Laser plasma protons with future application on cancer therapy and Proton Radiography

Rashida Jafer

Supervisor: Prof. Dimitri Batani

A thesis submitted for the Degree of Doctor of Philosophy to the "Dipartimento di fisica "G.Occhialini" Universita' degli studi di Milano Bicocca"

14 December 2009

ABSTRACT

Recent developments in high power, ultrashort pulse laser systems enable laser intensities beyond 10^{21} W/cm^2 to be achieved. When focused onto thin foil targets, plasmas with extremely high electrostatic fields ($>10^{12}$V/m) are produced, resulting in the acceleration of protons/ions to very high energies (~60MeV). During my PhD, I have worked on experimental investigations into proton acceleration driven by high power laser pulses. Key to successful deployment of laser proton sources one one side is getting higher proton energies through to achieve the ultimate goal of realising table top machines for the treatment of cancer and on the other side, optimising the beam quality, an objective that was of the main motivation for my PhD work. My two main achievements were:

1. The production of bright, ultrashort and radially smooth pulsed proton beams using laser heating of pre-plasmas formed with long (nanosecond) pulses with ultrahigh intensity picosecond pulses.

2. Use of these beams to study the ultrafast dynamics of target implosion under intense laser irradiation

The experiments on proton acceleration with the specific goal of controlling the proton beam quality by optical tool design, were performed at RAL. This scheme involves the use of multiple laser pulses to enhance and control the properties of beams of protons accelerated in ultra-intense laser irradiation of planar foil targets. Specifically, one laser pulse produces and controls the expansion of the target to enhance the energy coupling to the main (delayed) laser and/or drives shock deformation of the target to change the direction of the proton beam. The preplasma formed by this low intensity nanosecond beam (~ 0.5-5×10^{12} W/cm^2) was used to enhance the laser absorption of the main (delayed) CPA (Chirped pulse amplified). The main CPA picosecond beam was used at high intensity (~ 4×10^{20} W /cm^2) to produce intense proton beams from the hydrogen rich target. The optimum intensity of the nanosecond beam was investigated and optimised to yield a very smooth and circular distribution of the proton beam achieved using a second long pulse laser at 5×10^{12}w/cm^2.

The second achievement concerns an experiment also performed at RAL on proton radiography. As the laser based protons are characterised by small source size,

high degree of collimation and short duration, they can be used in point projection backlighting schemes to perform radiography. In particular, I used this idea to perform radiography of a cylindrical target ~ 200µm long imploding under irradiation by long laser pulses of nanosecond duration. This allows measuring the degree of compression of the target as well as the stagnation time in the dynamic regime. The experiment took place in the framework of the HiPER project (the European High Power laser Energy Research facility Project). The final goal of the experiment was to study the transport of fast electron in cylindrical compressed target a subject of interest for fast ignition. In parallel to proton radiography x-ray radiography was used to compare the results. One of the specific advantages of using laser generated protons is that their spectrum is continuous upto a high energy cutoff. Because of their different time of flights protons proved to be very effective in revealing the implosion history of the target. In principle, the obtained implosion can be followed in time with a single shot sensitivity. Instead x-ray radiograph gives one image per laser shot at one fixed time and one has to make several shots in order to reveal the complete history of implosion. Another advantage of using proton radiography is a simpler experimental setup keeping imploding cylinder between proton target and proton detector on the same axis. Simulations of formation of proton images were made with the Monte Carlo MCNPX Code using the density profiles of the imploded cylinder obtained with the 2D-hydro CHIC code. A detailed study of Multiple Coulomb Scattering and Stopping Powers of the protons in low energy regimes for cold and warm matter was done to interpret the experimental results.

Finally, I'm taking part in the analysis of experimental results obtained at the University of Rochester (USA) on the Omega-EP laser, and concerning magnetic field effect on the proton radiographs of a wired cone.

Acknowledgement:

Contents:

INTRODUCTION

Chapter 1

Theoratical Survey on Conventional and Laser Based Proton Sources:

Chapter 2:

Potential Applications of Laser Plasma Protons:

Chapter 3:

Laser Plasma Interactions and Particle Acceleration

Chapter 4:

Description of Used Laser Facilities for the Experimental Work

Chapter 5:

Uniform Distribution and enhancement of Laser Driven ion/proton beam Energies

INTRODUCTION

INTRODUCTION

Protons, discovered by Rutherford in 1918, are obviously of enormous importance for our understanding of matter. However, they have also been used for many applications. X rays (and g-rays) are commonly used for radiography and radiotherapy, but protons may have several important advantages. For instance, already today they are efficiently used in radiotherapy to cure cancer by damaging irreversibly the DNA of cells while allowing for a much-reduced collateral damage to surrounding healthy tissues. Protons beams have been considered as possible sources for radiography in the context of stewardship of the nuclear stockpiles. They may also be used in microelectronics (proton writing) and for the production of short-living radioisotopes, needed in PET imaging. More recently proton beams were used in plasma diagnostics. Being charged, they are sensitive to electric and magnetic fields in plasmas (or, in general, in matter) therefore allowing detecting them. With this respect the recent development of laser-driven proton sources allows the generation of very short pulse (ps) high-charge bunches of protons. First, this adds the time-resolution dimension to the potentiality of proton applications. Second, the rapidly decreasing costs of high-intensity laser systems (as driven by rapid developments in laser technology) can allow for production of energetic proton beams at a price considerably lower that what is possible today.

laser-driven proton sources

Ion (and proton) emission from laser-plasmas is a subject, which has been largely studied from the 70's (ions were mainly used for plasma diagnostic but later also for application as sources for injection to accelerators). The early works showed a correlation between ion mean energy and scaled laser intensity ($I\lambda^2$ using the laser wavelength). They also showed only weak dependence on target material and laser (wavelength, pulse length, focal conditions) [for instance, see the review in E.Clarket al, Phys Rev Lett, 85, 1654 (2000)]. At the end of the 90's, high-energy short-pulse laser systems based on the CPA (Chirped Pulse Amplification) technology were

introduced, capable of delivering intensities " 10^{18} W/cm^2, the so-called relativistic limit (at such intensity, electrons in the laser field oscillate at velocity comparable to light velocity). With CPA lasers new features are seen, in particular a first experiment at Livermore evidenced (with surprise) the generation of protons with:

 i) strong energy/angle correlation, ii) high collimation, iii) energy up to 58MeV [Snavely et al., Phys.Rev.Lett, Oct 2000].
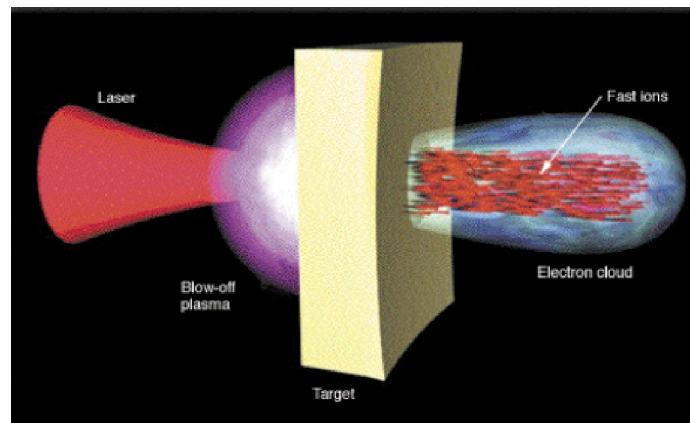
Fig 1. Schematic of the TSNA mechanism at work in laboratory experiments

In the following years, experimental and theoretical research allowed to ascribe the generation of protons to the so-called TSNA Mechanism (Target Sheath Normal Acceleration): protons are accelerated at target rear by a quasi electrostatic field produced when part of the fast electrons generated by the laser on the front side reach the target rear and escape in vacuum, producing a charge separation. The fact that protons are emitted with any kind of target (even not containing hydrogen) shows the crucial role of hydrocarbons / H2O contamination in these experiments (having lower mass, protons are accelerated before and take most of the energy as compared to heavier ions from target bulk) [V.Yu.Bychenkov, D.Batani, et al. "Ion acceleration from expanding multi-species plasma" phys.Plasmas, 11, 3242 (2004)]. Clearly in the TNSA mechanism, the characteristics of the proton source, acceleration and collimation critically depend on how many electrons arrive at target rear, their residual energy, and the flow geometry. Therefore the study of electron transport is essential for optimizing laser proton sources. The characteristics of the proton sources, some of which can easily be derived from above graphs, are:

1-High directionality along the normal to the back surface of targets and small angular divergence (below $10°$ for protons > 10 MeV)

2-Ultra shot time duration (~ 1 ps) and very compact dimensions (acceleration length less than a few %m, transversal dimension a few 10 %m)

3-Large intensity (up to 1012 protons/shot implying ~2 J or 0.2 %C per shot or a current of ~2 105 A)

4-Ultra low emittance: transversal emittance < 0.08 mm mrad, longitudinal emittance $< 10^{-4}$ eV s, better than conventional accelerator beams.

Again, the difference between target materials evidences different fast electron transport (probably due to «electric inhibition» of fast electron propagation in plastics, from self-generated resistive electric fields). It should be noticed that while the energy record of laser-generated protons is $ 70 MeV obtained with high-energy relatively long pulses (up to 0.5 ps), lower proton energies have been obtained with laser systems characterized by shorter pulses, like the one we have used at LOA. Filling such a gap, and further increasing the energy of laser-generated protons, is one of the current challenges in this field of research.

Applications

Several applications of protons from conventional sources are already very important today. In particular:

1) cancer therapy

Already today, protons from "conventional" sources are used for cancer therapy. The rationale of radiotherapy is that the deposited dose damages and kills cancer cells, but at the same time however, it must avoid, as far as possible, collateral damage to surrounding healthy tissues. This is indeed one of the main problems in radiotherapy and it is particularly difficult with photons. Indeed g-rays are intrinsically characterized by an exponential absorption in matter, implying that the dose deposited "before" the cancer region is indeed even larger than that delivered to the tumour

(while some dose is also released after it). On the contrary the absorption of protons in matter is characterized by a "Bragg peak" which means that the protons lose little energy while travelling in matter until they are close to the end of their path where they deposited most of the energy, as shown in Fig.2.
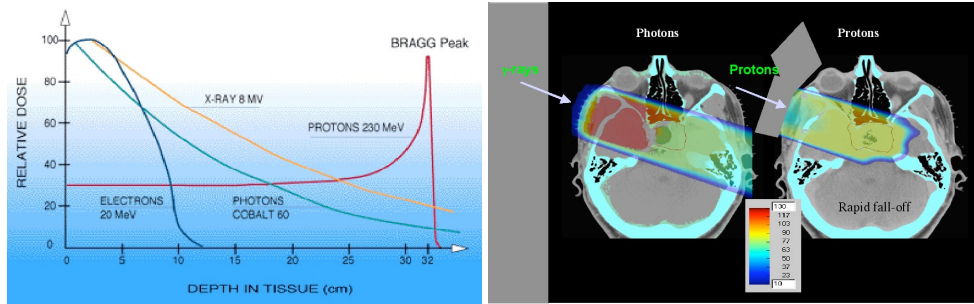
Fig. 2: comparison of energy deposition in biological matter for X-rays and protons in terms of depth (left) and of actual dose deposition in the head of a patient (right)

Not only energy deposition is longitudinally quite localized (due to the Bragg 's peak) but also proton beams are characterized by little angular diffusion providing high lateral precision on deposited dose. Therefore, the target can be irradiated in a geometrical "conformal" way by moving the proton beam (of course a capability of reducing the energy of protons is needed in order to adjust the penetration to the depth of the different cancer layers in the body).

Due to the advantages of proton therapy, if ion accelerators were small and cheap as electron linacs, then probably radiotherapy would be made with protons, more precise and with the same effects of grays. However today 99% of radiotherapy is done with g-rays and only a few centres in the world use «conventional» sources (Fig. 3 left) to perform proton-therapy, including 5 in USA, 4 in Japan, 2 in China, 1 in Switzerland, 1 in Germany, 1 in Korea, etc. For instance, in Italy a considerable effort is going on for the realization of CNAO (Centro Nazionale di Adroterapia Oncologica) located in Pavia (Northern Italy) with the participation of several cancer centres, the TERA Foundation, the INFN (Italian National Institute of Nuclear Physics), and an initial investment of the order of 70 M euros.
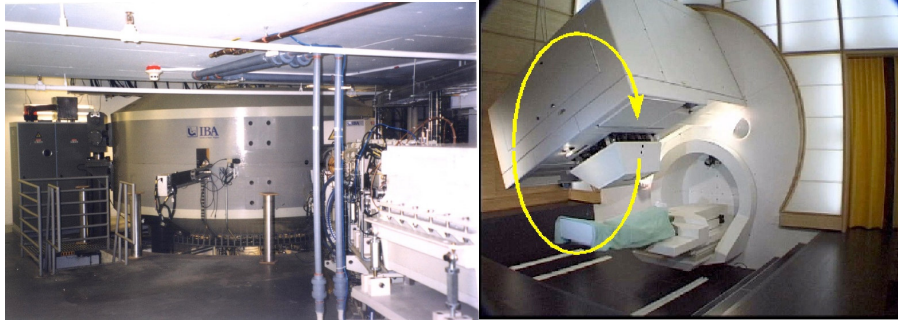
Fig. 3: Left) Cyclotron (IBA-NPTC): max proton energy: 250 MeV, pulse rate: CW, power: 400KW, size: 4 m diameter; Right) Positioning (gantry) weight: 220 tons

The main limitation towards a larger spreading of proton therapy comes from the huge costs, which do not make it possible to provide each hospital with an irradiation apparatus, as in the case of g-rays. Such costs are in part related to proton sources, but in reality mainly come from positioning (gantry, see Fig. 3 right) and the need for very large radio protected areas. Indeed all the area from the proton source to the irradiation point needs to be radio protected. There is a likely need for alternative sources of protons at lower price and, above all, reducing the positioning and radioprotection costs. Lasers are promising candidates: the advent of compact and powerful lasers, with moderate costs and high repetition, as driven by rapid developments in laser technology, makes it possible to think of new compact and low-cost "laser-proton sources". But above all, with lasers the radio protected area could be much smaller, and also steering of the laser beam is much easier and cheaper of proton beam steering. Therefore if protons with required characteristics can be produced by lasers in proximity of patients, costs of proton therapy would be substantially cut, allowing its large spreading.

2) plasma diagnostics and proton radiography

For some time, physicists have considered using protons as a way to penetrate thick materials more effectively than X-rays. Proton radiography was also used for early medical imaging tests, but these were not promising: radiographs were blurred due to scattering of protons as they move through objects. In 1995 researchers at Los Alamos had the idea of using a magnetic lens to focus scattered protons into a clear image. This can be possibly used for stockpile stewardship to image in depth inside dynamic systems. Preliminary tests have been made at Los Alamos and Brookhaven.

Fig. 4: Left) a 3-ton steel vessel used to confine the explosion involved in proton-radiography experiments is flanked by large orange electromagnets focusing the protons to produce sharp radiographs at Los Alamos. Right) proton radiography with ~8 MeV laser-generated protons by M. Roth et al. at LULI showing the ability to discriminate different thicknesses and densities

More recently efforts in the field of proton radiography have been undertaken using laser-generated protons [M.Roth, et al., Phys. Rev. ST Accel. Beams 5, 061002 (2002)]. The ultra-low emittance of laser-accelerated protons allowed radiography of dense objects with excellent spatial resolution (a resolution in the object plane of < 2.5 %m has been demonstrated in following experiments).

Laser-generated protons have been used to obtain dynamical images of compression induced by a laser-generated shock in [M. Koenig, D. Batani, et al. "Progress in the study of Warm Dense Matter" Plasma Phys. Contr. Fusion, 47, B441 (2005)]. In which full advantage of the time domain dimension of laser-generated protons has been taken. Since the proton emission is practically instantaneous (of the order of 1 ps) with respect to the phenomena to be probed, and since protons with such energies are non-relativistic (and therefore travel at different velocities) they probe the system at different times.

Moreover such protons are also characterized by different penetration in materials (different depth of the Bragg peak). Therefore a stack of radiochromic films placed at a given distance from the system, allows obtaining 2D images at different times: proton of a given energy have probed the system at a given time but they also preferentially deposit their energy at a give layer, e.g in a given RCF. More recently I have used this technique to diagnose the implosion of cylindrical targets (in connection to the experiment at RAL on fast electron transport in cylindrically

compressed targets). The detailed study of proton radiography and experimental results are discussed in chapter 6.

A variation of proton radiography (or better proton probing) is based on the fact that protons are charged and hence sensitive to electric and magnetic fields thereby allowing them to be detected, with simultaneous time and space resolution. The technique was originally introduced by Borghesi et al. at Queens, Belfast. Our group has used it to detect the presence of huge quasi-electrostatic fields ($1011 V/m) associated to the propagation edge of fast electrons in a gas medium (ionization front) [S.Baton, D.Batani, et al. "Recent experiments on electron transport in high-intensity laser matter interaction" Plasma Phys. Contr. Fusion, 47 B777 (2005); D.Batani, et al. "Laser-driven fast electron dynamics in gaseous media under the influence of large electric fields" Phys. Plasmas (2009)]. The protondetection
of electric and magnetic fields in the plasmas, with simultaneous time and space resolution, opens new possibilities for the progress of studies on controlled thermonuclear fusion.

So, In my opinion, today's challenges in the laser-driven proton sources can be summarized as follows:

• being able to increase the energy of proton beams up to 300 MeV (for applications in cancer treatment or for radiography of dense / thick samples)
• being able to achieve such energy by using relatively compact and high-repetition laser systems (therefore system which are characterized by relatively low energy and very short pulses)
• being able to obtain quasi-monoenergetic spectra (for applications in proton radiography or, again, cancer therapy) or, more in general, to control and shape the proton spectra
• being able to obtain much larger proton currents and show the focusability of such beams (for applications in fast ignition)

Structure of the thesis

I basically took part in several experimental campaigns at Rutherford Appleton Laboratory, Didcot UK , LOA, Paris France, Lund Laser Centre, Lund Sweden and ILE, Osaka Japan. This thesis is related to the two main sets of experiments conducted at RAL, UK on optical control of proton beam spectra and proton radiography.

Chapter 1 is dedicated for a detailed theoretical survey of proton sources. It has been demonstrated by literature survey that how laser-based protons could be advantageous over the conventional proton sources.

Chapter 2 is dedicated to the potential applications of the laser-based proton sources including proton radiotherapy and radiography.

Chapter 3 comprises the physics of laser plasma interactions.

Chapter 4 shows the configuration and details of the laser facilities, where I have been conducted experiments during my PhD research.

Chapter 5 is dedicated to the first experimental part in which the study of optical control of proton beam spectra and effects of plasma prepulse on the proton beam shaping has been described. Results and experimental methods are discussed in details.

Chapter 6 is dedicated to the second experimetntal part in which I have described a detailed study of proton radiography. The experimental methods, results and analytical techniques are discussed intensively. Finally I have shown the novelty of my work in controlling the spectral shape of proton beam and the new step in proton radiography by comparing the experimental results with MCNPX simulation code.

CHAPTER 1

Theoretical Survey on Conventional and Laser Based Proton Sources

1.1 Protons

The proton was discovered by Ernest Rutherford in 1918. He fired alpha particles, which are essentially helium nuclei without electrons, into a nitrogen gas. His detectors found the characteristic signature of hydrogen nuclei being produced. He realized that these hydrogen nuclei could have only come from the nitrogen gas. This led to the theory that the nucleus of a hydrogen atom was an elementary particle, the proton, and that protons could be found in the nuclei of all atoms.

The properties of atoms are defined by the number of electrons, neutrons and protons they have. But the number of protons is the most significant variable. So significant, in fact, that the number of protons in the nucleus of an atom is referred to as the atomic number, and atoms are named based on the number of protons they have. The atomic number is the most physically relevant characteristic of an atom.

Atoms with low atomic numbers are the most prevalent in the universe, because they are the easiest to form. This is why hydrogen and helium are the most abundant elements in the universe.

Protons are accelerated to significant fractions of the speed of light in particle physics experiments. Ballistic protons are responsible for a lot of discoveries in the huge "Particle Zoo" that 20th century physics generated. Unlike neutrons, protons are stable outside of an atomic nucleus, making them useful for purposes of experimentation.

The elementary charge, usually denoted by e, is the electric charge carried by a single proton, or equivalently, the negative of the electric charge carried by a single electron. This is a fundamental physical constant. It has a measured value of approximately $1.602176487(40) \times 10^{-19}$ coulombs.[2]   In   cgs,   the   value   is $4.80320427(12) \times 10^{-10}$ statcoulombs [3]. In the system of atomic units as well as some other systems of natural units, e functions as the unit of electric charge, i.e. $e = 1$ in those unit systems.

Since the atomic number of hydrogen is 1, a positive hydrogen ion (H+) has no electrons and corresponds to a bare nucleus with 1 proton (and 0 neutrons for the most abundant isotope 1H). In chemistry and biology therefore, the word "proton" is commonly used as a synonym for hydrogen ion (H+) or hydrogen nucleus in several contexts:

1. The transfer of H+ in an acid-base reaction is referred to "proton transfer". The acid is referred to as a proton donor and the base as a proton acceptor.
2. The hydronium ion (H3O+) in aqueous solution corresponds to a hydrated hydrogen ion. Often the water molecule is ignored and the ion written as simply H+(aq) or just H+, and referred to as a "proton". This is the usual meaning in biochemistry, as in the term proton pump which refers to a protein or enzyme which controls the movement of H+ ions across cell membranes.
3. Proton NMR refers to the observation of hydrogen nuclei in (mostly organic) molecules by nuclear magnetic resonance. This method uses the spin of the proton, which has the value of one-half.

Prior to Rutherford, Eugen Goldstein had observed canal rays, which were composed of positively charged ions. After the discovery of the electron by J.J. Thomson, Goldstein suggested that since the atom is electrically neutral there must be a positively charged particle in the atom and tried to discover it. He used the "canal rays" observed to be moving against the electron flow in cathode ray tubes. After the electron had been removed from particles inside the cathode ray tube they became positively charged and moved towards the cathode. Most of the charged particles passed through the cathode, it being perforated, and produced a glow on the glass. At this point, Goldstein believed that he had discovered the proton.[7] When he calculated the ratio of charge to mass of this new particle (which in case of the electron was found to be the same for every gas that was used in the cathode ray tube) was found to be different when the gases used were changed. The reason was simple. What Goldstein assumed to be a proton was actually an ion. His work was widely ignored.

1.2 Stopping Power of Particles into matter.

In passing through matter, fast charged particles ionize the atoms or molecules which they encounter. Thus, the fast particles gradually lose energy in many small steps. By stopping power we mean the average energy loss of the particle per unit path length, measured for example in MeV/cm (see figure to the right). Stopping power is a necessary ingredient for many parts of basic science, for medical and for technological applications
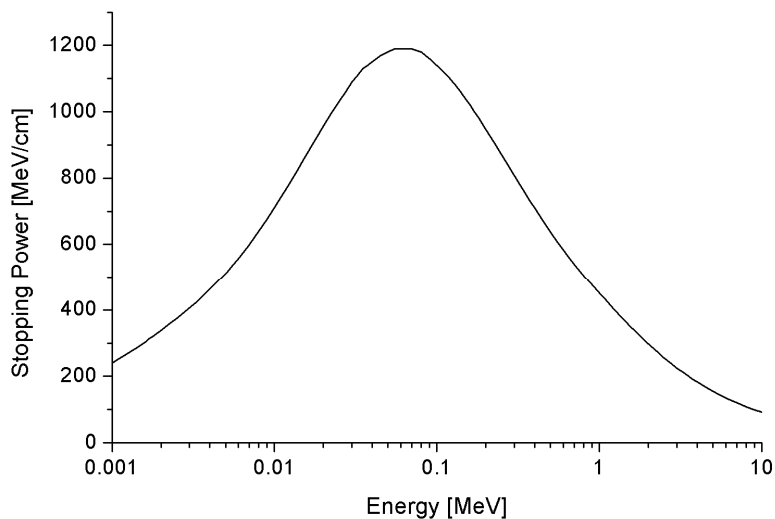
The stopping power of aluminium for protons, plotted versus proton energy.

Stopping power and range

The stopping power depends on the type and energy of the particle and on the properties of the material it passes. Since the production of an ion pair (usually a positive ion and a negative electron requires a fixed amount of energy (for example, 34 eV in air), the density of ionisation along the path is proportional to the stopping power of the material.

Both electrons and positive ions lose energy while passing through matter. In the following, we mainly treat positive ions.

The 'stopping power', S(E) is a property of the material, which expresses the energy loss per unit path length according to:

$$S(E) = -\frac{dE}{dx}$$

where E is the energy, and x is the path length. The minus sign makes S positive.
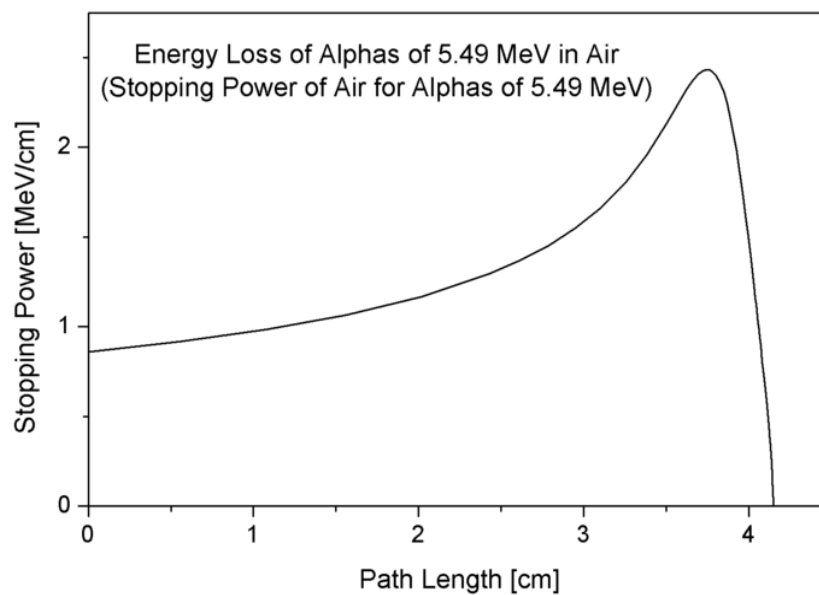
Fig 1.1: Bragg curve of 5.49 MeV alphas in air

The stopping power and hence, the density of ionization, usually increases toward the end of range and reaches a maximum, the Bragg peak, shortly before the energy drops to zero. The curve that describes this is called the Bragg curve. This is of great practical importance for radiation therapy.

The equation above defines the linear stopping power which may be expressed in units like MeV/mm or similar. Very often one divides *S(E)* by the density of the material to obtain the mass stopping power which may be expressed in units of

MeV/(mg/cm^2) or similar. The mass stopping power is nearly independent of the density of the material.

The picture in figure 1.1 shows how the stopping power of 5.49 MeV alpha particles increases while the particle traverses air, until it reaches the maximum. This particular energy corresponds to that of the naturally radioactive gas radon (222Rn) which is present in the air in minute amounts wherever the ground contains granite.

The mean range can be calculated by integrating the reciprocal stopping power over energy. The deposited energy can be obtained by integrating the stopping power over the entire path length of the ion when it moves in the solid.

1.2.1 Electronic, nuclear and radiative stopping

By electronic stopping, one means slowing down due to the inelastic collisions between bound electrons in the medium and the ion moving through it.

Since the number of collisions an ion experiences with electrons is large, and since the charge state of the ion while traversing the medium may change frequently, it is very difficult to describe all possible interactions for all possible ion charge states. Instead, the electronic stopping power is often given as a simple function of energy $S_e(E)$ which is an average taken over all energy loss processes for different charge states. It can be theoretically determined to an accuracy of a few % in the energy range above several hundred keV per nucleon from theoretical treatments, the best known being the Bethe formula. At energies lower than about 100 keV per nucleon, it becomes more difficult to determine the electronic stopping theoretically (see Sigmund 2005).

Graphical presentations of experimental values of the electronic stopping power for many ions in many substances have been given by Paul, see http://www.exphys.uni-linz.ac.at/Stopping/. The accuracy of various stopping tables has been determined, e.g., by (Paul 2006), using statistical comparisons.
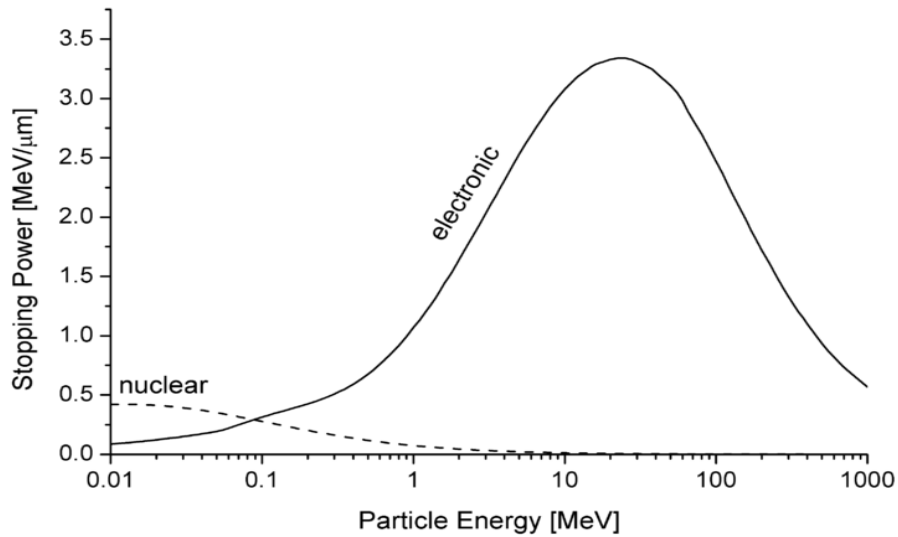
Figure 1.2: Electronic and nuclear stopping power for aluminium ions in aluminium, versus particle energy. The maximum of the nuclear stopping curve typically occurs at energies of the order of 1 keV per nucleon, of the electronic stopping power below 100 keV per nucleon.

By nuclear stopping, one means elastic collisions between the ion and atoms in the sample (the established designation "nuclear" is a misnomer since nuclear stopping is not due to nuclear forces [1]. If one knows the form of the repulsive potential $V(r)$ between two atoms (see below), it is possible to calculate the nuclear stopping power $S_n(E)$. In the stopping power figure 1.2 shows the protons in aluminum, we see that nuclear stopping is negligible except at the lowest energy. Nuclear stopping increases when the mass of the ion increases. In the figure shown here, nuclear stopping is larger than electronis stopping at low energy. For very light ions slowing down in heavy materials, the nuclear stopping is weaker than the electronic at all energies.

At not too high energies, the stopping power is therefore the sum of two terms: $S(E) = S_e(E) + S_n(E)$. Several semi-empirical stopping power formulas have been devised. The model given by Ziegler, Biersack and Littmark (the so called "ZBL" stopping) (Ziegler 1985), implemented in different versions of the TRIM/SRIM codes (http://www.SRIM.org), is used most often today.

At even higher energies, one has to consider, in addition, radiative stopping power which is due to the emission of bremsstrahlung in the electric fields of the nuclei of the material traversed[1].

Close to the surface, both nuclear and electronic stopping may lead to sputtering.

1.2.2 Energy regimes

At very high energies (larger than several hundreds of MeV per nucleon), nuclear reactions and (especially for electrons) bremsstrahlung and Cherenkov radiation contribute to the slowing down of all charged particles (Burcham 1979). The remainder of (Burcham 1979) mainly deals with lower energies.

The slowing-down process in Solids
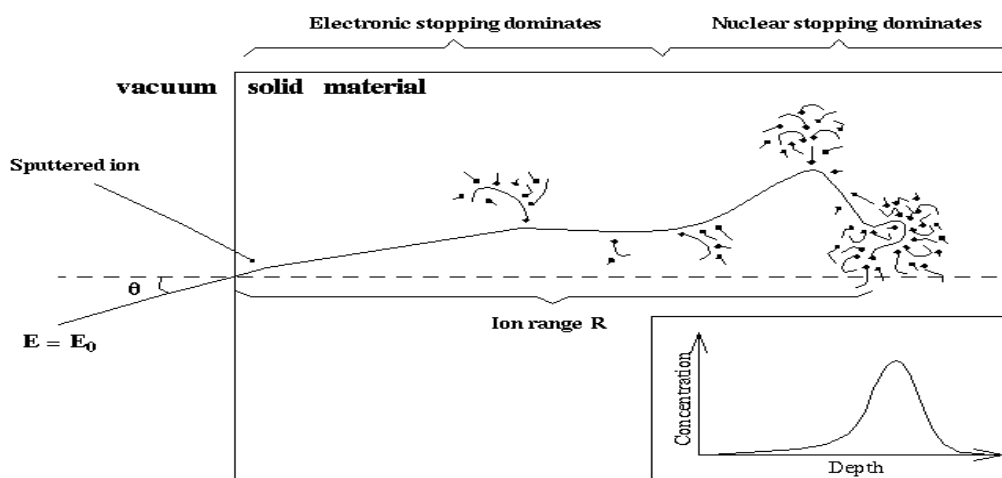
Figure 1.3 : llustration of the slowing down of a single ion in a solid material.

In the beginning of the slowing-down process at high energies, the ion is slowed down mainly by electronic stopping, and it moves almost in a straight path. When the ion has slowed down sufficiently, the collisions with nuclei (the nuclear stopping) become more and more probable, finally dominating the slowing down. When atoms of the solid receive significant recoil energies when struck by the ion, they will be removed from their lattice positions, and produce a cascade of further collisions in the

material. These collision cascades are the main cause of damage production during ion implantation in metals and semiconductors.

When the energies of all atoms in the system have fallen below the threshold displacement energy, the production of new damage ceases, and the concept of nuclear stopping is no longer meaningful. The total amount of energy deposited by the nuclear collisions to atoms in the materials is called the nuclear deposited energy.

The inset in the figure 1.3 shows a typical range distribution of ions deposited in the solid. The case shown here might for instance be the slowing down of a 1 MeV silicon ion in silicon. The mean range for a 1 MeV ion is typically in the micrometer range.

1.2.3 Repulsive interatomic potentials

At very small distances between the nuclei the repulsive interaction can be regarded as essentially Coulombic. At greater distances, the electron clouds screen the nuclei from each other. Thus the repulsive potential can be described by multiplying the Coulombic repulsion between nuclei with a screening function $\varphi(r/a)$,

$$V(r) = \frac{1}{4\pi\varepsilon_0}\frac{Z_1 Z_2 e^2}{r}\varphi(r/a)$$

where $\varphi(r) \rightarrow 1$ when $r \rightarrow 0$. Here Z_1 and Z_2 are the charges of the interacting nuclei, and r the distance between them. a is the so called screening parameter.

A large number of different repulsive potentials and screening functions have been proposed over the years, some determined semi-empirically, others from theoretical calculations. A much used repulsive potential is the one given by Ziegler, Biersack and Littmark, the so called (ZBL repulsive potential). It has been constructed by fitting a universal screening function to theoretically obtained potentials calculated for a large variety of atom pairs (Ziegler 1985). The ZBL screening parameter and function have the forms

$$a = a_u = \frac{0.8854a_0}{Z_1^{0.23} + Z_2^{0.23}}$$

and

$$\varphi(x) = 0.1818e^{-3.2x} + 0.5099e^{-0.9423x} + 0.2802e^{-0.4029x} + 0.02817e^{-0.2016x}$$

where x = r / au and a0 is the Bohr atomic radius = 0.529 Å.

The standard deviation of the fit of the universal ZBL repulsive potential to the theoretically calculated pair-specific potentials is 18 % above 2 eV (Ziegler 1985). Even more accurate repulsive potentials can be obtained from self-consistent total energy calculations using density-functional theory and the local-density approximation (LDA) for electronic exchange and correlation (Nordlund 1996).

1.2.4 Channeling

In crystalline materials the ion may in some instances get "channeled", i.e., get focused into a channel between crystal planes where it experiences almost no collisions with nuclei. Also, the electronic stopping power may be weaker in the channel. Thus the nuclear and electronic stopping do not only depend on material type and density but also on its microscopic structure and cross-section.

1.2.5 Computer simulations of ion slowing down

Computer simulation methods to calculate the motion of ions in a medium have been developed since the 1960s, and are now the dominant way of treating stopping power theoretically. The basic idea in them is to follow the movement of the ion in the medium by simulating the collisions with nuclei in the medium. The electronic stopping power is usually taken into account as a frictional force slowing down the ion.

Conventional methods used to calculate ion ranges are based on the binary collision approximation (BCA) (Robinson 1974). In these methods the movement of ions in the implanted sample is treated as a succession of individual collisions between the recoil

ion and atoms in the sample. For each individual collision the classical scattering integral is solved by numerical integration.

The impact parameter p in the scattering integral is determined either from a stochastic distribution or in a way that takes into account the crystal structure of the sample. The former method is suitable only in simulations of implantation into amorphous materials, as it does not account for channeling.

The best known BCA simulation program is [TRIM/SRIM](#) (short of TRansport of Ions in Matter, in more recent versions called Stopping and Range of Ions in Matter), which is based on the ZBL electronic stopping and interatomic potential (Biersack 1980, Ziegler 1985, www.SRIM.org). It has a very easy-to-use user interface, and has default parameters for all ions in all materials up to an ion energy of 1 GeV. However, it doesn't take account of the crystal structure, which severely limits its usefulness in many cases.

Although the BCA methods have been successfully used in describing many physical processes, they have some obstacles for describing the slowing down process of energetic ions realistically. Due to the basic assumption that collisions are binary, severe problems arise when trying to take multiple interactions into account. Also, in simulating crystalline materials the selection process of the next colliding lattice atom and the impact parameter p always involve several parameters which may not have perfectly well-defined values, which may affect the results 10-20 % even for quite reasonable-seeming choices of the parameter values.

A fundamentally more straightforward way to model multiple atomic collisions is provided by molecular dynamics (MD) simulations, in which the time evolution of a system of atoms is calculated by solving the equations of motion numerically. Special MD methods have been devised in which the number of interactions and atoms involved in MD simulations have been reduced in order to make them efficient enough for calculating ion ranges (Nordlund 1995, Beardmore 1998)

1.2.6 Minimum ionizing particle

When a fast charged particle passes through matter, it ionizes or excites the atoms or molecules that it encounters, losing energy in small steps. The mean rate at which it loses energy depends on the material, the kind of particle and also its momentum. In practical cases, most relativistic particles (e.g., cosmic-ray muons) are minimum ionizing particles.

1.2.7 Radiation Length:

High-energy electrons predominantly lose energy in matter by bremsstrahlung. The characteristic amount of matter traversed for these related interactions is called the radiation length X0, usually measured in gcm^{-2}. It is both the mean distance over which a high-energy electron loses all but 1/e of its energy by bremsstrahlung. It is also the appropriate scale length for describing high-energy electromagnetic cascades.

The radiation length is given, to good approximation, by the expression

$$X_0 = \frac{716.4 \cdot A}{Z(Z+1)\ln \frac{287}{\sqrt{Z}}} \; g \cdot cm^{-2}$$

where Z is the atomic number and A is the mass number.

While this definition may also be used for other electromagnetic interacting particles beyond leptons and photons, the presence of the stronger hadronic and nuclear interaction makes it a far less interesting characterisation of the material; the nuclear collision length and nuclear interaction length are more relevant.

Comprehensive tables for radiation lengths and other properties of materials are available from http://pdg.lbl.gov/AtomicNuclearProperties

1.2.8 Range

In passing through matter, charged particles ionize and thus lose energy in many steps, until their energy is (almost) zero. The distance to this point is called the range of the particle. The range depends on the type of particle, on its initial energy and on the material which it passes.

For example, if the ionising particle passing through the material is a positive ion like alpha particle or proton, it will collide with atomic electrons in the material via Coulomb interaction. Since the mass of the proton or alpha particle is much larger than that of the electron, there will be no significant deviation from the radiation's incident path and very little kinetic energy will be lost in each collision. As such, it will take many successive collisions for such heavy ionising radiation to come to a halt within the stopping medium or material. Maximum energy loss will take place in a head on collision with an electron.

Since large angle scattering is rare for positive ions, a range may be well defined for that radiation, depending on its energy and charge, as well as the ionisation energy of the stopping medium. Since the nature of such interactions is statistical, the number of collisions required to bring a radiation particle to rest within the medium will vary slightly with each particle, i.e. some may travel further and undergo less collisions than others. Hence, there will be a small variation in the range, known as straggling.

The energy loss per unit distance (and hence, the density of ionization), or stopping power also depends on the type and energy of the particle and on the material. Usually, the energy loss per unit distance increases while the particle slows down. The curve describing this fact is called the Bragg curve. Shortly before the end, the energy loss passes through a maximum, the Bragg Peak, and then drops to zero (see the figures in Bragg Peak and in stopping power).

The range of alpha particles in ambient air amounts to several centimetres, while this type of radiation can be stopped already by a sheet of paper. Although beta particles scatter much more than alpha particles, a range can still be defined; it, frequently amounts to several hundred centimeters of air.

The mean range can be calculated by integrating the inverse stopping power over energy.

1.3 The Bragg Peak

The ionization density (number of ions per unit of path length) produced by a fast charged particle along its track increases as the particle slows down. It eventually reaches a maximum called the Bragg peak close to the end of its trajectory. After that, the ionization density dwindles quickly to insignificance.
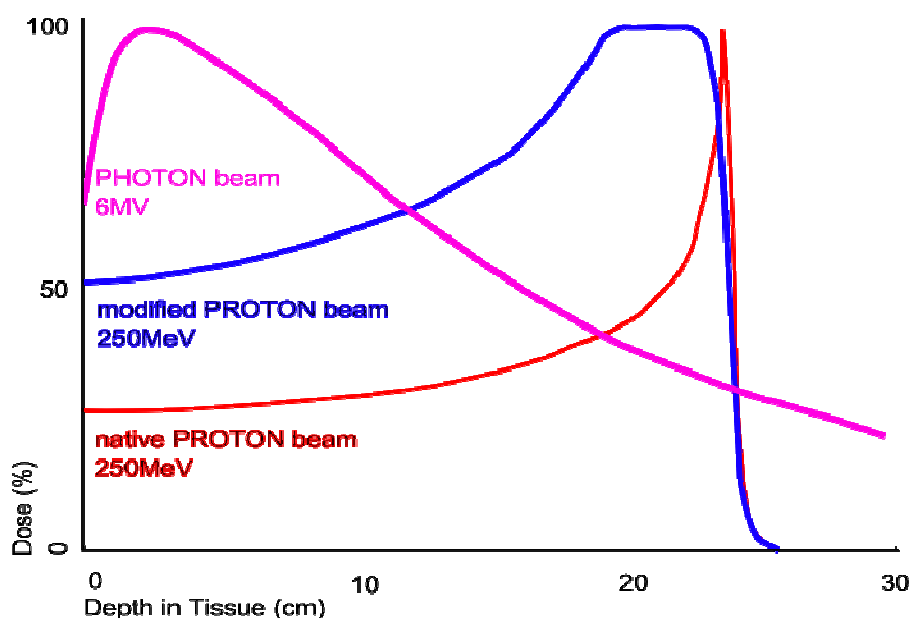
Figure 1.4: The dose produced by a native and by a modified proton beam in passing through tissue, compared to the absorption of a photon beam

When a fast charged particle moves through matter, it ionizes atoms of the material and deposits a dose along its path. A peak occurs because the interaction cross section increases as the charged particle's energy decreases. Figure 1.1 shows the peak for alpha particles of 5.49 MeV moving through air. Figure 1.4 shows the narrow peak of the "native" proton beam curve which is produced by a particle accelerator of 250

MeV. The figure also shows the absorption of a beam of energetic photons (X rays) which is entirely different in nature; the curve is mainly exponential.

The phenomenon is exploited in particle therapy of cancer, to concentrate the effect of light ion beams on the tumor being treated while minimizing the effect on the surrounding healthy tissue. The blue curve in the figure ("modified proton beam") shows how the originally monoenergetic proton beam with the sharp peak is widened by increasing the range of energies, so that a larger tumor volume can be treated. This can be achieved by using variable thickness attenuators.

1.4 Why Proton Therapy

Proton beam therapy has demonstrated success for the treatment of selected tumours. More than 20,000 patients have been treated with protons or light ions in research laboratories or hospitals around the world. The therapeutic radiation dose is limited by the unavoidable dose to healthy tissue surrounding the target. The mandate of modern radiation therapy has been to increase the dose to the target while reducing the dose to the surrounding tissue. To date more than 50% of proton beam treatments have been used for malignant melanoma of the eye. The precise dose localization with protons allows a uniform dose to be delivered to the tumour while sparing the nearby structures such as the lens and optic nerve. The alternative therapies are removal of the eye (enucleation) or radioactive plaque therapy. Proton therapy addresses this mandate because the physics of proton therapy is fundamentally different from the physics of traditional radiation

1.4.1 Proton VS X-Rays

Figure 1.5

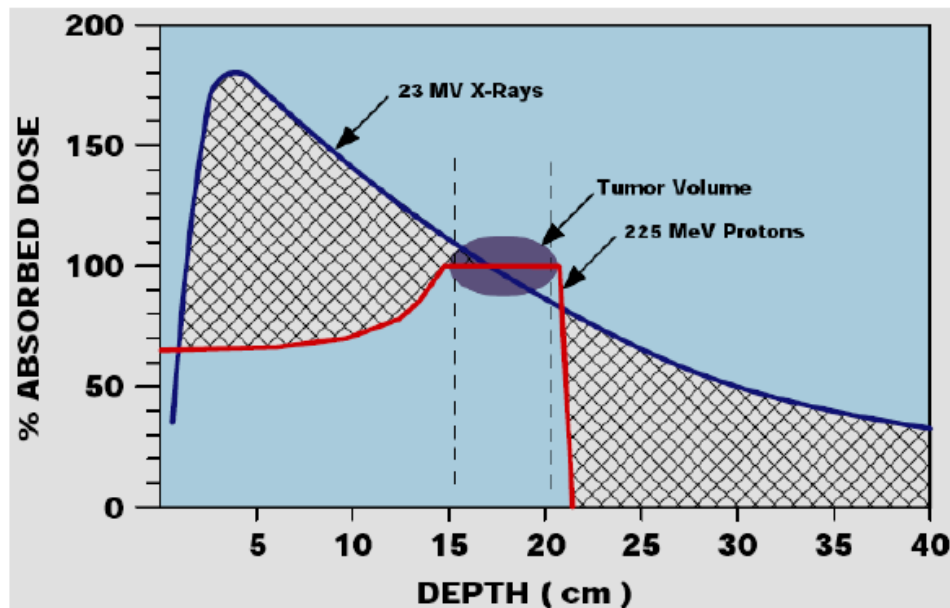As illustrated in the figure 1.5, traditional radiation deposits most of the dose near the skin (0 depth), and about 20% of the maximum dose to tissues beyond the target. Proton radiation delivers maximum dose at the target depth and falls off rapidly protecting tissue beyond the target. The maximum dose range (Bragg peak) can be extended - the spread out Bragg peak (SOBP) - to cover the tumor.
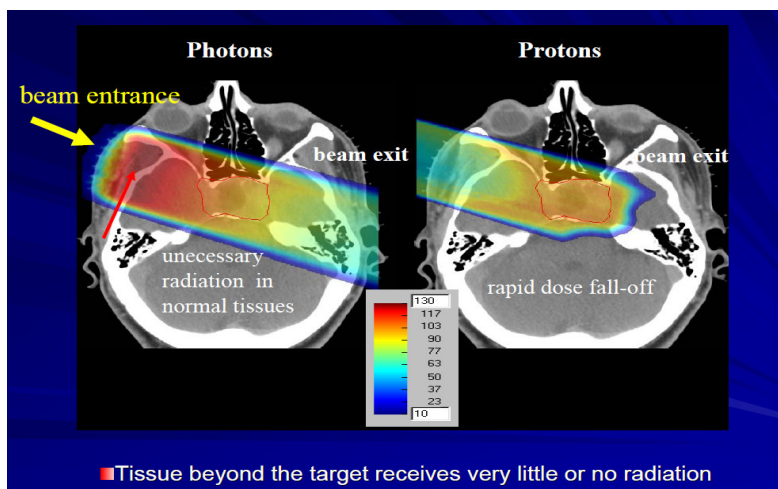

Figure 1.6

As shown in the figure 1.6, most of the treatments have been done with X-rays (photons). X-rays are successful in destroying tumours but they also damage the healthy tissue around the tumour. This is because the penetrating power of X-rays decreases exponentially with increasing depth as expressed by Beer's law:

$$I_{(x)} = I_o e^{-\mu x}$$

This means the X-rays deposit most of their energy near the surface of the body. If the tumour is deep-seated, this presents a problem.

Protons, being particles instead of rays, slow down much faster than X-rays. Their power, however, does not decrease exponentially (as it does for X-rays). Instead, they deposit more energy as they slow down, culminating in Bragg peak, the depth at which the peak occurs can be controlled by the amount of energy the protons are given by the accelerator.

Protons deposit their energy near the end of their path and have little lateral scatter. Therefore the beam energy can be precisely delivered to the tumour volume without seriously harming surrounding tissues or adjacent critical organs.

1.4.2 How Does Proton Therapy work for Cancerous Cells

There is a significant difference between standard (x-ray) radiation treatment and proton therapy. If given in sufficient doses, x-ray radiation techniques will control many cancers. But, because of the physician's inability to adequately conform the irradiation pattern to the cancer, healthy tissues may receive a similar dose and can be damaged. Consequently, a less- than-desired dose is frequently used to reduce damage to healthy tissues and avoid unwanted side effects. The power of protons is that higher doses of radiation can be used to control and manage cancer while significantly reducing damage to healthy tissue and vital organs.

Understanding how protons work provides patients and physicians with an insight into this mainstream treatment modality. Essentially, protons are a superior form of radiation therapy. Fundamentally, all tissues are made up of molecules with atoms as

their building blocks. In the centre of every atom is the nucleus. Orbiting the nucleus of the atom are negatively charged electrons.

When energized charged particles, such as protons or other forms of radiation, pass near orbiting electrons, the positive charge of the protons attracts the negatively charged electrons, ionizing the atom. Because of ionization, the radiation damages molecules within the cells, especially the DNA or genetic material. Damaging the DNA destroys specific cell functions, particularly the ability to divide or proliferate. Enzymes develop with the cells and attempt to rebuild the injured areas of the DNA; however, if damage from the radiation is too extensive, the enzymes fail to adequately repair the injury. While both normal and cancerous cells go through this repair process, a cancer cell's ability to repair molecular injury is frequently inferior. As a result, cancer cells sustain more permanent damage and subsequent cell death than occurs in the normal cell population. This permits selective destruction of bad cells growing among good cells.

Both standard x-ray therapy and proton beams work on the principle of selective cell destruction. The major advantage of proton treatment over conventional radiation, however, is that the energy distribution of protons can be directed and deposited in tissue volumes designated by the physicians-in a three-dimensional pattern from each beam used. This capability provides greater control and precision and, therefore, superior management of treatment. Radiation therapy requires that conventional x-rays be delivered into the body in total doses sufficient to assure that enough ionization events occur to damage all the cancer cells. The conventional x-rays lack of charge and mass, however, results in most of their energy from a single conventional x-ray beam being deposited in normal tissues near the body's surface, as well as undesirable energy deposition beyond the cancer site. This undesirable pattern of energy placement can result in unnecessary damage to healthy tissues, often preventing physicians from using sufficient radiation to control the cancer.

Protons, on the other hand, are energized to specific velocities. These energies determine how deeply in the body protons will deposit their maximum energy. As the protons move through the body, they slow down, causing increased interaction with orbiting electrons.

Maximum interaction with electrons occurs as the protons approach their targeted stopping point. Thus, maximum energy is released within the designated cancer volume. The surrounding healthy cells receive significantly less injury than the cells in the designated volume.

As a result of protons' dose-distribution characteristics, the radiation oncologist can increase the dose to the tumour while reducing the dose to surrounding normal tissues. This allows the dose to be increased beyond that which less-conformal radiation will allow. The overall affects lead to the potential for fewer harmful side effects, more direct impact on the tumour, and increased tumour control."

The minimized normal-tissue injury results in the potential for fewer effects following treatment, such as nausea, vomiting, or diarrhoea. The patients experience a better quality of life during and after proton treatment.

Proton Therapy VS X-Ray Therapy: in short

Protons	X-Rays
Low entrance Dose	High Entrance Dose
Almost no distal dose	Distal dose an issue
No exit dose	Finite exit dose
Less integral dose	Integral dose an issue
Bragg peak (fixed range)	Exponential dose fall-off

1.5 Conventional Proton Sources

Protons are accelerated conventionally using a devices that use electric fields of two basic types: linear accelerators and circular accelerators.

1.5.1 Linear particle accelerators

In a linear accelerator (linac), particles are accelerated in a straight line with a target of interest at one end. Linacs are very widely used – every cathode ray tube contains

one. They are also used to provide an initial low-energy kick to particles before they are injected into circular accelerators. The longest linac in the world is the Stanford Linear Accelerator, SLAC, which is 3 km (2 miles) long. SLAC is an electron-positron collider.

Linear high-energy accelerators use a linear array of plates (or drift tubes) to which an alternating high-energy field is applied. As the particles approach a plate they are accelerated towards it by an opposite polarity charge applied to the plate. As they pass through a hole in the plate, the polarity is switched so that the plate now repels them and they are now accelerated by it towards the next plate. Normally a stream of "bunches" of particles are accelerated, so a carefully controlled AC voltage is applied to each plate to continuously repeat this process for each bunch.

As the particles approach the speed of light the switching rate of the electric fields becomes so high that they operate at microwave frequencies, and so RF cavity resonators are used in higher energy machines instead of simple plates.

Linear accelerators are also widely used in medicine, for radiotherapy and radiosurgery. Medical grade LINACs accelerate electrons using a klystron and a complex bending magnet arrangement which produces a beam of 6-30 MeV. The electrons can be used directly or they can be collided with a target to produce a beam of X-rays. The reliability, flexibility and accuracy of the radiation beam produced has largely supplanted the older use of Cobalt-60 therapy as a treatment tool.

Figure 1.7 : Weizmann Institute particle accelerator

1.5.2 Tandem electrostatic accelerators

In a tandem accelerator, the negatively charged ion gains energy by attraction to the very high positive voltage at the geometric centre of the pressure vessel. When it arrives at the centre region known as the high voltage terminal, some electrons are stripped from the ion. The ion then becomes positive and accelerated away by the high positive voltage. Thus, this type of accelerator is called a 'tandem' accelerator. The accelerator has two stages of acceleration, first pulling and then pushing the charged particles. An example of a tandem accelerator is ANTARES (Australian National Tandem Accelerator for Applied Research).

1.5.3 Circular or cyclic accelerators

In the circular accelerator, particles move in a circle until they reach sufficient energy. The particle track is typically bent into a circle using electromagnets. The advantage of circular accelerators over linear accelerators (linacs) is that the ring topology

allows continuous acceleration, as the particle can transit indefinitely. Another advantage is that a circular accelerator is smaller than a linear accelerator of comparable final energy (i.e. a linac would have to be extremely long to provide the equivalent final energy of a circular accelerator).

Depending on the energy and the particle being accelerated, circular accelerators suffer a disadvantage in that the particles emit synchrotron radiation. When any charged particle is accelerated, it emits electromagnetic radiation and secondary emissions. As a particle traveling in a circle is always accelerating towards the center of the circle, it continuously radiates towards the tangent of the circle. This radiation is called synchrotron light and depends highly on the mass of the accelerating particle. For this reason, many high energy electron accelerators are linacs. Certain accelerators (synchrotrons) are however built specially for producing synchrotron light (X-rays).

1.5.4 Cyclotrons

The earliest circular accelerators were cyclotrons, invented in 1929 by Ernest O. Lawrence at the University of California, Berkeley. Cyclotrons have a single pair of hollow 'D'-shaped plates to accelerate the particles and a single large dipole magnet to bend their path into a circular orbit. It is a characteristic property of charged particles in a uniform and constant magnetic field B that they orbit with a constant period, at a frequency called the cyclotron frequency, so long as their speed is small compared to the speed of light c. This means that the accelerating D's of a cyclotron can be driven at a constant frequency by a radio frequency (RF) accelerating power source, as the beam spirals outwards continuously. The particles are injected in the centre of the magnet and are extracted at the outer edge at their maximum energy.
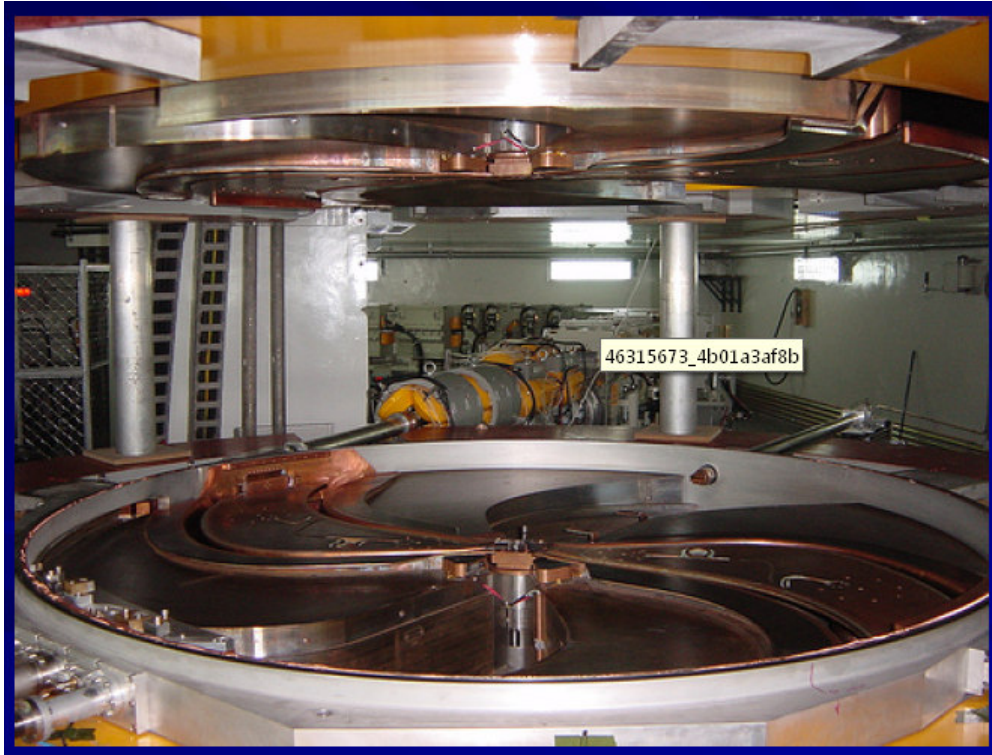
Figure 1.8:235MeV Proton Cyclotron used for Proton Cancer Therapy at Boshan ,China
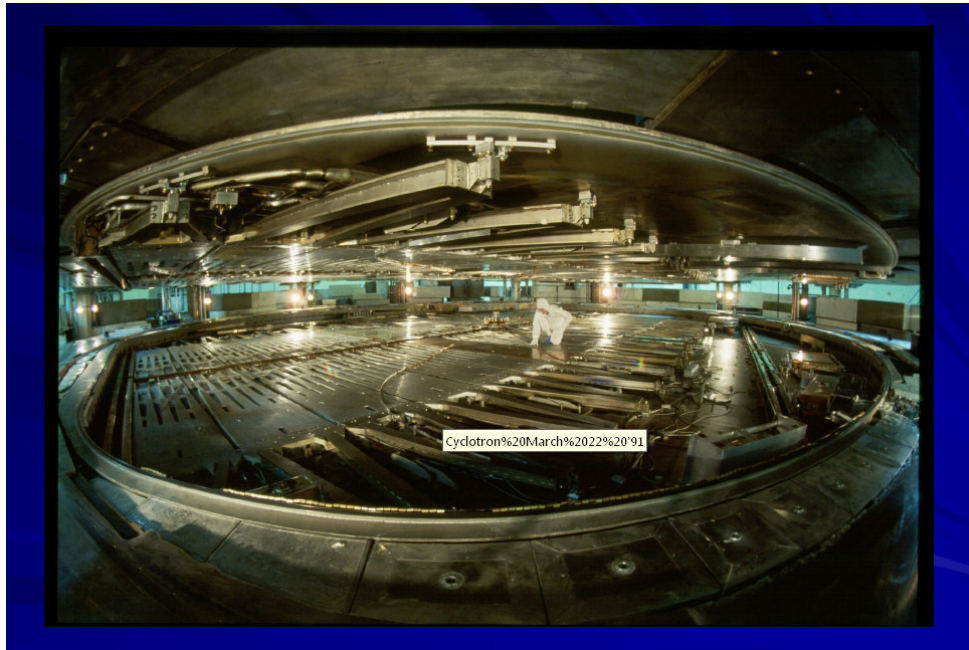

Figure 1.9: Another view of Proton Cyclotron used for Cancer Therapy

Cyclotrons reach an energy limit because of relativistic effects whereby the particles effectively become more massive, so that their cyclotron frequency drops out of synch with the accelerating RF. Therefore simple cyclotrons can accelerate protons only to an energy of around 15 MeV, (corresponding to a speed of roughly 10% of c), because the protons get out of phase with the driving electric field. If accelerated further, the beam would continue to spiral outward to a larger radius but the particles would no longer gain enough speed to complete the larger circle in step with the accelerating RF. Cyclotrons are nevertheless still useful for lower energy applications.

1.5.5 Synchrocyclotrons and isochronous cyclotrons

There are ways of modifying the classic cyclotron to increase the energy limit. This may be done in a continuous beam, constant frequency, machine by shaping the magnet poles so to increase magnetic field with radius. Then higher energy particles travel a shorter distance in each orbit than they otherwise would, and can remain in phase with the accelerating field. Such machines are called isochronous cyclotrons. Their advantage is that they can deliver continuous beams of higher average intensity, which is useful for some applications. The main disadvantages are the size and cost of the large magnet needed, and the difficulty in achieving the higher field required at the outer edge.
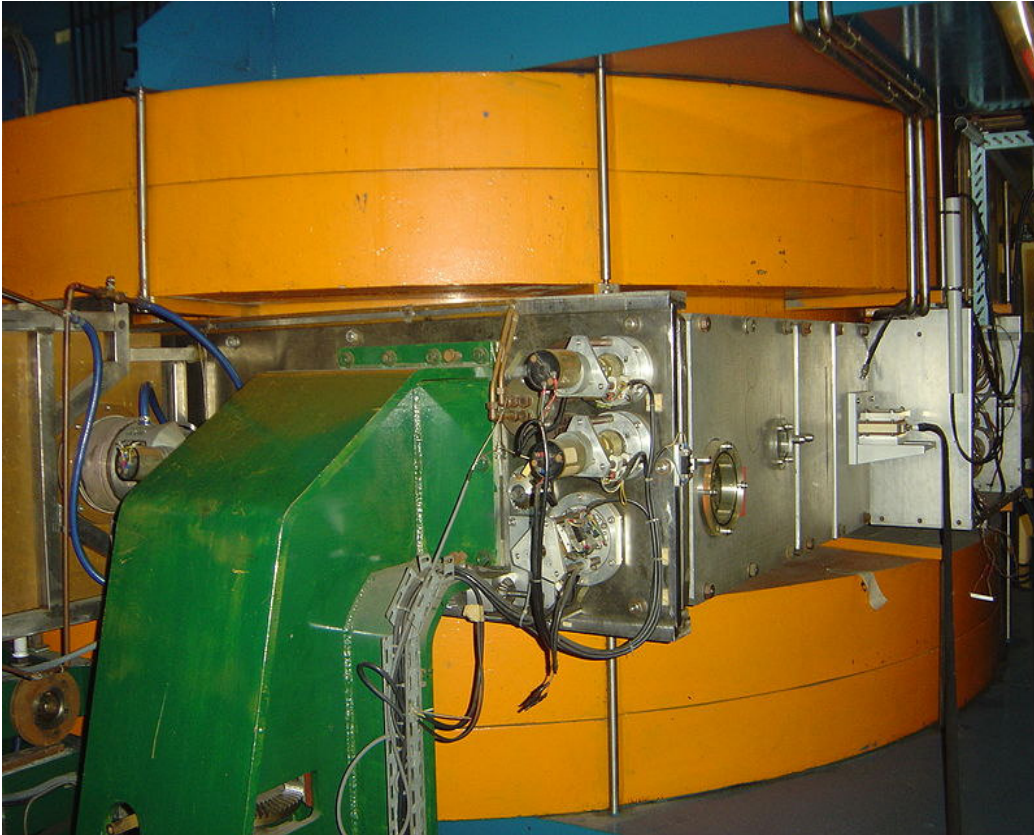
Figure 1.10: A magnet in the synchrocyclotron at the Orsay proton therapy Centre

Another possibility, the synchrocyclotron, accelerates the particles in bunches, in a constant B field, but reduces the RF accelerating field's frequency so as to keep the particles in step as they spiral outward. This approach suffers from low average beam intensity due to the bunching, and again from the need for a huge magnet of large radius and constant field over the larger orbit demanded by high energy.

1.5.6 Betatrons

Another type of circular accelerator, invented in 1940 for accelerating electrons, is the Betatron. These machines, like synchrotrons, use a donut-shaped ring magnet (see below) with a cyclically increasing B field, but accelerate the particles by induction from the increasing magnetic field, as if they were the secondary winding in a transformer, due to the changing magnetic flux through the orbit. Achieving constant orbital radius, while supplying the proper accelerating electric field requires that the magnetic flux linking the orbit be somewhat independent of the magnetic field on the

orbit, bending the particles into a constant radius curve. These machines have in practice been limited by the large radiative losses suffered by the electrons moving at nearly the speed of light in a relatively small radius orbit.

1.5.7 Synchrotrons

To reach still higher energies, with relativistic mass approaching or exceeding the rest mass of the particles (for protons, billions of electron volts GeV), it is necessary to use a synchrotron. This is an accelerator in which the particles are accelerated in a ring of constant radius. An immediate advantage over cyclotrons is that the magnetic field need only be present over the actual region of the particle orbits, which is very much narrower than the diameter of the ring. (The largest cyclotron built in the US had a 184 in dia magnet pole, whereas the diameter of the LEP and LHC is nearly 10 km. The aperture of the beam of the latter is of the order of centimeters.)

However, since the particle momentum increases during acceleration, it is necessary to turn up the magnetic field B in proportion to maintain constant curvature of the orbit. In consequence synchrotrons cannot accelerate particles continuously, as cyclotrons can, but must operate cyclically, supplying particles in bunches, which are delivered to a target or an external beam in beam "spills" typically every few seconds.

Since high energy synchrotrons do most of their work on particles that are already traveling at nearly the speed of light c, the time to complete one orbit of the ring is nearly constant, as is the frequency of the RF cavity resonators used to drive the acceleration.

Note also a further point about modern synchrotrons: because the beam aperture is small and the magnetic field does not cover the entire area of the particle orbit as it does for a cyclotron, several necessary functions can be separated. Instead of one huge magnet, one has a line of hundreds of bending magnets, enclosing (or enclosed by) vacuum connecting pipes. The design of synchrotrons was revolutionized in the early 1950s with the discovery of the strong focusing concept.The focusing of the beam is handled independently by specialized quadrupole magnets, while the acceleration itself is accomplished in separate RF sections, rather similar to short linear accelerators. Also, there is no necessity that cyclic machines be circular, but

rather the beam pipe may have straight sections between magnets where beams may collide. be cooled, etc. This has developed into an entire separate subject, called "beam physics" or "beam optics".

Figure 1.11: Aerial photo of the Tevatron at Fermilab.

More complex modern synchrotrons such as the Tevatron, LEP, and LHC may deliver the particle bunches into storage rings of magnets with constant B, where they can continue to orbit for long periods for experimentation or further acceleration. The highest-energy machines such as the Tevatron and LHC are actually accelerator complexes, with a cascade of specialized elements in series, including linear accelerators for initial beam creation, one or more low energy synchrotrons to reach intermediate energy, storage rings where beams can be accumulated or "cooled" (reducing the magnet aperture required and permitting tighter focusing;and a last large ring for final acceleration and experimentation.

1.5.8 History of Conventional particle accelerators.

Lawrence's first cyclotron was a mere 4 inches (100 mm) in diameter. Later he built a machine with a 60 inches dipole face, and planned one with a 184-inch diameter, which was, however, taken over for World War II-related work connected with uranium isotope separation; after the war it continued in service for research and medicine over many years.

The first large proton synchrotron was the Cosmotron at Brookhaven National Laboratory, which accelerated protons to about 3 GeV. The Bevatron at Berkeley, completed in 1954, was specifically designed to accelerate protons to sufficient energy to create antiprotons, and verify the particle-antiparticle symmetry of nature, then only strongly suspected. The Alternating Gradient Synchrotron (AGS) at Brookhaven was the first large synchrotron with alternating gradient, "strong focusing" magnets, which greatly reduced the required aperture of the beam, and correspondingly the size and cost of the bending magnets. The Proton Synchrotron, built at CERN, was the first major European particle accelerator and generally similar to the AGS.

The Fermilab Tevatron has a ring with a beam path of 4 miles (6 km). The largest circular accelerator ever built was the LEP synchrotron at CERN with a circumference 26.6 kilometers, which was an electron/positron collider. It has been dismantled and the underground tunnel is being reused for a proton collider called the LHC, due to start operation in at the end of July 2008. However, after operating for a short time, 100 of the giant superconducting magnets failed and the LHC had to shut down in September 2008.

According to a press release from CERN that was printed in Scientific American "the most likely cause of the problem was a faulty electrical connection between two magnets, which probably melted at a high current leading to mechanical failure."

An apparent later report by the BBC said "On Friday, a failure, known as a quench, caused around 100 of the LHC's super-cooled magnets to heat up by as much as 100 degrees." This was later described as a "massive magnet quench".

This caused a rupture of a high magnitude – leaking one ton of liquid helium into the LHC tunnels. The liquid helium is used for more efficient use of power and the super cooling of the liquid helium allows the electrical resistance of the superconducting magnets to be nonexistent – zero ohms. According to the BBC, before the accident its operating temperature was 1.9 kelvins (−271 °C; −456 °F)—which is colder than deep space.

The aborted Superconducting Super Collider (SSC) in Texas would have had a circumference of 87 km. Construction was started in 1991, but abandoned in 1993. Very large circular accelerators are invariably built in underground tunnels a few metres wide to minimize the disruption and cost of building such a structure on the surface, and to provide shielding against intense secondary radiations that may occur. These are extremely penetrating at high energies.

Current accelerators such as the Spallation Neutron Source, incorporate superconducting cryomodules. The Relativistic Heavy Ion Collider, and Large Hadron Collider also make use of superconducting magnets and RF cavity resonators to accelerate particles.

1.6 Why Laser Based Proton Radiotherapy

In radiation therapy, the use of proton beams provides the possibility of better dose conformity to the treatment target and normal tissue sparing compared to commonly used photon beams because of the lower entrance dose, sharper penumbra and rapid fall off beyond the treatment depth, which result from the Bragg peak in the dose distribution. Despite the dosimetric superiority and some encouraging clinical results for well-localized radio-resistant lesions, the utilization of proton therapy has lagged behind therapies using photons and electrons because the facilities of proton therapy employing cyclotron and synchrotron technology are expensive and complex. As a result, proton therapy has not been a widespread modality in radiation therapy. This

situation can be improved if a compact and economical proton therapy unit becomes available.

1.6.1 Tabletop Laser proton accelerator Design

Laser acceleration of particles was first proposed in 1979 for electrons. Rapid progress has been made in laser-electron acceleration in the 1990s since the advent of chirped pulse amplification (CPA) and high fluence solid-state laser materials such as Ti:sapphire. Recently, there have been a number of experimental investigations, which observed protons with energies of several tens of MeV. A recent experiment conducted at Lawrence Livermore National Laboratory reported particles with a maximum energy of 58 MeV. The mechanism for laser-proton acceleration is under study. It has been long linked to the longitudinal electric field created as a result of laser-matter interaction.

Need for (from previous section) new laser proton accelerators.

A typical laser-proton system design includes three types of components:

1- a compact laser-proton source to produce high-energy protons,

2-a compact particle selection and beam collimating device for accurate beam delivery, and

3- a treatment optimization algorithm to achieve conformal dose distributions using laser-accelerated proton beams.

Chapter 2

Potential Applications of Laser Produced Protons

2.1- Cancer Therapy

With more than 30,000 patients worldwide with successful clinical results, proton and hadrons therapies are still emerging, but represent promising methods for the specific treatment of deep tumours and radio-resistant cancers. However, although this treatment is expanding considerably (more than 20 new projects are under consideration worldwide), its use is still strongly limited owing to the size and cost of the infrastructure, which exceeds 100M euros. The infrastructure requirements, which include accelerator, beam lines, massive gantries of more than 100 tons and building, are not accessible to the majority of radiotherapy centres. With the outstanding progress in laser physics and fast development of high-power laser systems, several laser-based projects have emerged with the goal of reducing the cost of proton therapy treatment. These costs could be cut, not only by changing the accelerator itself (commercial accelerators that deliver stable and reliable 200MeV protons beams cost about 10Me), but mainly because the building footprint would be strongly reduced, and the gantry could be replaced by a smaller and lighter structure. Several severe conditions have to be met before considering such an approach for medical applications. It is necessary to

(1) increase the proton energy up to 200MeV, for which petawatt class lasers will probably be required

(2) have enough protons at this energy to treat patients in sessions of a few minutes, for which

high repetition rates (10 Hz) could be needed,

(3) have a reliable and stable laser–plasma accelerator.

The dose requirement and dose profile could be achieved with particle selectors or structured targets. This promising application is also extremely challenging, as it requires the development of high-contrast, peta-watt lasers operating at 10 Hz, as well

as dedicated research activities in target design and high-intensity interaction. In a related field, lower energy protons of several mega-electronvolts delivered with compact cyclotron machines of a few MeV are used to produce radioisotopes for medical diagnostics.

2.2 Single Proton Emission Computed Tomography (SPECT)

Proton Emission: (also known as proton radioactivity) is a type of radioactive decay in which a proton is ejected from a nucleus. Proton emission can occur from high-lying excited states in a nucleus following a beta decay, in which case the process is known as beta-delayed proton emission, or can occur from the ground state (or a low-lying isomer) of very proton-rich nuclei, in which case the process is very similar to alpha decay. For a proton to escape a nucleus, the proton separation energy must be negative - the proton is therefore unbound, and tunnels out of the nucleus in a finite time. Proton emission is not seen in naturally-occurring isotopes; proton emitters can be produced via nuclear reactions, usually utilising some kind of particle accelerator.

Single proton emission computed tomography (SPECT) allows a physician to see three-dimensional images of a person's particular organ or body system. SPECT detects the course of a radioactive substance that is injected, ingested, or inhaled. In neurology, a SPECT scan is often used to visualize the brain's cerebral blood flow and thereby, indicate metabolic activity patterns in the brain.

Purpose

SPECT can locate the site of origin of a seizure, can confirm the type of seizure that has occurred, and can provide information that is useful in the determination of therapy. Other uses for SPECT include locating tumours, monitoring the metabolism of oxygen and glucose, and determining the concentration of neurologically relevant compounds such as dopamine.

Currently, a clinical trial is underway in the United States to evaluate the potential of SPECT to study brain receptors for the neurotransmitter acetylcholine. The study will

help to determine the usefulness of the technique in charting the progress of the brain deterioration associated with

2.3 Spot Scanning

Protons are charged particles. As opposed to photons, they can be easily and quickly focused and deflected by the action of magnetic fields under computer control. This opens the possibility for the fast dynamic scanning of a proton pencil beam to provide three-dimensional dose conformation as a completely automated routine therapy.

The figures below describe the principle of the spot scanning technique. The dose is deposited by scanning the dose "spot" delivered by a focused proton pencil beam in all three dimensions inside the patient body.

The dose distribution delivered to tissues by a proton pencil beam retains much of the original shape of the undisturbed beam until the protons stop. At the Bragg peak position the dose reaches its maximum. The hot-spot of dose is well localised in space in all three dimensions. The figure below shows the dose distribution of a single static proton pencil beam (a "dose spot").
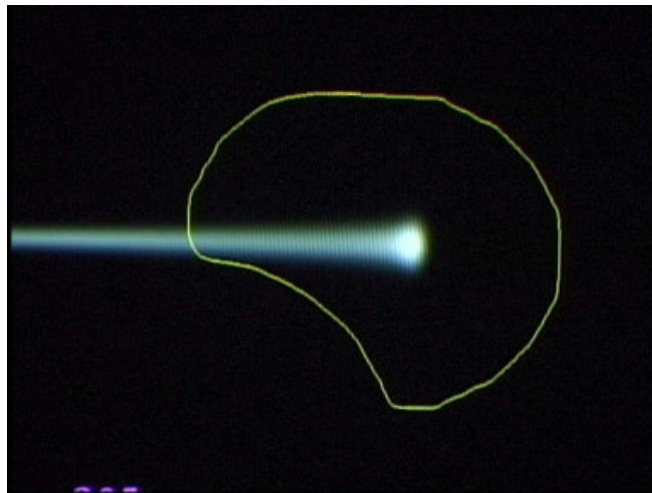
Through the superposition of a very large number of such individual elementary static dose applications, a total conformation of the dose to the target volume can be achieved.

Example: ... a few spots
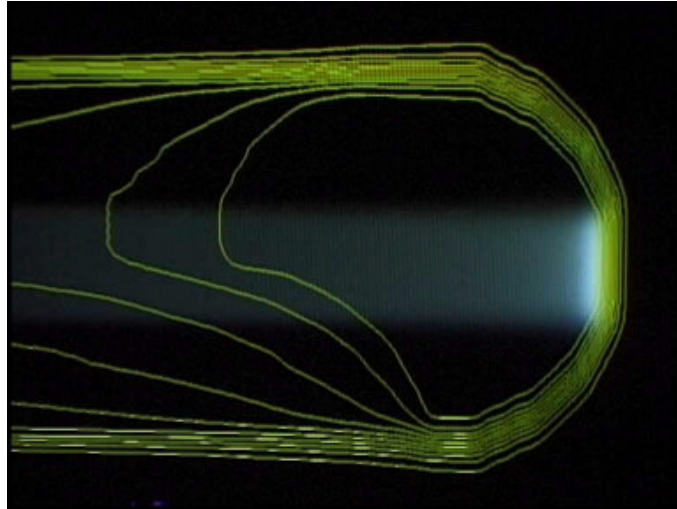
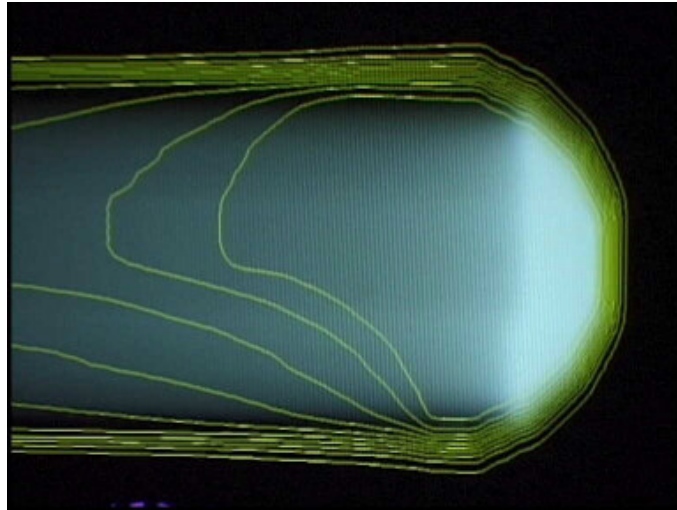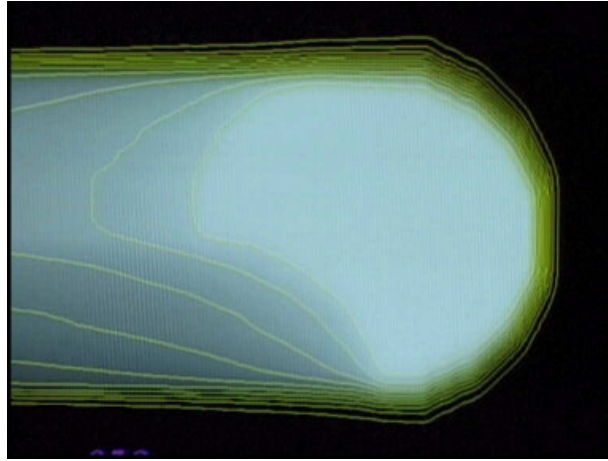... more

... until it is all done.

2.4 P-Beam Writing (Industrial Application)

A number of processes have been developed for the production of x-ray masks. Because of the large thickness required, typically a two step process is carried out, where first an intermediate and relatively thin mask is produced either by electron beam writing or by a photolithographic process, e.g. laser direct writing or UV or EUV lithography. This intermediate mask is then used in a (soft) X-ray lithographic step to transfer the features onto the final thick mask without significant loss of structural quality. Obtaining deep sub micron resolution in X-ray lithography requires features down to several hundred nanometres in a metal absorber mask, featuring high aspect ratios.

Proton beam writing is a new direct write lithography technique for fabricating high aspect ratio structures. The slowing-down and ensuing energy deposition of energetic charged particles (e.g. MeV protons) impinging on and penetrating into solids is governed by the Coulomb interaction of the incident particle with the electrons and nuclei of the target. In e-beam writing as well as p-beam writing the stopping is dominated by substrate electrons. Low proximity effects coupled with the characteristic straight trajectory and high penetration of the proton beam enables the production of high density 3D micro and nanostructures with well defined smooth side walls to be directly written into resist materials.

It has applications in nano-fluidics, biomedical research, and it directly relates with Proton beam with medical applications

2.5 Isochoric Heating

For EOS studies plasmas with uniform densities and single temperatures are required. However when a material is heated at a temperature of several eV, pressures of more than Mbar are induced, causing the plasma to expand. In this case measurement of plasma properties are extremely difficult. One way to overcome this problem is by Isochoric heating with sub-picoseconds laser pulses or proton beams at temperature of eV upto few tens of eV and solid densities. These values cannot be obtained from experiments and therefore a characterisation of these plasma states is very important for EOS researchers. Lasers are limited in their penetration depth of solid matter to a few micron skin depth, therefore, only a thin surface laser is directly heated, while the inner part of the sample is heated on a longer timescale by heat conduction. MeV Protons have a penetration depth of a few microns and are more attractive for volumetric heating.

With the advent of multi-TW ultrashort laser pulses, proton beams are produced by irradiating thin solid targets with 100fs, 5×10^{20} W/cm^2. Upto 10^{11}-10^{13} protons per laser pulse, originating from hydrocarbons found in surface contaminations on the target back surface, are emitted with energies upto 20-50 MeV, from a spot of 200 um. The duration of the proton beam is a few times larger than the duration of the laser pulse. The conversion efficiency of the laser energy to protons ranges between 2% and 7%.The protons are emitted in a cone with a half angle of 15°- 20° .These energetic protons beams were discovered recently (Clark et al;2000'Snavely et al;2000) and are now produced at TW laser facilities.

Recent progress in laser matter interaction makes it possible to produce high currents of protons with energies spanning the spectrum from few hundreds of electron volts up to several tens of MeV. M. Borghesi, J. Fuchs, S.V. Bulanov, A.J. Mackinnon, P. Patel and M. Roth, Fusion Sci. Technol. 49 (2006), p. 412. View Record in Scopus |Cited By in Scopus (87.These proton beams present a promising source for volumetric heating.

The mechanism used to generate the proton beam employs a high intensity ultra-short laser pulse incident on a thin metallic foil that accelerates, via ponderomotive force, electrons from the interaction region into the foil with relativistic velocities. The electrons emerging at the target rear surface induce a large electrostatic charge separation field which accelerates positive ions from the rear surface up to multi-MeV energies. The spectrum is dominated by protons originating from hydrocarbon contaminant layers which outrun the lower charge to mass ratio ions and screen the accelerating field. The proton signal is approximately two orders of magnitude larger than the signal from the heavier ions. Being produced in a very short time (few ps) the protons can deposit energy potentially in a shorter time scale than the expansion time of matter heated to a few eV, allowing for the possibility to create isochoric heating over a large volume of matter. This technique allows one to produce sufficiently large volumes of WDM to permit quantitative observation, thus opening the way for measurements of WDM parameters, stopping power, equation of state etc

2.6- Proton Based Fast Ignition

The minimum requirements for high fusion gain using the fast ignition (FI) approach to inertial confinement fusion (ICF) are relatively well understood , and some are similar to conventional hotspot ICF. The assembled fuel must satisfy certain requirements. In order to keep the amount of DT fuel and the yield at a manageable level, the fuel must be compressed to a mass density in the range $\rho = 300–500$ g/cc, which requires a high-quality capsule implosion. Achieving a high DT burn-up fraction for high efficiency requires an areal density $\rho r \approx 3$ g/cm^2. In order to ignite the DT fuel, the FI particle beam must deposit at least $E_{FI} \sim 10$ kJ (the energy requirement) in a hot-spot volume with a linear dimension of ~ 25 μm (the volume requirement), within $\tau \sim 20 – 50$ ps (the power requirement).The FI power requirement makes particle beams driven by high energy, short pulse (~ps) lasers attractive. Such lasers can drive beams of electrons, protons or heavier ions, all in principle suitable for FI . (Hereon, "ion beam" includes protons, unless otherwise specified.) For a given conversion efficiency ε of laser to particle energy, the energy requirement implies that the laser energy must be $E_L > E_{FI} /\varepsilon$. Such beams are born with duration of the order of laser pulse, but with a finite energy spread. When the beam is created close to the compressed fuel (e.g. with electrons), the power

requirement is just a laser power requirement. For ions, the acceleration mechanism requires a shortpulse laser target that is distinct from the capsule, and whose integrity needs to be protected during the capsule implosion. In practice, this requires a short-pulse laser target placed away from the capsule.

In that limit, for a given total beam energy, the power requirement and the ion energy spread result in a trade-off of distance & energy spread because the longer the beam drifts on its way to the fuel, the more it spreads in time, until the power requirement is not met - the fuel disassembles before it ignites. Therefore, the smaller the ion energy spread, the farther the ion source can be placed (with obvious target fabrication advantages) and the smaller the total beam energy can be.

The particle range has to be adjusted to the fuel ρr for maximum efficiency, which sets the ideal energy for the beam particle EP. For electrons, it is EP ~ 1 MeV, for protons it is $E_P \sim 13$ MeV, while for C ions it is EP ~ 440 MeV. The ion stopping is calculated using the code ISAAC (Ion Stopping At Arbitrary Coupling). ISAAC accounts for plasma effects, which yields significantly different results than stopping in cold matter. The beam particle energy is related to the laser intensity. Based on ponderomotive scaling, 1MeV electrons requires $I_L \sim 5\text{x}10^{19}$ W/cm2. The TNSA process requires $\sim 10^{20}$ W/cm^2 for 13MeV protons, In the case of C, $\sim 10^{21}$ W/cm^2 is required (explained below). Finally, E_{FI} and E_P set the required number of beam particles, N_P. N_P is $\sim 10^{14}$ for C and 10^{16} for protons. NP is not a concern *per se* for electrons, but it can be for ions.

2.7 Proton Diagnostics

2.7.1 Proton Radiography

Proton radiography in terms of radiation dose, imaging speed, image quality (density and spatial resolution) and image content under clinical conditions is very fisible. Protons with ~250 MeV energy can penetrate through most patients and is used for imaging. The measured residual range (or energy) of the protons behind the patient was subtracted from the range without an object in the beam path and used to create a projected image."

Proton radiography is a new technology for imaging the interior of objects that can be penetrated by high-energy protons. A broad beam of high-energy protons shines through the object, and suffers path-dependent attenuation by collisions with the nuclei. It also suffers path dependent spread in angle by multiple Coulomb scattering (MCS). The protons exit the object with an assortment of energies due to the losses on the varying paths through the object. The net effect is that an image is imprinted in the exit beam by its passage through the object. A magnetic lens after the object extracts the implicit image

by refocusing the varied scattering angles onto a detector plane, where it is recorded by a set of gated TV cameras.

2.7.2 Proton Probing of E and B fields

The use of laser-accelerated protons as a particle probe for the detection of electric fields in plasmas has led in recent years to a wealth of novel information regarding the ultrafast plasma dynamics following high intensity laser-matter interactions. The high spatial quality and short duration of these beams have been essential to this purpose.

The development of proton probing techniques has provided a very powerful tool to explore the fast dynamics of laser produced plasmas (Mackinnon et al., 2004; Romagnani et al., 2005). In these techniques, a laser-accelerated proton beam is employed as a charged particle probe for the electric and magnetic fields generated in laser-plasma interactions. Thanks to the high quality of such proton probes, and in particular to their high degree of laminarity (Cowan et al., 2004), short burst duration and broad spectral content, detailed (spatial resolution in the mm range) time-resolved (temporal resolution in the ps range) maps of the fields and charge density and/or current density distributions in the probed plasma can be obtained (Mackinnon et al., 2004; Romagnani et al., 2005).

Chapter 3: Laser Plasma Interaction and Particle Acceleration

3.1 Laser

The name LASER is an acronym for Light Amplification by the Stimulated Emission of Radiation. In 1917, Albert Einstein first theorized about the process which makes lasers possible called "Stimulated Emission."

3.1.1 Ultra-short Pulses

Optical pulses as generated in mode-locked lasers can be extremely short, particularly for passive mode locking. There is no commonly accepted definition of "ultrashort", but usually this label applies to pulses if their pulse duration is at most a few tens of picoseconds, and often in the range of femtoseconds.

Note that ultrashort pulses should not be called "ultrafast" – they are not faster (do not have a higher velocity) than longer pulses. They do, however, make it possible to investigate ultrafast processes (→ *ultrafast optics*), and can be used for fast optical data transmission. In the latter case, "fast" means a high data rate, not actually a high velocity.

Ultrashort pulses are usually generated with passively mode-locked lasers, but sometimes also with optical parametric amplifiers (possibly using a supercontinuum as input) or with free electron lasers. It is also possible to start with longer pulses and apply some method of pulse compression.
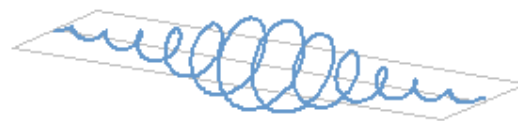
3.1.2 Polarization

it is defined as the direction of the electric field oscillation of a laser beam,In my experiments I used linearly polarized laser output , where the electric field oscillates in a certain (stable) direction perpendicular to the propagation direction of the laser beam.
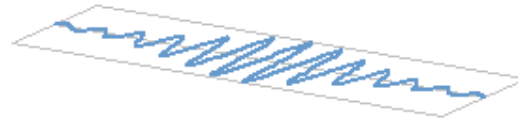
horizontal linear polarization
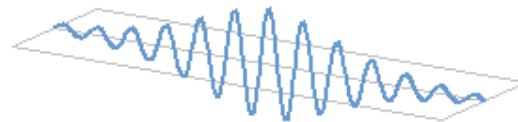
vertical linear polarization

left circular polarization
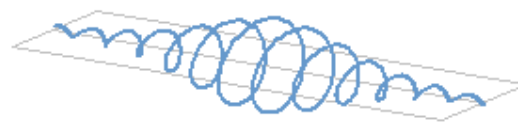
right circular polarization

Figure 3.1: Different polarization states of laser emission, illustrated for a few-cycle pulse propagating from left to right.

3.2 Chirped Pulse amplification(CPA)

Remarkable progress in the development of high power femtosecond pulses and their application has been achieved since the introduction of Chirped pulse amplification (CPA), is a technique for amplifying an ultrashort laser pulse up to the petawatt level with the laser pulse being stretched out temporally and spectrally prior to amplification.

Fig 3.2: History of laser output power density growth
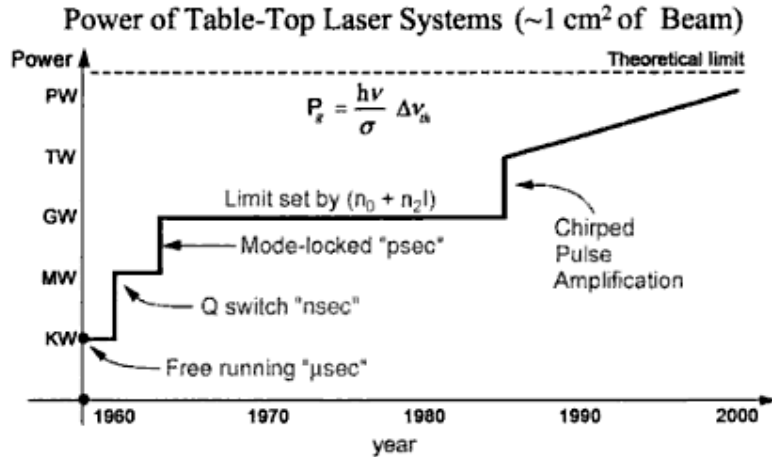
CPA is the current state of the art technique which all of the highest power lasers (greater than about 100 terawatts, with the exception of the ~ 500 TW National Ignition Facility) in the world currently utilize. Some examples of these lasers are the Vulcan Petawatt Upgrade at the Rutherford Appleton Laboratory's central laser facility, the Gekko Petawatt laser at the Gekko XII facility in the Institute of Laser Engineering at Osaka University, the OMEGA EP laser at the University of Rochester's Lab for Laser Energetics and the now dismantled petawatt line on the former Nova laser at the Lawrence Livermore National Laboratory. Apart from these state-of-the-art research systems, a number of commercial manufacturers sell Ti:sapphire-based CPAs with peak powers of 100 TW.
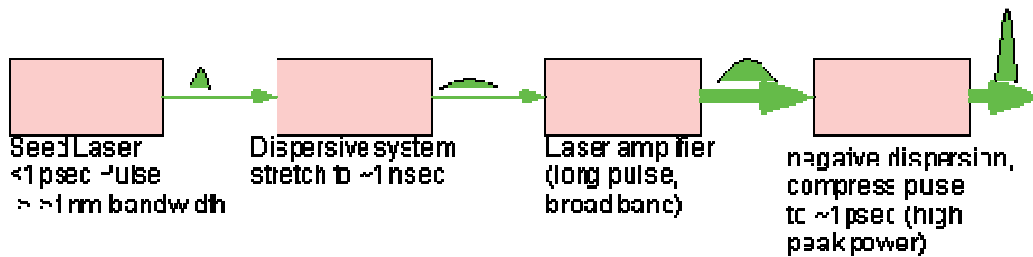

Fig 3.3: Showing CPA

CPA was invented by Gérard Mourou and Donna Strickland at the University of Rochester in the mid 1980. Before then, the peak power of laser pulses was limited because a laser pulse at intensities of gigawatts per square centimeter causes serious damage to the gain medium through nonlinear processes such as self-focusing. For

example, some of the most powerful compressed CPA laser beams, even in an unfocused large aperture (after exiting the compression grating) can exceed intensities of 700 gigawatts/cm2, which if allowed to propagate in air or the laser gain medium would instantly self focus and form a plasma or cause filament propagation, both of which would ruin the original beam's desirable qualities and could even cause back-reflection potentially damaging the laser's components. In order to keep the intensity of laser pulses below the threshold of the nonlinear effects, the laser systems had to be large and expensive, and the peak power of laser pulses was limited to the high gigawatt level or terawatt level for very large multi beam facilities.

In CPA, on the other hand, an ultrashort laser pulse is stretched out in time prior to introducing it to the gain medium using a pair of gratings that are arranged so that the low-frequency component of the laser pulse travels a shorter path than the high-frequency component does. After going through the grating pair, the laser pulse becomes positively chirped, that is, the high-frequency component lags behind the low-frequency component, and has longer pulse duration than the original by a factor of 103 to 105. Then the stretched pulse, whose intensity is sufficiently low compared with the intensity limit of gigawatts per square centimeter, is safely introduced to the gain medium and amplified by a factor 106 or more. Finally, the amplified laser pulse is recompressed back to the original pulse width through the reversal process of stretching, achieving orders of magnitude higher peak power than laser systems could generate before the invention of CPA.

In addition to the higher peak power, CPA makes it possible to miniaturize laser systems (the compressor being the biggest part). A compact high-power laser, known as a tabletop terawatt laser (T3 laser), can be created based on the CPA technique.

3.2.1 Stretcher and Compressor

There are several ways to construct compressors and stretchers. However, a typical Ti:sapphire-based chirped-pulse amplifier requires that the pulses are stretched to several hundred picoseconds, which means that the different wavelength components must experience about 10 cm difference in path length. The most practical way to achieve this is with grating-based stretchers and compressors. Stretchers and compressors are characterized by their dispersion. With negative dispersion, light with

higher frequencies (shorter wavelengths) takes less time to travel through the device than light with lower frequencies (longer wavelengths). With positive dispersion, it is the other way around. In a CPA, the dispersions of the stretcher and compressor should cancel out. Because of practical considerations, the stretcher is usually designed with positive dispersion and the compressor with negative dispersion.

3.2.2 Grating Based Stretcher and Compressor

Figure 3.4 shows the simplest grating configuration, where long-wavelength components travel a larger distance than the short-wavelength components (negative dispersion). Often, only a single grating is used, with extra mirrors such that the beam hits the grating four times rather than two times as shown in the picture. This setup is normally used as a compressor, since it does not involve components that could lead to unwanted side-effects when dealing with high-intensity pulses. The dispersion can be tuned easily by changing the distance between the two gratings.
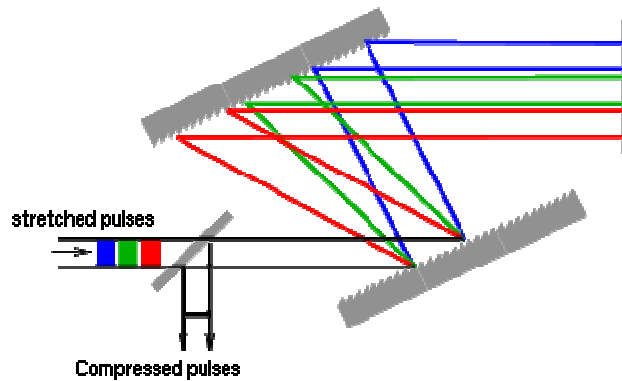

Fig 3.4: Schematic layout of a grating-based compressor with negative dispersion, i.e. the short wavelengths (in blue) come out first.

Figure 3.5 shows a more complicated grating configuration that involves focusing elements, here depicted as lenses. The lenses are placed at a distance 2f from each other (they act as a 1:1 telescope), and at a distance L from the gratings. If L < f, the setup acts as a positive-dispersion stretcher and if L > f, it is a negative-dispersion stretcher. And the case L = f is used in the pulse shaper. Usually, the focusing element is a spherical or cylindrical mirror rather than a lens. As with the configuration in Figure 3.5, it is possible to use an additional mirror and use a single grating rather than two separate ones. This setup requires that the beam diameter is very small compared to the length of the telescope; otherwise undesirable aberrations will be

introduced. For this reason, it is normally used as a stretcher before the amplification stage, since the low-intensity seed pulses can be collimated to a beam with a small diameter.
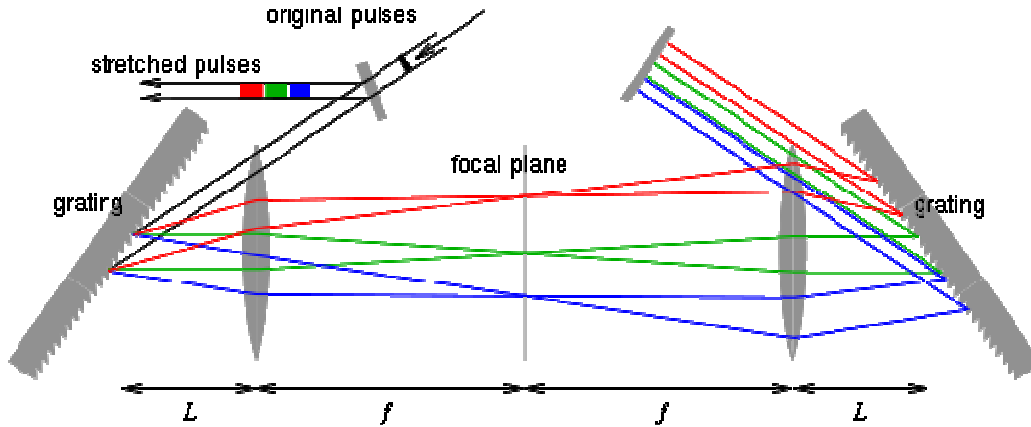

Fig 3.5: Schematic layout of a grating-based stretcher. In this case, L < f, which leads to a positive dispersion, i.e. the long wavelengths (in red) come first.

3.2.3 Amplified Spontaneous Emission – contrast

The intensity contrast of an ultra-high intensity laser pulse is an important parameter in laser-plasma interactions. The contrast is defined as the ratio between the intensity of the main pulse and the intensity of the pedestal that precedes it. Typically, the intensity contrast is quoted at two values, one where the main pulse is compared with the pedestal intensity tens of picoseconds prior to the main pulse, and the other where the pedestal intensity nanoseconds before the main pulse is used. A poor or low level contrast pulse results in target preheating and shock disruption of thin targets before the main part of the pulse arrives. This affects the laser-target interaction. The higher the peak intensity of the main pulse the higher the contrast needs to be to minimise these effects.

The main factors that affect the contrast of a laser system is the amplified spontaneous emission, where stray laser light is amplified, and uncompensated dispersion, a part of the main pulse that was not fully compressed. Fig. shows schematically the different components that a laser pulse is typically composed of. The length of the ASE pedestal is determined mainly by pockel cell gating and the uncompensated dispersion is of the order of the uncompressed main pulse.
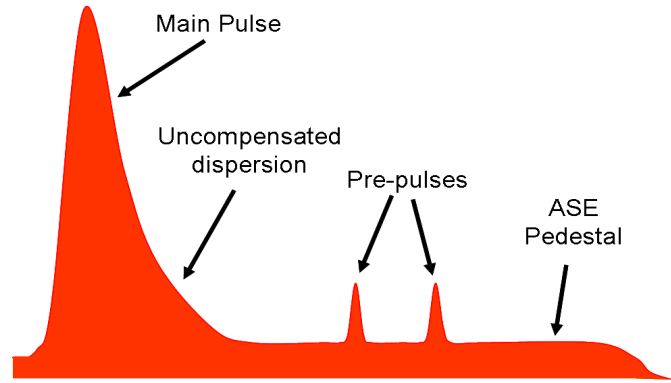
Figure 3.6

Schematic of a high intensity laser pulse propagating from left to right. Propagating ahead of the main pulse is the ASE pedestal, pre-pulses and the uncompensated dispersion. All three components will lead to the generation of a pre-plasma at the target surface before the main pulse arrives on target. The contrast on a nanosecond time scale can be measured using a fast diode and on a picosecond time scale is typically measured with a third order autocorrelator.

3.2.5 The Ponderomotive Force

The ponderomotive force is a nonlinear force that a charged particle experiences in an inhomogeneous oscillating electromagnetic field.

The ponderomotive force F_p is expressed by

$$\mathbf{F}_p = -\frac{e^2}{4\,m\,\omega^2}\nabla \mathbf{E}^2$$

........................3.1

where e is the electrical charge of the particle, m is the mass, ω is the frequency of oscillation of the field, and E is the amplitude of the electric field (at low enough amplitudes the magnetic field exerts very little force).

This equation means that a charged particle in an inhomogeneous oscillating field not only oscillates at the frequency of ω but also drifts toward the weak field area. It is

noteworthy that this is one rare case where the sign of the particle charge does not change the direction of the force, unlike the Lorentz force.

The mechanism of the ponderomotive force can be easily understood by considering the motion of the charge in an oscillating electric field. In the case of a homogeneous field, the charge returns to its initial position after one cycle of oscillation. In contrast, in the case of an inhomogeneous field, the position that the charge reaches after one cycle of oscillation shifts toward the lower field-amplitude area since the force imposed onto the charge at the turning point with a higher field amplitude is larger than that imposed at the turning point with a lower field amplitude, thus producing a net force that drives the charge toward the weak field area.

3.3 Plasmas

The plasma state is a state of matter where components are no more neutral; this is usually reached when a bulk is heated to a point where its internal energy is higher than one or more ionization levels, which makes the single atoms to lose electrons in collisions. A plasma can be locally created by ionizing a certain amount of material, like in discharge tubes, heating a rarefied gas with microwaves or by interaction with a laser. The vast set of parameters, in temperature, pressure, density, neutrality makes the plasma state one of the most various chapter of the physics.

Collective parameters In a plasma, for each of the species α, it is defined the α-plasma frequency

$$\omega_{p\alpha} = \sqrt{\frac{n_\alpha q_\alpha^2}{\varepsilon_0 m_\alpha}}$$

……………..3.2

which is the oscillating frequency of the α component. This is a key parameter for evaluating the response timescale of the α-plasma to external fields. When a separation of charges is produced, the motion of the α component to restore the neutrality results in an oscillation at the frequency (3.1).

The free electrons in the plasma are mobile enough that they can "shield" the plasma from external fields so that the bulk plasma remains largely unaffected. This shielding

is called Debye shielding and the sheath around a field source called the plasma sheath. The first criterion for an ionised gas to be treated as a plasma is

$$\lambda_D \ll L$$

where λ_D is the length of the sheath (Debye length) and L is the length of the plasma. λ_D can be calculated using the following

$$\lambda_D \equiv \left(\frac{\varepsilon_0 kT_e}{n_e}\right)^{1/2} = 69\left(\frac{T}{n}\right)^{1/2} = 7430\left(\frac{kT}{n}\right)^{1/2} \quad \ldots\ldots\ldots\ldots..3.3$$

In above equation ε_0 is the permittivity of free space, k is Boltzmann's constant, T_e is the average electron temperature in the plasma, n the density of particles in the plasma and e is the electron charge. In the first practical formula, T is measured in Kelvin while in the second kT is measured in eV.The second criterion is that the charged particles in the plasma must be close enough to exert force on more particles than just its neighbour. The "Debye sphere"is a measure of the number of charged particles N_D within the sphere of influence of a particle at the centre of the sphere and is calculated by:

$$N_D = \frac{4}{3}\pi\lambda_D^2 n \quad \ldots\ldots\ldots\ldots..3.4$$

The second of the criteria regarding collective behaviour is therefore

$$N_D \gg 1$$

The last of the parameters for an ionised gas to be treated as a plasma relates to inter-particle collisions in the plasma itself. If the charged particles collide too frequently with neutrals, then the motion of the charged particles are governed more by hydrodynamic effects rather than electromagnetic forces. If we take ω_p (known as the plasma frequency) i.e. the oscillation frequency of electrons in the plasma and τas the average time between collisions with neutral particles, then for a plasma to act rapidly in shielding out external fields the following must be observed:

$$\omega_p\tau > 1$$

In other words, the collision frequency of particles in the plasma must be far less than

the plasma frequency.

3.3.1 Optical Skin Depth

The depth to which the laser pulse penetrates the target is called the optical skin depth (δ_{opt}), and is dependent on both the material's physical characteristics and the type of radiation incident on it . It can be computed using:

$$\delta_{opt} = \sqrt{2/\omega\mu\sigma} \qquad ……………..3.5$$

In the above, ω is the angular frequency of the laser radiation, μ is the magnetic permeability of the material and σ is the conductivity of the target material.

3.3.2 Plasma created by lasers

The interaction between laser pulses, at a flux over a certain threshold, and supercritical matter (i.e. ω pe > ω laser) produces a plasma. As a general scenario, electrons are heated at first, by the evanescent wave that penetrates the skin depth l_s = c/ω pe, atoms are ionized and a high temperature corona of plasma starts to expand from the area of interaction. The involved mechanisms range depending on the intensity and the duration of the laser pulse.

3.3.3 Matter ionization and plasma creation

When high intensity electromagnetic (em) radiation interacts with matter, electrons start to oscillate accordingly to the forcing electric field. As intensity increases, the field amplitude becomes comparable to the bounding field of the outer electronic shells (or electrostatic potential comparable to the work potential) and nonlinear effects gain in importance. [1, 2, 3]. If no resonant level exists, the direct, single photon, ionization is impossible; when the density of photons is sufficiently high, different ionization mechanisms (nonlinear ionizations) can happen; their small cross section makes them not observable at lower intensities. The relative importance of these cross sections has been extensively studied. The adiabaticity parameter (the Keldysh factor)

$$\gamma_K = \omega/\omega_t = \omega\sqrt{2mW}/eA \qquad \ldots\ldots\ldots 3.6$$

is defined as the ratio between the laser frequency ω and the frequency ω_t of electron tunnelling through a potential barrier. This last comes from the ratio between the electron potential in the oscillating field eA and its ionization momentum $\sqrt{2mW}$, set W the work potential of the level. The value of γ_K defines the main ionization mechanism, as briefly described hereafter in order of increasing field amplitude. Figure 3.7: Non linear ionization: the electron in the potential well can tunnel through the residual potential (red) of is freed by suppression of the barrier (blue)
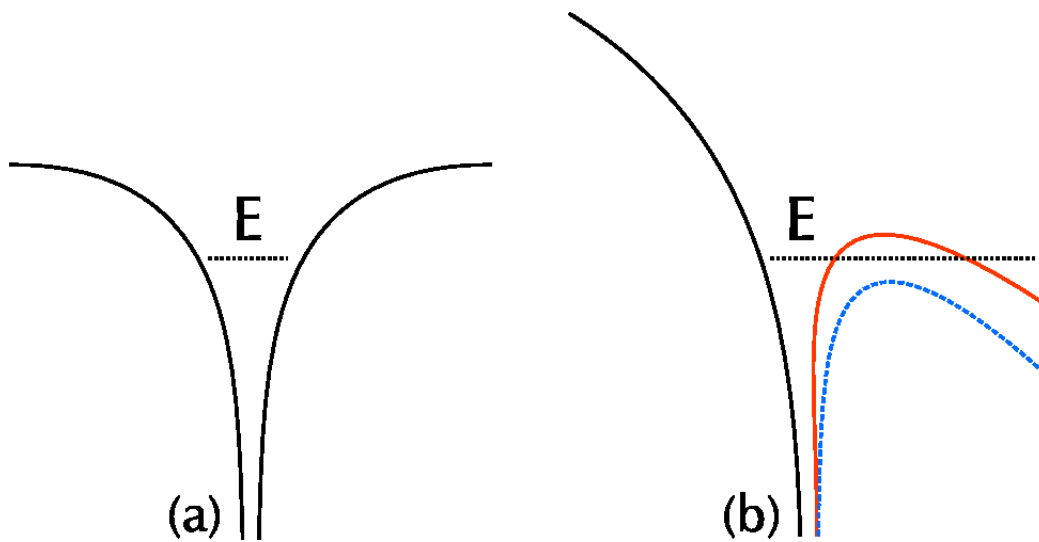

Fig 3.7: Non linear ionization: the electron in the potential well can tunnel throughthe residual potential (red) of is freed by suppression of the barrier (blue)

3.3.4 Multiphoton ionization

For values of $\gamma_K > 1$ the only possible mechanism is the multiphoton ionization. When a sufficient density of photon exists, a bound electron can be freed by the absorption of several photons with an energy lower than the work potential [4, 5, 6]. The typical threshold value ranges between 10^{10}W/cm^2 and 10^{14}W/cm^2. In above-threshold ionization (ATI, [7, 8]) more photons are absorbed than necessary for the ionization. In this case electrons are freed with non-zero energy, and their spectrum shows peaks around multiples on the photon energy, hν.

3.3.5 Tunnel ionization

When $\gamma_K < 1$ the walls of the potential well are deformed in a way that only a finite range of forbidden energies exists for the bound electron. A non-zero probability exists for the electron to tunnel through the potential barrier (Fig.3.7-red).

3.3.6 Suppression of the potential barrier

When the well boundary is deformed to have its maximum lower than the energy of the bound electron (Fig.3.7-blue), no more barrier exists and the electron drifts in the electric field ($\gamma K \ll 1$).

3.3.7 General description of Critical Density

While the plasma is still in its initial stages, a high percentage of light can pass through the plasma and onto the target surface, the laser beam suffers from increasing attenuation as the plasma becomes denser however, due to increasing number of free electrons involved in collisional absorption. This continues until the electron density in the plasma has reached a critical value, the critical density c_n :

$$n_c = \frac{\varepsilon_0 m_e \omega^2}{e^2} = n_c = \frac{m_e \omega^2}{4\pi e^2} \cong 1.1 x 10^{21} (\frac{1\mu m}{\lambda^2}) cm^{-3} \ldots\ldots\ldots 3.7$$

in which m_e is the electron mass, ω is the frequency of the laser radiation, e is the electron charge and λ is the laser wavelength measured in μm. When the plasma density reaches this value, the incident laser radiation is primarily absorbed by the plasma near the critical density zone. In this phase of the laser pulse, the plasma starts to expand rapidly away from the target surface. This expansion reduces the electron density, and laser light is once more able to pass through to the target surface relatively undiminished. This cyclical process continues until the laser pulse ceases – at this point, the plasma no longer has an external energy source, and atomic processes dominate energy transfer in the plasma.

So the wave dispersion for a laser propagating in a plasma shows that as the ω_p approaches the frequency of the laser (ω) the wave vector (k) approaches zero. Hence, at this point the wave is unable to propagate any further and is reflected.

In the relativistic regime n_c increases by a factor of (time dependent) due to the relativistic electron mass increase. This shift in the critical density, which allows the laser to propagate further, occurs due to the laser intensity and is called laser-induced transparency. The n_c is used to describe two different plasma regimes, an underdense plasma is where $n_e < n_c$ and where $n_e > n_c$ the plasma is called overdense.

3.3.8 Laser self-focusing

The refractive index η of a plasma is dependent on the plasma frequency and therefore the electron density and the approximation is defined in Eq 3.6.

$$\eta = \sqrt{1-\left(\frac{\omega_p}{\omega}\right)^2} = \sqrt{1-\frac{n_e}{n_c}} \quad …………………..3.8$$

When a laser is tightly focused into a plasma the ponderomotive force, as discussed earlier, depletes regions of higher laser intensity of their electrons. This inverted distribution of electrons compared to the laser intensity profile results in a refractive index profile with a maximum on the laser axis (point of highest intensity). This refractive index profile, which acts like a convex lens, focuses the laser pulse [30-33] and thereby increasing its intensity further [34, 35]. This process is known as laser self-focusing.

3..3.9 Correlation with the pulse duration

ns pulses

When a nanosecond laser pulse interacts with matter, atoms are ionized by multiphoton ionization and electrons accelerated in the laser electric field. In metals the temperature of electrons in conduction band is strongly increased and new electrons from inner shells are promoted to it. In transparent dielectrics electrons have to be freed before any absorption could take place, and this motivates the higher threshold of damage. In both cases the plasma is produced by collisions between the quivering electrons and the matter at rest. The threshold fluxes for τ_L = 1ns are of the order of $I\tau_L => 1.5 J/cm^2$ for gold and $I\tau_L => 40 J/cm^2$ for fused silica (Fig.3.8). In

71

the ns regime, the laser duration is longer than the characteristic timescale of thermal processes, which brings to the quasi-stationary formation of three areas,
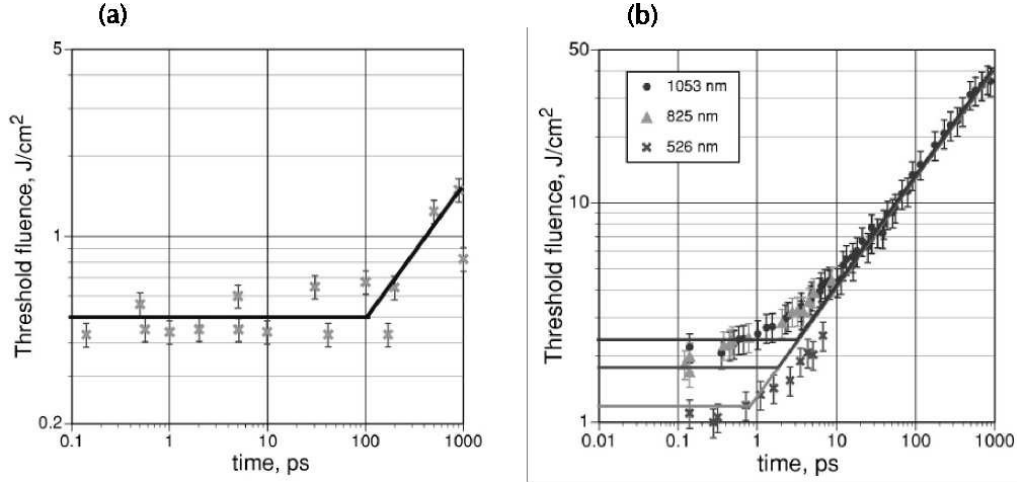

Figure 3.8: Damage thresholds at different pulse length for gold (a) and fused silica (b). (Ref.[27])

namely a corona, a conduction region and a shocked region. In the corona (ne < nc) the laser energy is absorbed by electrons in the plasma at undercritical density 2; in the conduction region (nc < ne < ns) the thermal conduction transports energy from the laser-heated region to the bulk; in the shocked region (ρ > ρs) the matter is compressed to densities higher than the solid (ρs) by conservation of momentum from the expanding motion in the corona (rocket effect). This last effect is responsible for the creation of a shock wave, which propagates towards the unperturbed part of the bulk. During the laser pulse duration, the expansion of the corona in the vacuum can be regarded as isothermal.

sub-ps pulses

When the laser duration is $\tau_L < 1ps$, the interaction process with cold matter changes due to (i) the short duration and (ii) the higher intensities reached. The laser pulse duration is shorter than the characteristic times of electron-to-ion energy transfer, the electron heat conduction and the time of hydrodynamic expansion of the interaction zone. This makes the laser pulse to interact with a solid target where the density remains almost constant. The higher intensities (I~10^{13}–10^{14}W/cm^2 at the threshold) are responsible for almost sudden ionization at the beginning of the laser pulse, not

depending on the nature of the material, metal or dielectric. Ablation of the material can happen for charge separation in the interaction zone. Electrons can gain sufficient energy to escape from the target and drag ions out of it when $(\varepsilon_e > \varepsilon_{work} + \varepsilon_b)$ or can be pushed deeper by ponderomotive force. Where are defined the ε_e electron energy, ε_{work} the electron work potential and ε_b the ion work potential.

The expansion starts once the laser pulse has passed over and it can be regarded as adiabatic, where a plasma front propagates towards the vacuum at a speed of

$$v_p = \frac{2\gamma A^{1/2}}{\gamma A - 1} c_s o \qquad \dots\dots\dots\dots\dots\dots\dots 3.9$$

and the transition between the unperturbed bulk and the shocked region at

$$v_s = -\gamma A^{1/2} c_s o \qquad \dots\dots\dots\dots\dots\dots\dots\dots 3.10$$

Having defined

$$c_s o = \sqrt{\frac{(Z+1)k_B T_i}{A m_i}} \qquad \dots\dots\dots\dots\dots\dots 3.11$$

the isothermal speed of sound in the unperturbed material and γ = 5/3 the adiabatic constant[15].

3.3.10 Electron Heating from UHI lasers and particle acceleration

This thesis falls in the context of the interaction between Ultra High Intensity (UHI) femtosecond lasers and supercritical matter. At relativistic intensities ($I_0 > 10^{18}$W/cm^2) from CPA laser chains the interaction with a ns pedestal at intensities over the ionization threshold, is to be accounted for before the sub-ps peak. The considered situation is then an UHI, sub-ps pulse interacting with a preformed expanding plasma. In this section I focus on the mechanisms of energy transfer between the laser pulse and the existing plasma gradient, which are responsible for the generation of a suprathermal electron population. When the em wave penetrates the plasma gradient, it propagates freely until the critical surface at density

$$n_c = \frac{\varepsilon_0 m_e \omega^2}{e^2} \qquad \dots\dots\dots\dots\dots\dots 3.12$$

which is obtained by equating $\omega = \omega_{pe}$ from (3.1). If the field amplitude is relativistic, the electron plasma frequency is corrected by the increase of the accelerated electron mass (induced transparency), giving

$$\omega'_{pe} = \sqrt{\frac{e}{\gamma}}\,\omega_{pe} \quad \text{…………………………..3.13}$$

The free electrons are made slowly drifting by the $v \times B$ term in the Lorenz force while oscillating in the electric field. The only way to make them gain a net energy from the interaction is to break the adiabaticity of the process, i.e. make them escape the interaction region once they have gained momentum. In a plasma this can happen due to collisionality, wave breaking or steep discontinuities in the density distribution.

3.3.11 Laser absorption

Plasma scale length In many cases the high intensity laser pulse will initially propagate through an underdense plasma before reaching the critical density surface. This underdense plasma is formed before the main pulse arrives by ablation of the target surface due to either laser pre-pulses or a low intensity pedestal preceding the main pulse. The low intensity pedestal has two components; Amplified Spontaneous Emission (ASE) and uncompensated dispersion. ASE is generated by scattered light within the laser system being amplified. The temporal length of the ASE preceding the laser pulse is determined by the gating of the pulse, typically by Pockels cells in the laser system. The uncompensated dispersion is found at the rising edge of the laser pulse and is formed from parts of the pulse not being compressed correctly. This preformed underdense plasma will have a density profile that falls off away from the target and is generally assumed to be an exponential decay:

$$n_e(z) = n_o \exp(-z/L_n) \quad \text{……………….3.14}$$

where z is the distance out from the target surface, n_0 is the initial electron density of the target and L_n is the density scale length. The plasma density scale length is the distance over which the density of the underdense plasma drops by a factor of 1/e, where e is Euler's number. The plasma scale length is important as it is a useful

characterisation of the pre-formed plasma which greatly affects how the laser energy is absorbed. An estimate of the plasma scale length [29] can be found using Eq. 3.15.

$$L_n \approx c_o \tau_L \qquad \text{……………………….3.15}$$

where τ_L is the expansion time and c_0 is the ion sound speed, given by:

$$c_o = \sqrt{\frac{k_B(ZT_e + T_i)}{M_i}} \qquad \text{…………………….3.16}$$

where k_B is Boltzmann's constant, Z is the charge state of the ion, T_e and T_i are the electron temperature and ion temperature respectively and M_i is the ion mass. There are several different mechanisms through which energy is transferred from the laser pulse to the plasma.

3.3.12 Shock wave propagation

The ablation of material from the surface of a target by a laser induces a pressure wave into the un-ablated material of the target to maintain momentum conservation. This launches a shock into the target. The pressure exerted by the ablation of aterial as a function of laser intensity and wavelength can be approximated as [17]:

$$P = 400\left(\frac{I_{cm}}{\lambda_{\mu m}}\right)^{2/3} \qquad \text{……………….3.17}$$

where P is the pressure in Pascals, I_{cm} is the laser intensity in W/cm^2 and $\lambda_{\mu m}$ is the laser wavelength in µm.

The state of material, initially at rest, that has been shocked is governed by the conservation of mass and momentum. The relationship between the shock (v_s) and particle (v_p) velocities and state variables are given in Eqs. 2.31-2.33 [18]. It is assumed that there is no lateral spreading of the shock wave due to the targets being thin (µm) and that the shock wave propagates at a constant velocity.

$$v_s = \frac{c_o}{2\alpha}\left(\sqrt{1+\chi}+1\right) \qquad \text{…………….3.18}$$

$$\upsilon_p = \frac{c_o}{2\alpha}\left(\sqrt{1+\chi}-1\right) \qquad \text{...............}3.19$$

$$\chi = \frac{4\alpha P}{\rho_o c_o^2} \qquad \text{....................}3.20$$

where ρ_o is the initial material density, c_0 is the sound speed and α is an empirical material constant. Lundh et. al. summarises these values for different materials, for example for Al, ρ_o = 2.70 gcm^{-3}, c_0 = 5.24 µm/ns and α = 1.40 [18].

The arrival of a shock at a target rear surface can effect ion acceleration by inducing expansion of the rear surface. For a low temperature shock the velocity of expansion is $v_e = 2v_p$ [18].

3.4 Laser ion acceleration

Two separate mechanisms of laser ion acceleration are at present recognised and confirmed by experiments and PIC simulations: front surface and rear surface acceleration. This last is normally termed TNSA (Target Normal Sheath Acceleration). In this theoretical introduction as well as in proton acceleration experiments, I only focused on protons which acquire a final velocity in the forward direction. A proton beam emerging from the illuminated surface and propagating backwards is found in PIC simulations and experimentally observed by some experimental teams, as a consequence of the plasma expansion from that surface. When using a high contrast laser on very thin targets [19], the backward acceleration conditions are the same as the forward ones, which makes the two spectra and cutoffs comparable.
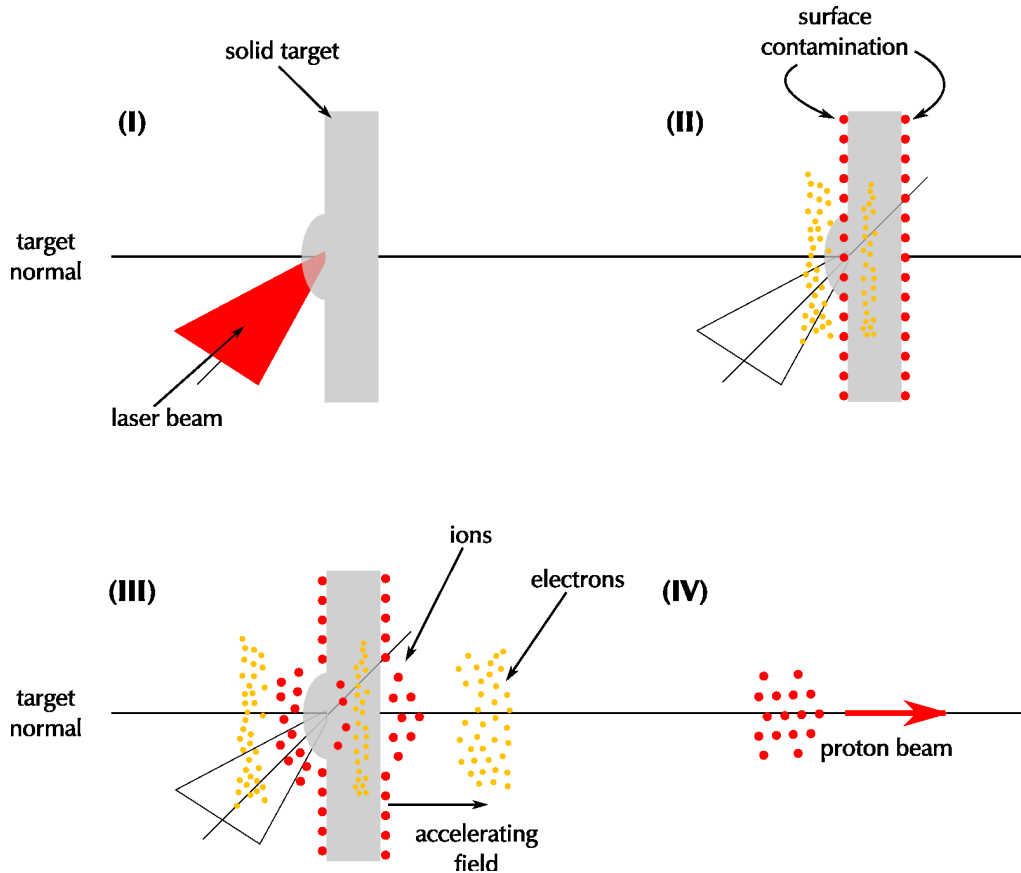
Figure 3.9: Proton acceleration scheme. The UHI laser pulse impinges on a slab of solid matter (I); the matter is ionized and the plasma heated, which produces suprathermal electron population (II). Following the propagation of electrons through the target (III) an electrostatic accelerating field is set up on the rear surface (TNSA), which extracts and accelerates ions from the back surface impurities.

3.4.1 Acceleration from the illuminated surface

Ions are accelerated at the front (illuminated) surface by the charge separation that is induced in the expanding plasma. Depending on the mechanism that dominates in the electron heating, the correlation with laser parameters changes. In cases of normal incidence or s-polarized obliquely incident light, the main charge separation mechanism at relativistic intensities is due to the ponderomotive potential, thus the acceleration gradient lies on the axis of laser propagation [20]; as a consequence of the radial components of the ponderomotive force, a non negligible charge separation on the target normal direction can be however set up. From [20] the scaling of the cutoff energy for protons from the front surface and normal incidence of the laser is

$$E_{MAX}^{front} \approx 2\sqrt{2}aZ \times 0.511 MeV \qquad \ldots\ldots\ldots\ldots 3.21$$

where a is the renormalized field amplitude.

For p-polarized light, independently from the scale gradient length [21], the heating mechanisms, resonant and vacuum heating, are directed along the normal, and so the accelerated ion beam. From [22] the front ion acceleration can be seen as a balance between the thermal pressure and the laser pressure:

$$\frac{dE_i}{dt} = (1+R)\frac{I_0}{cL_s} - \frac{n_e k_B T_e}{L_{grad}} \quad ……………….3.22$$

3.4.2 Rear surface acceleration

When a hot plasma is not confined, its internal pressure leads to its expansion. We observe the formation of a density gradient, density being lower at peripheral regions, and the propagation of a rarefaction wave towards the higher densities. The local charge neutrality holds up to its local Debye length (3.2). The difference in mass between electrons and ions produces a separation of charges at the plasma/vacuum interface; the suprathermal part of the electron spectrum enhances this separation, which results in an accelerating field that drags and accelerate the initially cold ions[23, 24].

The suprathermal electron population that is produced in the laser-plasma interaction drifts through the target. Upon its arrival onto the rear surface, the matter is ionized by resistive heating and collisions; the resistive heating happens as a consequence of the ultra strong currents that re-equilibrate the charge unbalance. The divergence of the electron flux travelling through the bulk is in some part considered responsible of the decrease of ion energy that is observed on thicker targets. In [25] the divergence is measured by looking at the Optical Transition Radiation (OTR) emission on the rear surface of targets of different thicknesses. The measured half width at half maximum (HWHM) corresponds to an angle of 17 (The experiment was held in the Laboratoire pour l'Utilisation des Lasers Intenses (LULI) of the ´E cole Polytechnique and the focusing parabola had f/3 aperture). More recent experiments [26] repeated the measure by observing the Coherent Transition Radiation (CTR) emission. They underlined a double structured transport, with a hotter and narrower bunch ($\approx$ 10MeV at ~ 7◦ HWHM), followed by a colder and more divergent ($\approx$ 600keV at ~ 35◦

HWHM). The second one contains the larger part (some tens of percent) of the total laser energy. In the following sections, two analytical models for TNSA ion acceleration are presented.

3.4.3 Isothermal Model

In [27] and in later improvement [28] is presented the solution for the expansion of an isothermal plasma where $T_e \neq T_i$. At t = 0, a semi-infinite plasma occupies the ($-\infty$, 0] space; ions are cold whereas an electronic temperature Te exists. No cold electrons are taken in account and the neutrality is written as $n_{e0} = Zn_{i0}$. The electron population respects the Boltzmann distribution.

$$n_e \frac{\partial^2 \Phi}{\partial x^2} = e(n_e - Zn_i) \dots\dots\dots\dots\dots 3.23 \text{ a}$$

Under the action of electrostatic potential Φ

$$\varepsilon_0 \frac{\partial^2 \Phi}{\partial x} = e(n_e - Zn_i) \quad \dots\dots\dots\dots\dots 3.23 \text{ b}$$

The electric field at x = 0 is obtained by integration of (3.23b), which produces [29]

$$E_{front,0} = \sqrt{\frac{2}{e}} \cdot \frac{k_B T_e}{e\lambda_{D0}} \quad \dots\dots\dots\dots 3.24$$

During the evolution in time the electron component is supposed in equilibrium with the potential, while the ion component is governed by the fluid equation where the force on the electron component derives from the potential Φ :

$$\frac{\partial u_i}{\partial t} + u_i \frac{\partial u_i}{\partial x} = \frac{Ze}{m_i} \frac{\partial \Phi}{\partial x} \quad \dots\dots\dots\dots 3.25$$

The set of differential equation of fluid equations and (3.31) with the conditions (3.23a) and (3.23b) has been resolved numerically with a lagrangian code in [27]. The formation of three non-neutral areas is observed (Fig.3.10). Firstly a rarefaction front with positive charge propagates at a speed $-cs$ in the unperturbed plasma. Secondly a

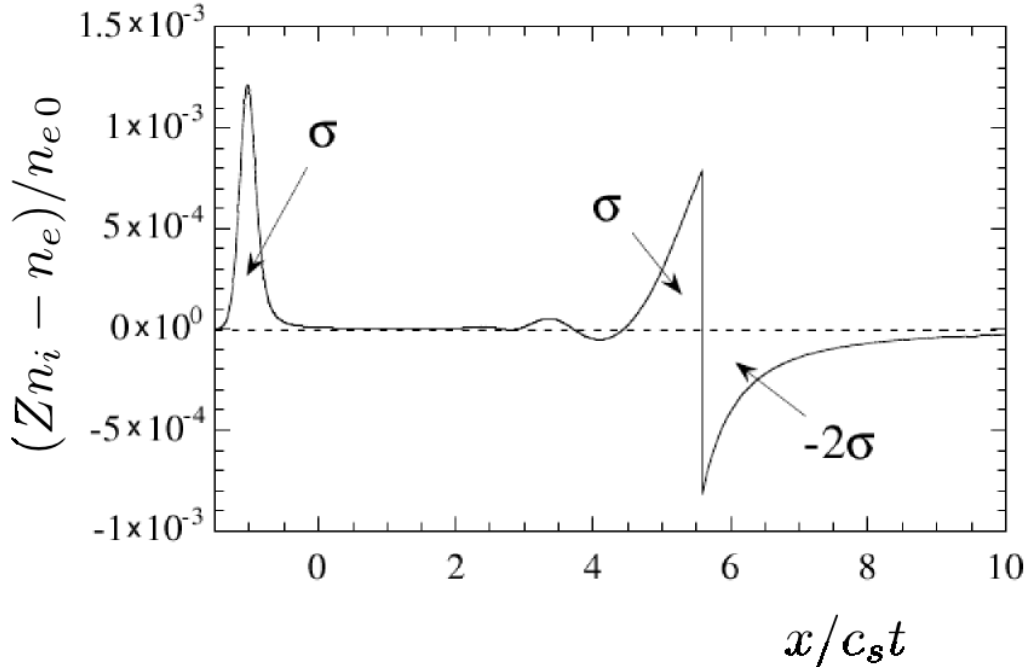separation of charges forms at the expanding front: an electron cloud followed by an ion front. By fitting the

Figure 3.10: The creation of three non-neutral areas during the expansion of the hot electrons, cold ions plasma (excerpt from [31]).

numerical result for the accelerating field at the charge separation front, it is obtained:

$$E_{front} = \frac{2E_0}{\sqrt{2e + (\omega_{pi}t)^2}} \quad \ldots\ldots\ldots\ldots 3.26$$

from which the speed of the ion front is:

$$v_{f,I} = 2c_s \log\left[\tau + \sqrt{\tau^2 + 1}\right] \ldots\ldots\ldots\ldots\ldots 3.27$$

$$\tau = \frac{1}{\sqrt{2e}}\,\omega_{pi}t \ldots\ldots\ldots\ldots\ldots\ldots\ldots 3.28$$

where $\omega_{pi} = (Zn_{e0}e^2/m_i\varepsilon_0)^{1/2}$. It has to be underlined that in this calculation the charge neutrality $n_i - n_{e0}/Z$ is fixed at the beginning of the simulation, which makes the quantity ω_{pi} dependent on the initial n_{e0}. The ion energy is finally calculated from 3.22 and 3.23a and 3.23b to be:

$$E_{max} = \frac{1}{2} Z k_B T_e [2\log(\omega_{pi}t) - \log(2) - 2]^2 \quad \dots\dots\dots\dots\dots 3.29$$

In the isothermal model, no energy depletion of the electron component is taken in account. The ions will indefinitely gain energy in time. Rough estimation of a meaningful "acceleration time" correlates with the duration of the laser pulse.

3.4.4 Adiabatic Model

The experimental situation of a laser-plasma acceleration on a thin target, differs from the assumption of isothermal model by the fact that (i) the finite size of the target doesn't provide an infinite reservoir of hot electrons and (ii) no external source of energy exists for an indefinite acceleration time. In [30], an improvement to the isothermal model is presented. At the initial time t = 0, the plasma at density (n_{i0}, n_{e0} = Zn_{i0}) occupies the space x $\in$ [−L/2,L/2] (Fig.3.11). The depletion in energy of the electron component is inserted in the calculation by
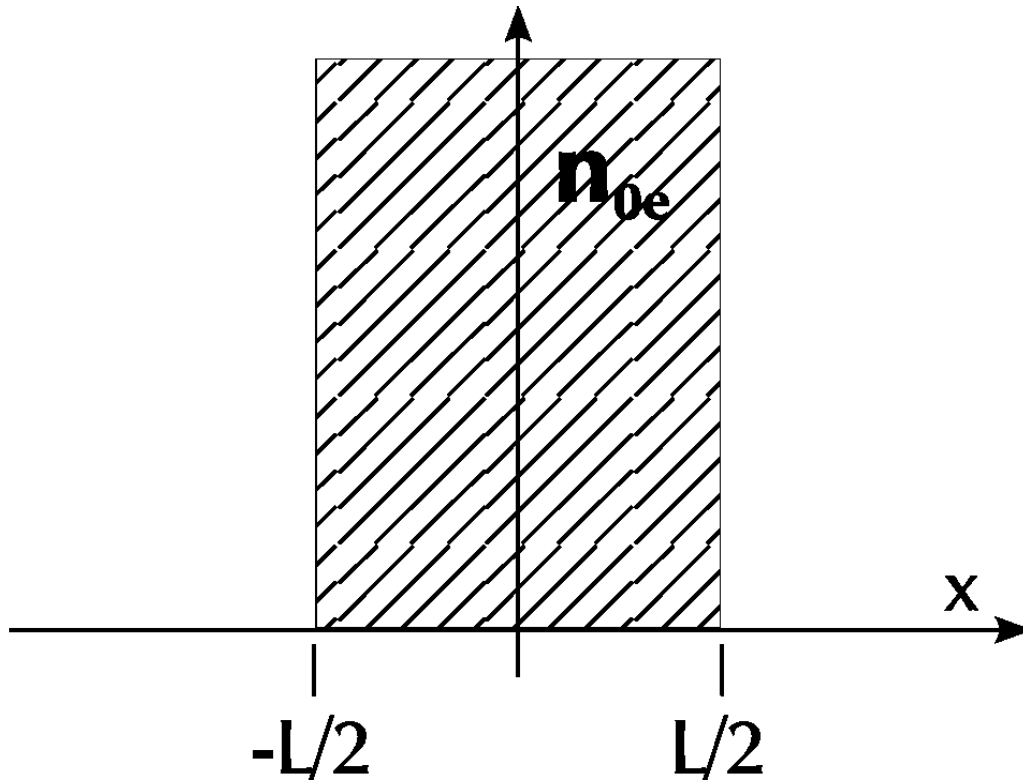
Figure 3.11: Initial condition for the adiabatic model.

$$\frac{dU_{elec}}{dt} = -\frac{dU_{ions}}{dt} - \frac{dU_{field}}{dt} \dots\dots\dots\dots\dots\dots \; 3.30$$

The expansion is symmetric in the two directions, which adds the condition E (x = 0)= 0 and v_e (x = 0) = 0 for every time. The system of equations from the isothermal model expressed by fluid equations and (3.25), (3.23a and 3.23b) is resolved by the same lagrangian code with the added condition (3.30). In these condition, the solution doesn't change from the isothermal model when $t < t_L$, defined

$$t_L = L/2c_{s0} \dots\dots\dots\dots\dots\dots\dots..3.31$$

the time needed to the rarefaction wave to reach the x = 0 boundary. The simulations show that for $t \ll t_L$ the electron temperature is constant, but that as t approaches t_L the temperature starts falling (Fig.3.12).
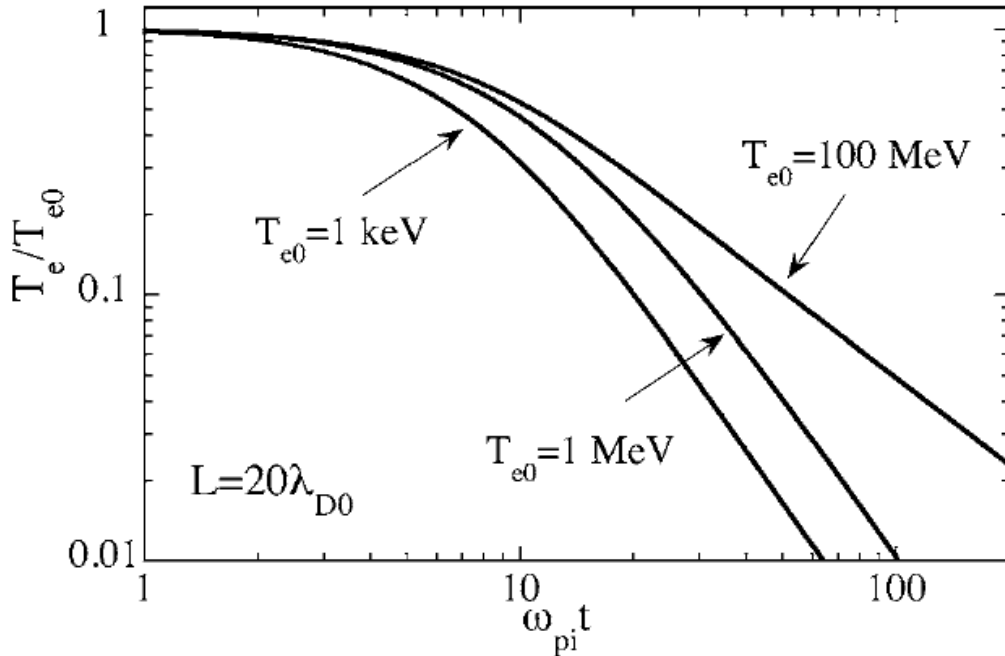
Figure 3.12: Electron temperature decreasing in the adiabatic expansion from a finite size plasma (excerpt from [58]). For an Aluminum target heated at $I = 4 \times 10^{19} W/cm^2$, $T_e \approx 1MeV$ which corresponds to $20\lambda_D \approx 0.4\mu m$. On the time scale, $\omega_{pi} \approx 40ps^{-1}$

The final ion velocity is found to be

$$\upsilon_{f,A} = 2c_{s0} \log[\alpha \frac{L}{\lambda_{D0}} + \beta] \ldots\ldots\ldots\ldots 3.32$$

where α and β are found to depend on the electron temperature. For Te = 1MeV it is found α = 0.49, β = 5.3. If we compare (3.32) to (3.27 and 3.28), the two asymptotic behaviours are found to be similar when $L \gg \lambda_{D0}$ with an acceleration time of t_L (3.31).

The applicability of each of the two models to the real experimental case of a thin metal foil heated by a laser is bound to the relationship between the two parameters tl, the laser duration, and te = 2_L/c, the time needed to relativistic electrons to fill the entire thickness 5. When $t_L \ll$ te the interaction between the electron burst and the non-irradiated surface happens only once, which can be considered as the case of an isothermal expansion limited to the duration of the laser pulse, tacc = t_l. For $t_e \simeq t_l$, the hot electrons fill the target, making the adiabatic model applicable. In [32] a correction to the model is presented, which analyses the expansion of a plasma slab when the ion-vacuum front is not steep anymore. A density gradient is introduced at t=0 on the ion front with the scale length of l_{ss} as sown in figure 3.13.
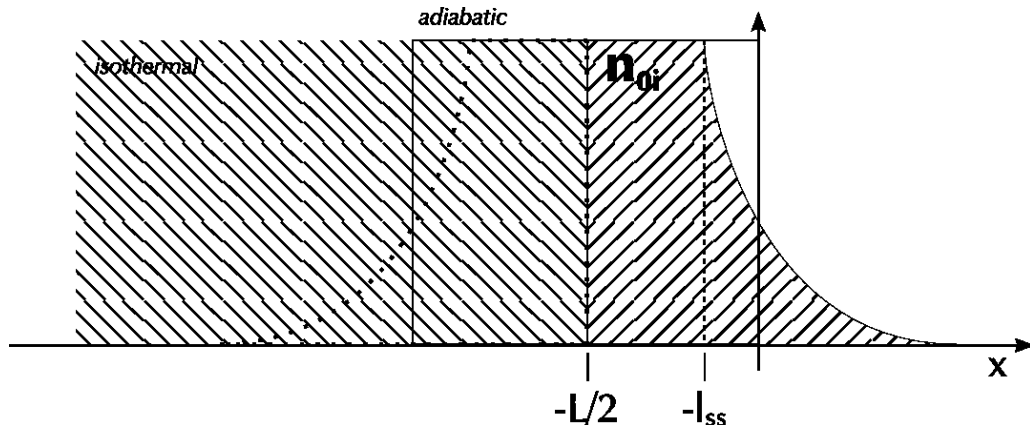

Figure 3.13: Picture of the initial condition for the two cases. In the isothermal case, the density is constant ni(x, t = 0) for x ∈ (−∞,−l_{ss}] and exponentially decreases on the right hand side of x = −l_{ss}. In the adiabatic case, the plasma initially occupies the x ∈ [−L, 0]; the symmetry axis is set at x = −L/2 and the two density gradients begin at x = −l_{ss} and x = l_{ss}− L.

The evolution of the system is analyzed for both the models (isothermal and adiabatic). According to the different representations of the initial system, the corrections are introduced as follow.

Isothermal The cold ion density distribution is

$$n_i(x, t = 0) = n_{i0} \qquad\qquad x \le -l_{ss} \ldots\ldots\ldots\ldots 3.33$$

$$n_i(x, t = 0) = n_{i0} . e^{-\frac{x + l_{ss}}{l_{ss}}} \qquad x > -l_{ss} \ldots\ldots\ldots\ldots 3.34$$

The density gradient starts at $x = -l_{ss}$ and the constant density plasma sits in the half-space for $x < -l_{ss}$.

Adiabatic The situation depicted in Fig.3.11 is modified in a way that the new symmetry axis is $x = -L/2$ which make the plasma slab to be initially between $-L$ and 0 for $l_{ss} \rightarrow 0$. The gradient envelope is the same as defined in (3.33 and 3.34) for $x > -L/2$ and is symmetrized accordingly for the left hand side.

Aside of this, the physical scenario is the same as previously described, i.e. the ions are initially cold and the electron temperature is set to T_{e0}. As the system is let evolve, by solving the set of fluid equations, the ions in the more peripheral region are accelerated by a charge separation field that is weaker than what experienced by those in the denser plasma. The differential gain in energy brings to the crossing between the two populations: the more internal and faster ions overrun the external and slower and the plasma fluid comes to a wave breaking.
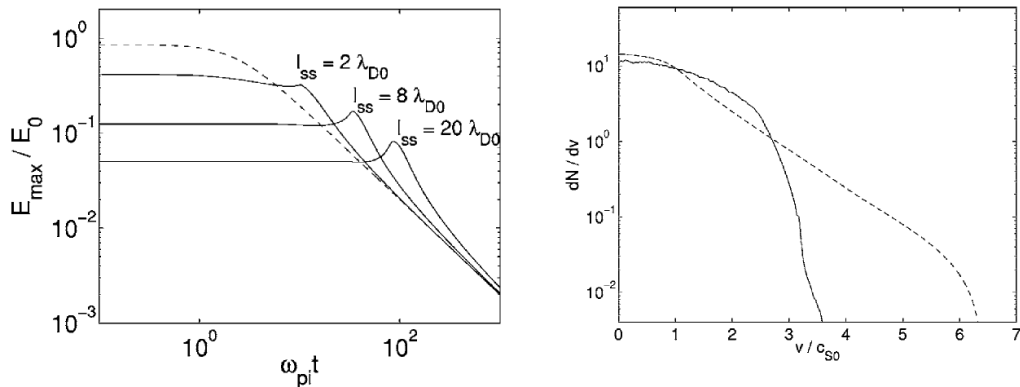

Figure 3.14: (left) The evolution in time of the accelerating field due to charge separation at the plasma boundary for different initial density gradient lengths. The dashed line represents the ideal ($l_{ss} = 0$) case for comparison; the peaks in the plot mark the moment when the breaking of the wave happens. (right) Final ion velocity spectrum for a sharp boundary (dashed) and lss = $20\lambda_{D0}$ (solid) from an adiabatic simulation of L = $40\lambda_{D0}$.

The evolution in time of the accelerating field for fast ions is shown in Fig.3.14-left for different initial conditions. After an initial, constant, accelerating field, a peak appears at the moment the wave breaks; the asymptotic behaviour is found to be the same in all the cases. The accelerating field before the wave breaks is lower for longer plasma scale lengths. A simulation on the adiabatic case, see Fig.3.14-right, clearly shows that the final energy that is acquired from a steep boundary plasma is lower than what is achieved in presence of a gradient. Moreover, longer the gradient, lower is the final ion velocity.

Chapter 4: Description of the used laser facilities for the Experimental work

4.1 The laser source, LOA (Laboratoire d'Optique Appliqu´ee)

The Salle Jaune laser is a Titanium-Sapphire (Ti:Sa) solid state laser and belongs to the category of T^3 lasers (Table Top Terawatt). It is a multi-stage CPA chain composed by a pre-amplified front-end and three multipass amplifiers, capable of delivering up to 2J per pulse (before compression) at a repetition rate of 10Hz.
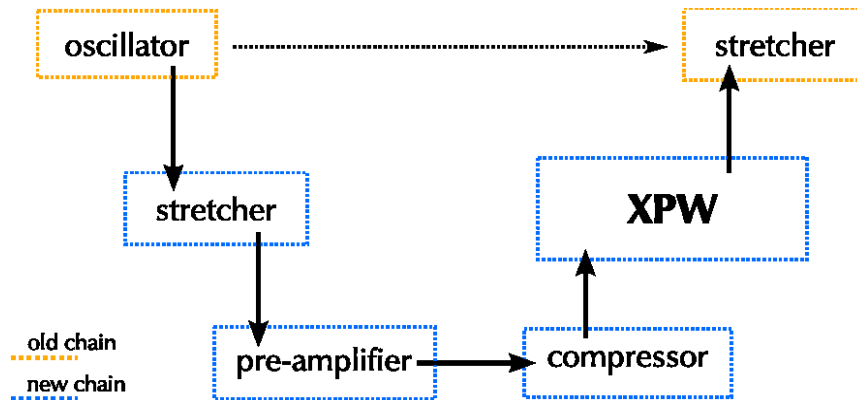
Oscillator:

A Ti:Sapphire, Kerr-lens mode-locked, oscillator produces a train of 8.5fs pulses, with a per-pulse energy of 5nJ at a repetition rate of 88MHz. The central wavelength is $\lambda = 810$nm and the spectrum is 150nm FWHM1.

Pre-amplification and XPW:

The repetition frequency from the oscillator is cut down to 10Hz by Pockels cells. The selected pulse is stretched, pre-amplified to 1mJ and compressed back to 23fs, in order to be injected in the XPW system. The preamplifier is charged by a diode-pumped CW laser, which noticeably improves the stability.

Multipass amplification:

The pulse is stretched to 600ps and injected in a three stages (4-pass, 5-pass and 3-pass) chain of Ti:Sa amplifiers pumped by doubled Nd:YAG lasers. The beam undergoes spatial filtering after each amplifier. The complete amplification process brings 100nJ (after XPW) to ≈ 2J. The contrast worsen from 10^{12} to $10^{9} \div 10^{10}$.

Separation of the beams:

Before the compression, a partially reflecting mirror (in our experiment was 10%) is used to create a second beam (probe) with lower energy. A $\lambda/2$ filter and a polarizer cube are used to introduce a variable loss. Finally, a motorized delay line is provided to change the delay between the two beams.

Compression:

The two beams of 400ps pulses are compressed by two separate grating compressors to a duration of approximately 30fs with an efficiency that ranges between 45% and $\approx$ 55%.Phase front cleaning: the wave front of the pump beam is corrected by a cylindrical symmetry deformable mirror.

Enhancement of the Contrast

The contrast ratio of an UHI pulse is a parameter of great importance when speaking of interaction with matter. Many features, many of them not completely exploited, of the interaction process are correlated with the total energy and the over-threshold duration of the pedestal that precedes the main peak. From a CPA chain, three types of effects are in general observed.

Prepulses

Replica of the fs pulse can be produced, by various reasons, before and after the main pulse. Examples are (i) insufficient extinction power of the Pockels cell that selects the pulse from the oscillator, (ii) the presence of shortcuts in the optical path or (iii) cuts in the pulse spectrum. Background light In the oscillator cavity, the production of fs pulses (with a repetition rate of 88MHz and a per-pulse energy of some nJ) is a process which is in competition with the continuous wave (CW) production, which results in a continuous background around the fs pulses. The contrast in the oscillator pulse train can however be as high as 10^9.

Amplified Spontaneous Emission

The ASE comes from the spontaneous emission in charged crystals, which is produced before the passage of the main pulse. The ASE is amplified in the forthcoming crystals, worsening the contrast. The importance of the spontaneous emission is directly bound to the gain in the amplifiers and to the timing between the pump laser pulses (used to charge the mediums) and the seed laser pulse (to be amplified).The path of the pulse in the optical system controlled by optical shutters (Pockels cells).

Their synchrony to the pulse sets the mark on the prepulse structure, cutting the sum of the three effects to a well defined light front. In Salle Jaune, the Pockels cells cut the pedestal between 2.5ns and 3ns before the fs pulse. In the original chain, before any active contrast enhancement technique was adopted, the peak to pedestal ratio was, $I_{max}/I_{ASE} = 10^7$ from 3ns before, and $I_{max}/I_{pre-p} = 10^5$ for prepulses 100ps before.

Cross polarized wave generation (XPW)

The use of XPW (acronym for Crossed Polarized Wave generation) to improve the contrast in a laser chain has been introduced at the Laboratoire d'Optique Appliqu´ee after previous studies on the $\chi(3)$ anisotropy of BaF^2 glasses. The generation of a crossed-polarized wave is a degenerate, $\omega \to \omega$, four wave mixing process, where a rotation of the polarization is produced between the input and the output wave.

The enhancement of contrast relies on the fact that the III-order non-linear process holds a 3rd order dependency of the output field on the input field. This produces a rotation of the polarization which depends on the 3rd power of the incoming intensity. The effect is optimized by matching the thickness of the BaF^2 crystals with the input amplitude A0, two polarizers in the final setup are used to (i) set the input polarization, (ii) select the output. a contrast of 10^{12} is reported, from 3ω autocorrelation measurements on the Salle Jaune front-end.

The theoretical efficiency in terms of contrast enhancement is limited by the extinction power of the two polarizers (the polarizer before and the analyzer after) that are used to set the input polarization and select the cross-polarized output. The low generation efficiency (12% and 25% respectively for single or double crystal arrangement) and the necessity to work on the compressed pulse made necessary to pre-amplify the pulse (and compress it back) before entering the system

Laser Diagnostics

Energy

The laser in its present conditions produces 1.5J to 2J per pulse before compression. The optics chain from the source to the experimental installation transports a total of 37% (measured) in energy. The efficiency of the compressor alone accounts for ≈ 45% of losses, which leaves ≈ 3% loss for each mirror. At the end of the experiment

the total transport coefficient decreased to 30%, probably due to aluminium deposition on the mirrors.

Focusing

The main beam is focused by a glass parabolic reflector; the parabola is a 30◦ off-axis cut, with a numerical aperture of f/3 and a focal length of 15cm. The glass surface is gold coated to optimize the reflectivity. In the case of an ideal gaussian beam, the pump would be focused down to a waist of w0 = 1.4μm.To image the focal spot, the focused beam is intercepted by a removable mirror and sent through a microscope objective to a linearized camera. The quality of the spot is defined by measuring its transverse size and the ratio of energy contained in its $1/e^2$ contour

Monitoring of Laser Parameters

In a laser system of this size it is common to observe fluctuations in the functional parameters. A precise control of shot to shot behaviour is even more important in experiments where a single measurement cannot be repeated a number of times sufficiently high to authorize a statistical treatment. Nevertheless a strong correlation between the different parameters (energy, direction of the beam, contrast, etc.) is observed; this enables us to limit our observation of the laser status to some key parameters and be able to set a rejection criterion out of them. During the experimental procedures, two diagnostics constantly keep the laser status under control: the pulse integrated energy and the contrast ratio. The energy is integrated by a linearized camera: the small leak (< 0.01% of energy) from a dielectric mirror is enough to record the transverse profile of the beam and to observe the variation in energy.

Two effects have been noticed in time: (i) a strong shot to shot and (ii) a slow drift on the average energy. To measure the contrast of the pulse, an aluminium-coated glass blade is used to intercept a tiny part (smaller than $5mm^2$) of the main beam. The reflection is sent to a fast photocathode (rise time < 500ps) that is controlled by a fast oscilloscope. A number of neutral optical densities, enough to observe the peak of the femtosecond pulse is added. Once the reference is taken, all of the densities are removed and the pedestal observed. The contrast is calculated from the ratio between the peak and the pedestal, taking in account the number of densities and the

integration factor of the photocathode (500ps/30fs = 1.6×10^4). The insertion of the blade did not produce any measurable worsening of the focal spot.

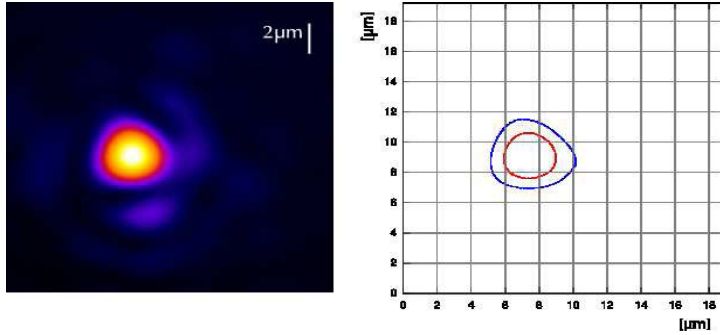Figure: Laser focal spot at 800nm; (a) image of the spot as seen by camera (resolution: 0.040μm/pix, magnification: 230×); (b) contour plots of two different levels of intensity; in red the FWHM contour (diameters: vertical 2.92μm, horizontal 3μm); blue is $1/e^2$ (diameters: vertical 4.4μm, horizontal 5μm) which corresponds to an average waist of 2.35μm. In the depicted case, a total of 72% of the energy is contained in the $\pi\omega_0^2$ surface.

4.2 The Lund multi-TW femtosecond laser, LLC(LUND LASER CENTRE)

The multi-terawatt laser at the Lund Laser Centre in Sweden is Ti:Sapphire based and operates at 10 Hz with a central wavelength of 800 nm and delivers pulses of 35 fs duration. A synchronised longer pulse beam is also available for experiments. The 5 nJ seed pulse for the main CPA beam line is generated by a Kerr-lens modelocked oscillator. These pulses are amplified via a multi-pass configuration and then passed through a saturable absorber (10% transmission) which removes or reduces the energy contained in any pre-pulses or amplified spontaneous emission (ASE). The pulses are then stretched to ~ 300 ps, using a grating based stretcher. One of the pulses, energy > 10 nJ, is then singled out and passed through a three stage amplification line. The first stage is a regenerative amplifier and the other two stages are both multi-pass amplifiers, the second one being cryogenically cooled. The beam is then expanded to a diameter of 50 mm and sent through a grating compressor under vacuum to get the

final main pulse. Between the last two amplification stages a VSF is used to improve the beam profile. The amplifiers are pumped with frequency doubled Q-switched Nd:YAG lasers with a total pump energy of ~7 J at $\lambda = 532$ nm. The second beam line can be used to deliver either a relatively short or a long pulse. The short pulse is sourced from the main pulse before the last pass in the final amplifier, with a maximum energy of ~ 500 mJ, and is either left uncompressed (300 ps) or compressed in a separate compressor in air to sub 100 fs duration. The longer pulse (nanoseconds) is sourced from one of the pump lasers, Q-switched Nd:YAG, where a fraction of the energy (50 mJ) is sent to the target chamber.
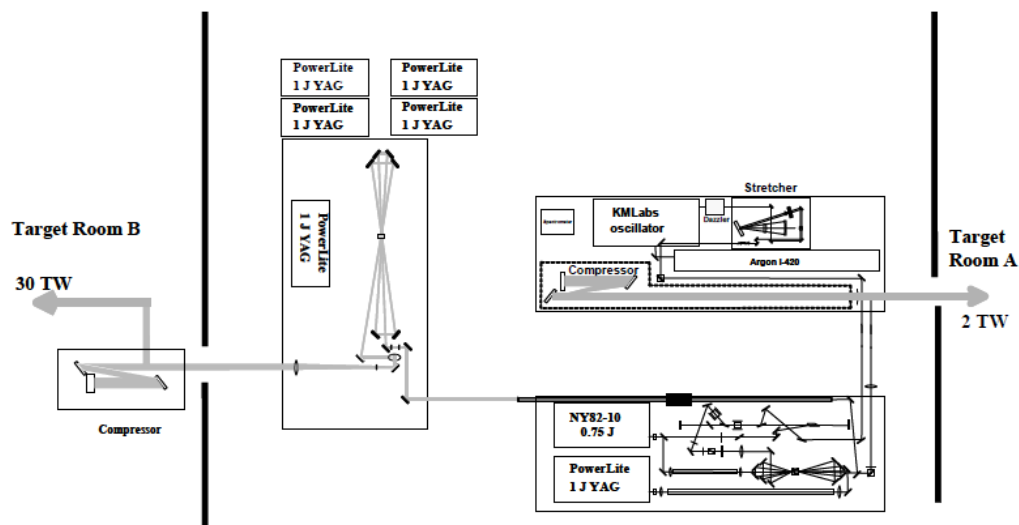
Figure: A schematic overview of the Lund multi-TW laser system.

4.3 The Vulcan laser, RAL (Rutherford Appleton Laboratory)

The Vulcan laser is an Nd:glass laser consisting of 8 beam lines and can deliver different configurations of these beams into three target areas: Target Area East (TAE), Target Area West (TAW) and Target Area Petawatt (TAP). In TAE the main interaction beams are long pulse beams with a minimum pulse length of 80 ps and hundreds of joules of energy. Configurations which utilise all 8 beam lines can be employed. TAW and TAP are the two short-pulse high-intensity laser areas and were both used during various experiments, and are discussed in more detail. Fig. shows the layout of Vulcan and the three target areas.
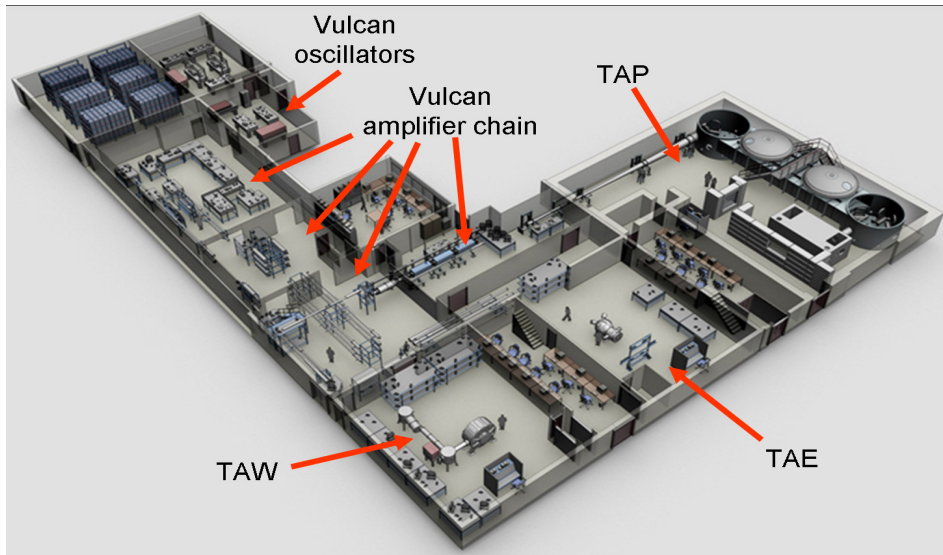
The layout of the Vulcan laser and the three target areas

In TAW it is possibe to use 6 of the 8 beams as nanosecond long pulse beams, delivering up to 200 J each. There is a high degree of flexibility for the beam path layout going into the target chamber. One of the other two beams is used as the main interaction beam and is able to deliver, via chirped pulse amplification (CPA)., 100 J onto target in a 1 ps pulse duration. The eighth beam is typically used as an optical probe diagnostic and has a minimum pulse length of 10 ps, produced by CPA pulse compression in air. This beam line has recently been upgraded to deliver 500 J in 10 ps. The central wavelength, $\lambda = 1053$ nm, is the same for all beams going into the area. TAP is configured to use two beam lines; one is an ultra-high intensity (gives 500J in 500 fs which means) 1 PW (10^{15} W) beam (that gives the target area it's name) and the second beam is a nanosecond long pulse beam (one of the Vulcan main six nanosecond beams). The petawatt beam is able to deliver 500 J in 500 fs through the use of optical parametric chirped pulse amplification (OPCPA). On the 5th October 2004 the petawatt laser achieved a Guinness World Record by delivering 1.03 PW (423 J in 410 fs) and achieved an intensity of 1.06×10^{21} Wcm^{-2}. In 2007 the TAP area was upgraded to make it possible to deliver one of the 6 nanosecond long pulse beams into the area, with a maximum deliverable energy of 200 J. The central wavelength for the Petawatt beam is slightly longer at $\lambda = 1054$ nm, due to a different amplifier configuration. For each target area in Vulcan there is a separate short-pulse oscillator, with each oscillator utilising a different method of mode locking to produce the ultra-short seed pulses needed for both CPA and OPCPA.

Group photo at RAL in TAW(Target area west) during the Hiper experiment Oct-Dec 2008

TAW oscillator

The laser source for the TAW beam line is a Semiconductor Saturable Absorber Mirror (SESAM) oscillator with the active medium being Nd:glass. The reflectivity of the saturable absorber mirror is dependent on the incident laser intensity. At low intensities, such as continuous wave (CW), the laser light is absorbed by the SESAM. At higher intensities the absorber becomes saturated with laser light and becomes reflective allowing random high-intensity short-pulses of light to be reflected. These short-pulses are amplified further after each pass through the laser cavity. A part of each pulse is transmitted at one end of the cavity by an output coupler resulting in a usable seed pulse. The SESAM oscillator produces 1 nJ pulses with a duration of 120 fs from an 80 MHz cavity.

TAP oscillator

A Ti:sapphire Kerr Lens Modelocked (KLM) oscillator is used as the source seed pulse for the Petawatt laser. This oscillator utilises a passive mode-locking method based on the non-linear Kerr effect in the laser medium. The effective refractive index (η) within the laser medium is dependent on the laser intensity I and its effect on the non-linear refractive index component

($\eta_2 I$):

$$\eta = \eta_0 + \eta_2 I$$

Because the beam has a non-uniform intensity distribution, with higher intensity on-axis than in the wings, the Kerr effect leads to self-focusing of the beam. Using an aperture in the laser axis, inside the laser cavity, makes it possible to discriminate in favour of high-intensity pulses that can be amplified further. This oscillator produces seed pulses of 5 nJ with a pulse length of 120 fs at a frequency of 80 MHz and has a bandwidth of 15 nm centred at 1053 nm.

Chirped Pulse Amplification, CPA – TAW

To achieve ultra-high intensities in TAW, CPA is used. The maximum energy that can be delivered by a laser system is limited by the damage threshold of its optical components, specifically the amplifier crystals. To prevent damage to the amplifier crystals without using CPA means expanding the area of the laser beam, resulting in the need for larger optics which becomes prohibitively expensive. CPA gets around this by lengthening the pulse for amplification and transport to the target areas. The pulse is then re-compressed, with a minimum number of reflective optics before reaching target, to get a high power pulse. The seed pulse is stretched using a double pass refractive confocal telescopic stretcher which disperses the frequency components of the pulse over different optical path lengths using a pair of diffraction gratings. The result is a chirped pulse with a frequency that varies linearly with a total pulse length of ~ 100 ps. This pulse can then be safely amplified through a series of Nd:glass rod and disc amplifiers. The beam first passes through the rod amplifiers with gradually increasing beam diameter of 9 mm, 16 mm, 25 mm and 45 mm. The final amplification is then carried out with a pair of disc amplifiers with diameters of 108 mm and 150 mm. At various stages along the beam line the laser is focused through a vacuum spatial filter (VSF, aperture in vacuum) which removes any part of the beam that does not have the correct divergence. The final stage of CPA is re-compressing the pulse with another pair of diffraction gratings that are a similar match to the first pair, but scaled up in size and with slight differences in alignment to account for aberrations in the system. The final result is a 1 ps pulse with an energy onto target of ~100 J, generated from a 170 fs, 1 nJ pulse. The limiting factor for the maximum deliverable energy is the coatings on the gratings rather than the amplifiers. Within the target chamber the pulse is focussed using an off-axis parabola with an

effective f/4 achieving FWHM (Full Width Half Maximum) focal spots of 9 µm. This gives peak intensities of ~7 x 10^{19} Wcm^{-2}, assuming half the laser energy is contained in the central spot.

Optical Parametric CPA (OPCPA) – TAP

Conventional amplification in Nd:glass is typically affected by gain-narrowing which limits the pulse bandwidth and so limiting the shortest pulse length achievable. To avoid this restriction the Vulcan Petawatt beam line uses OPCPA to increase the frequency bandwidth during a pre-amplification stage and therefore reducing the minimum pulse length possible for the system.

The seed pulse is first stretched, by a four-pass Offner stretcher, to 2.4 ns and is then sent through the optical parametric amplifier (OPA). The OPA works by mixing the seed pulse with a frequency doubled, 200 - 300 mJ, 4.5 ns pump pulse generated by an Nd:YAG laser. The system is designed so that the maximum bandwidth transmitted through the system is 18 nm which is a factor of 4.5 greater than the minimum required for a 500 fs pulse. The amplification mixing of the pump and seed pulses occurs in β-Barium Borate, a non-linear medium, with a total gain greater than 10^7. The amplification occurs over three single pass stages which ensures a low level of amplified spontaneous emission. The pulse is then passed through the stretcher for a second time to stretch the pulse to 4.8 ns. The main amplification stage for the Petawatt beam uses a combination of Nd:silicate and Nd:phosphate amplifiers. The mixed glass is used to reduce the effect of bandwidth narrowing and results in a central laser wavelength of λ= 1054.5 nm. The pulse is first passed through 9 mm and 16 mm Nd:silicate rod amplifiers to deliver an initial high gain. The pulse is then passed through the amplifiers of the main Vulcan short-pulse beam line with the 25 mm and 45 mm Nd:phosphate rod amplifiers and the 108 mm and 150 mm disc amplifiers. A mirror that slides in re-directs the beam through three more disc amplifiers with diameters equal to 208 mm. After this final stage the pulse energy is ~ 650 J, before entering the target area where it is re-compressed. Wave front errors that are introduced into the beam during propagation through the optical chain are corrected for by an adaptive optics (AO) system. This consists of a 120 mm deformable mirror, positioned after the rod amplifiers, but before the disc amplifiers, that adapts to slowly varying aberrations using a feedback loop mechanism based on

wave front measurements made at the end of the amplification chain. Correcting the wave front errors enables improved pulse compression and final focusing onto target. During the experiment conducted on TAP, the Nd:silicate section of the Petawatt beam line suffered from problems which meant that only Nd:phosphate amplifiers were used. This increased the typical pulse length from 500 to 600fs to ~1ps, the maximum energy available was similar through driving the Nd:phosphate amplifiers harder to achieve greater gain. Inside TAP the amplified pulse is compressed under vacuum to 500 fs by a pair of 1480 lines/mm gratings with an energy transmission efficiency of ~ 60%.The diameter of the gratings is 940 mm, which enables the beam to be expanded to a large diameter so that the energy per area is below the damage threshold of the gratings. The beam is then passed into the target chamber with a final diameter of 600 mm and is focused onto target with an f/3 off-axis parabola. The spot size of the focused beam at FWHM is ~ 5 µm which gives a peak intensity of ~ 2 x 10^{21} Wcm^{-2}.

Chapter 5:

Uniform Distribution and enhancement of Laser Driven ion/proton beam Energies

5.1 Introduction

The ion beams generated at the rear surface of a thin foil irradiated by a ultrahigh intensity ($> 10^{19}$ Wcm^{-2}) laser pulse has attracted a great deal of research interest. The distinctive characteristics of these beams, such as high laser-to-particle energy conversion efficiency [33], very low emittance [34] and a small virtual source size [35], make them attractive as an ion source. Some of the applications that have been proposed for these ion beams are discussed in chapter 2, including radiotherapy, medical isotope production and radiography. A detailed experiment and results will be reported on Proton Radiography in [chap 6] . To succeed in using laser driven ion beams for such applications requires that the parameters of the ion beam, such as ion energy spectrum and beam collimation, need to be carefully controlled and tailored. It has been demonstrated through the use of carefully structured target foils that the ion beam parameters can be changed; for example beam focusing [36], collimation [37] and altering the energy spectrum to a quasi-monoenergetic distribution [38,39]. However the reliance on complex targets is not always compatible with the requirement of high repetition rate ion beam delivery for many applications. Optical control of ion beam parameters, using simple planar target foils, and one or more laser pulses (operating at high repetition rate) is desirable. Results from several experimental campaigns aimed at the investigation of the use of dual laser pulses to influence and manipulate the ion acceleration processes in relativistic laser-foil interactions are presented.

Optimization of the high-energy end of the spectrum is a crucial point for the development of applications in various areas, e.g. for dense plasma radiography. Enhancement of laser-to-protons conversion efficiency and reduction of divergence are also equally important. Experiments have been in progress for about one decade to enhance proton energy beyond 60 MeV using the following strategies.

1-   Use of low-density plasmas
2-   Geometrical electron confinement
3-   Decrease the target thickness (less-spread+ volumetric target heating)

4- Highest Laser focussing

5.2 Source Characterisation

The first measurements of highly collimated multi-MeV proton [40-43] and ion [44] beams produced from thin foil targets irradiated by ultrashort high intensity laser pulses were published in 2000. The proton and ion beams observed had an exponential energy spectrum, with a maximum 30° to 40° half-angle beam divergence which decreases with increasing energy. To date, the maximum cutoff energy observed for protons is 58 MeV [41].

The laser intensities used to investigate ion acceleration range from ~10^{17} [45,46] to ~10^{21} Wcm^{-2} [33]. Ion acceleration as a function of a wide range of target foil parameters has been investigated. The target thickness has ranged from the ultrathin, tens of nanometres [47,48], through to microns [42,49] and hundreds of microns thickness [41,43,50,46,51,52]. Both insulating (plastic) and conducting (metallic) targets [41,43,46,53,54,55], as well as targets made up of layers of different materials [42,50,46,52,55,38] have been used to generate ion beams. Laser-driven ion acceleration has also been investigated with metallic wire targets [56,57], liquid droplets [58,59] and gas targets [60]. The highest quality proton beams are obtained with thin metallic foil targets.

The minimum foil target thickness that can be used for any given laser system is dependent on the laser contrast [61]. Ablative shocks induced within the target by the ASE pedestal or pre-pulses will reach the rear surface of the target, given enough time before the main pulse, and cause the rear surface to expand [62-64]. The expansion of the surface can be detrimental to the ion acceleration process [47,61].In this chapter, the effects of controlled expansion of the rear surface on ion acceleration is investigated. A variety of diagnostics have been used in experiments to measure the accelerated ions energy spectra and spatial distribution including RCF stacks [65,66], nuclear activation [67,68], CR39 nuclear particle detector [69] and Thomson parabola spectrometers [70].

There are several routes for beam optimization of laser-accelerated protons

- Use of low-density plasmas

high-energy ions, potential for high rep. rate if jet BUT sharp gradient needed.

- Use of ultra-thin targets

 high-energy ions, high-efficiency BUT requires high contrast.

- Use of small targets

high-energy ions, high-efficiency and collimation BUT requires high contrast.

- Use of tight focus

high-energy ions, high-efficiency AND provides high contrast.

5.3 Active Control on Proton Beam manipolation

During the first set of experimental compaigns at TAP (Target area petawatt at RAL) in July-August 2007, in which a separate study is done using a low intensity laser pulse to drive a low temperature shock wave to modify the rear surface of the target foil, and hence modify the properties of the ion beam. Besides using a separate low intensity pulse before the arrival of main interaction pulse the tailoring of Laser beam and Targets were also tried. Binary Phase plates and annular rings were used to Tailor the Laser beam and on the other hand different geometries of targets are also used .

5.3.1 Proton beam optimisation and spatial distribution.

- • The objective for this work is to use controlled and well-characterised front surface pre-plasma expansion to enhance ion acceleration. The effects on proton emission of a low intensity laser pulse (10^{12}Wcm^{-2}) irradiating thin foil targets prior to the main laser pulse ($> 10^{19}$ Wcm^{-2}) are presented. The first set of results from a detailed investigation using the Petawatt arm reported in Laser and Particle Beams 26 (2008) 591-596, in Comptes rendus. Physique. 10, no. 2, (2009): 188, Radiation defects and effects in Solids, accepted (2009), submitted in Nuclear instruments and methods (2009).

5.3.2 Experimental method

As this section covers the combined results from two experiments, the general experimental set-up that is similar to both is described first and then pertinent details for each experiment are highlighted. The experimental schematic is shown in Fig. 5.1 with features particular to each experiment identified. Both experiments use an off-axis f=3 parabolic mirror to focus the main laser pulse, duration 1 ps (FWHM) and p-polarised, to relativistic intensities. The focusing beam from the parabola is

intercepted by a plasma mirror, at a position such that the intensity is in the range 10^{14}- 10^{15} Wcm^{-2}, and is reflected onto a foil target. The plasma mirror is used to enhance the contrast of the laser on target by suppressing the ASE (Amplified Spontaneous Emission) pedestal to $\sim 10^{11}$ Wcm^{-2}. Prior to the arrival of the main pulse at the target, a lower intensity laser pulse (3 x10^{11} to 5 x10^{12} Wcm^{-2}), focussed by the use of an f/10 lens, irradiates the front surface of the target. The wavelength and duration (FWHM) of this lower intensity pulse is 1053 nm and 6 ns respectively, with a temporal profile that has a fast rise time of 0.2 ns and a slow decay from peak intensity to $\sim$ 50% of this level at 6 ns. For the Vulcan TAW experiment the main laser pulse has a wavelength of 1053 nm and energies up to 90 J after compression. The main pulse has an incidence angle of 15° onto the plasma mirror, with a measured reflectivity of 55%, giving energies on target of up to 50 J. The incidence angle of the beam onto target is 5° and the spot size at focus is 9 µm (FWHM), giving a peak intensity of 4×10^{19} Wcm^{-2}. The planar foil targets are 5, 12.5 and 20 µm thick Cu with a measured average peak-to-mean surface roughness of $\sim$ 0.7 µm. The leading edge of the low energy (< 5 J) lower intensity laser pulse arrives at the target 3.5-0.2 ns before the main laser pulse with an incidence angle of 25°. The intensity distribution at focus of this lower intensity pulse is shaped using a binary phase plate positioned in the beam just after the focusing lens. The intensity distribution shape is an annular ring, with a mean diameter of 460 µm and a `thickness' of $\sim$ 35 µm. The phase plate is a borosilicate glass substrate on which a surface relief, via photolithography, has been produced. This surface relief induces a design phase distribution in the laser beam which leads to the desired intensity distribution at focus. The intensity around the ring varies within the range 3×10^{11} - 3×10^{12} Wcm^{-2} and is shown in Fig. 5.2(a). The main laser pulse focal spot is positioned at the centre of this ring. For the Vulcan TAP experiment the main laser pulse wavelength is 1054 nm and is incident onto the plasma mirror at 20° with a measured reflectivity of 32%, resulting in a maximum energy on target of 115 J. The angle of incidence onto target is 10° and the spot size at focus is 5 µm (FWHM), giving a peak intensity of 3×10^{20} Wcm^{-2}. The targets are 25 µm thick Cu planar foils or 25 µm thick Au foils with a periodic groove structure on the rear surface. These grooves have a period of 10 µm and a sinusoidal profile with a peak-to-valley depth of 1.1 µm.
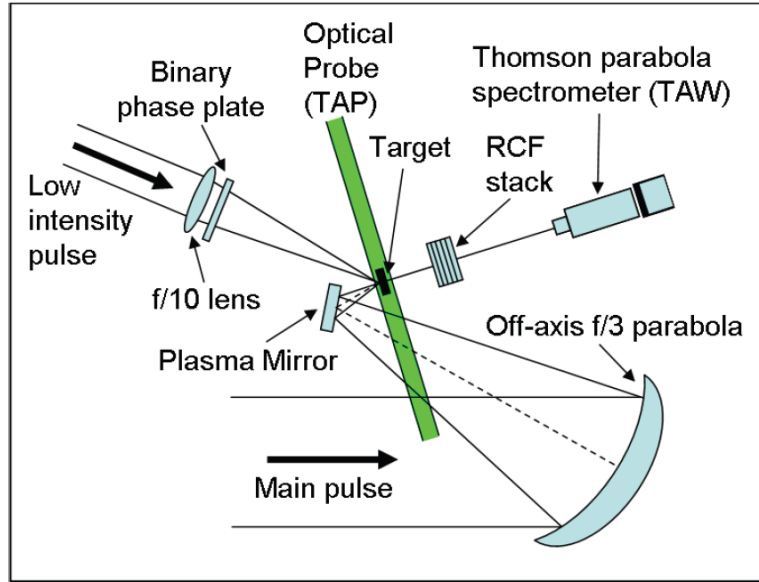
Figure5.1: Schematic of the experimental set-up for the TAW or TAP experiment. The primary diagnostic is the RCF stack and is common to both. Features of the set-up particular to one experiment are labelled either TAW or TAP to signify that experiment.

Fig. 5.3 shows images of the structure taken with an interference microscope. The low intensity laser pulse is focused to an approximately flat-top intensity distribution of
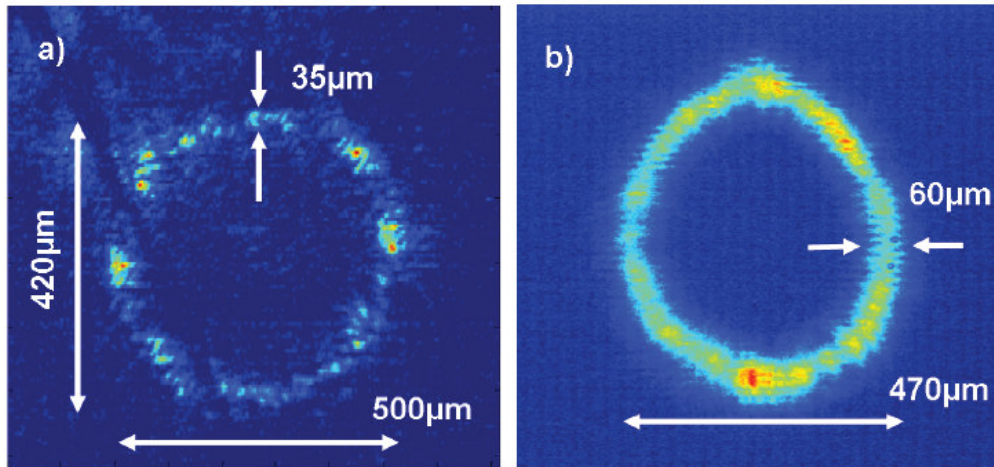

Figure 5.2: (a) The intensity distribution at focus for the low intensity laser pulsewith the binary phase plate in the beam path that results in an annular ring at focus. (b) The intensity distribution at target of the defocused low intensity laser pulse with an inverted aperture in the beam path. The images are captured with a CCD camera looking at focus with the laser in CW (continuous wave) mode.

450 μm diameter defocused spot (no phase plate used). This is positioned on target such that the focal spot of the main laser pulse is at the centre of the defocused spot.

The pulse energy is varied to change the intensity of the defocused spot in the range of 5×10^{11} to 5×10^{12} Wcm^{-2}. The low intensity pulse arrives on target prior to the main laser pulse with the time difference between the two main pulses varied from 0.5 ns to 3.6 ns with a precision of 0.2 ns. To confirm that the observations seen in the TAW experiment could be reproduced in TAP, for several laser shots the low intensity laser pulse is shaped into the annular distribution. This is done using either the same binary phase plate described above, or an inverted aperture inserted in the laser beam to produce a ring in the quasi-near field distribution (see Fig. 5.2). The main proton diagnostic for both experiments is an RCF stack placed behind the target and aligned along the target normal axis. Due to the higher proton energies produced on TAP, compared with TAW, the RCF layers are interspersed with Cu layers to provide additional energy filtering. The distance between the stack and target for TAW is 30 ± 1 mm and for TAP it is 39 ± 1 mm. In the TAW experiment a Thomson parabola spectrometer is positioned along the rear target normal axis to measure the ion species accelerated. The TAP experiment uses a transverse interferometric optical probe, wavelength 527 nm, to observe and characterise the front surface plasma expansion. The target is probed either 5 ps after the arrival of the main laser pulse or 50 ps before and is recorded using a 16 bit CCD camera. The resultant images have a spatial resolution of 5 µm.

5.3.3 Results

Effects of front surface plasma expansion on proton acceleration.

The proton beams generated by laser-foil interactions without the presence of the low intensity laser pre-pulse typically have uneven and asymmetric flux distributions across the beam, as measured with RCF. This is particularly true of low and medium Z targets. This asymmetry is most noticeable with the higher energy protons in the beam. Fig. 5.3(a) shows an example of the beam profile measured with RCF for the TAW experiment, for a 5 µm Cu target irradiated with a main laser pulse intensity of 2.5×10^{19} Wcm^{-2} and no low intensity pulse. When the target is irradiated with a low intensity pulse (3.5 ns prior to the main pulse) the profile of the resultant accelerated proton beam changes, as is shown in Fig. 5.3(b). The proton beam becomes more circular and has a more uniform flux distribution at all detected proton energies. The total flux has also increased, typically by a factor of 3. These features are also

observed when the target thickness is increased to 20 µm, though with a reduced maximum energy and beam divergence.

To illustrate how the proton beam profile has improved and become more like a `top-hat' distribution with well defined edges, vertical line outs across the beam for the 5 µm target case are extracted and are presented in Fig. 5.4. To quantify the improvement in the uniformity of the proton beam, a sampling of the proton dose distribution, corresponding to the central 50% of the beam area, is taken for measured energies in the range 3.0 to 8.8 MeV. It is found that the standard deviation of the proton dose from a flat distribution varies from 54% of the mean value for the lowest energy (3.0 MeV) to 11% at the highest energy (8.8 MeV) for the case where no low intensity pulse is used. The corresponding values decrease significantly to 16% and 4%, respectively, for the case where a low intensity pulse is used prior to irradiation by the main laser pulse. For the condition of no significant pre-plasma expansion, fully stripped carbon ions are identified with the Thomson parabola spectrometer in the TAW setup. This is higher than the highest charge state of carbon, C^{4+}, measured with significant pre-plasma expansion at the target front surface. The peak electric field to which these ions are subjected can be estimated, using the approach
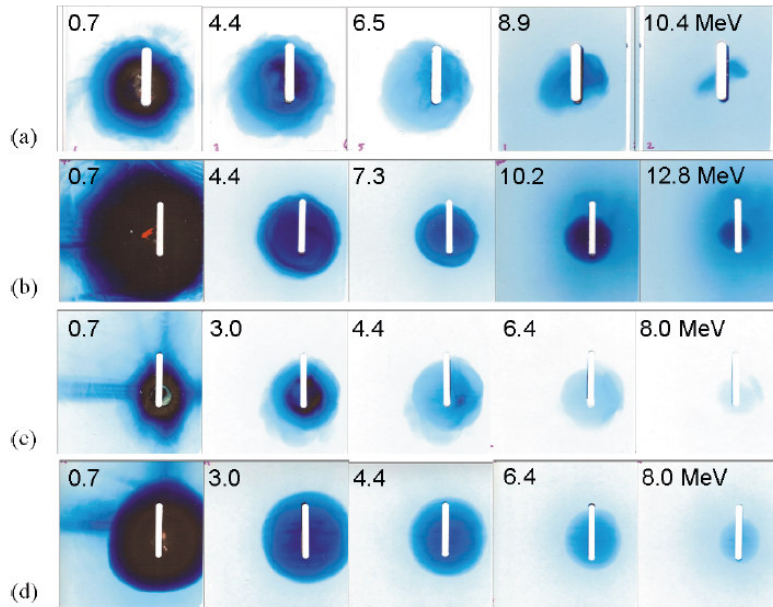
Figure 5.4: Representative examples of the measured proton spatial and energy distributions using RCF from the TAW experiment, obtained with a 5 µm target (a) without and (b) with the low intensity pulse. The corresponding results for a 20 µm target are shown in (c) and (d), respectively. The calculated intensity of the CPA pulse is between 2×10^{19} and 3×10^{19} Wcm^{-2} for all shots. These examples clearly show that the proton beam profile becomes more circular and more uniformly distributed in the presence of the low intensity pulse for both thickness of target. Higher proton flux is indicated on the RCF by a darker blue colour.

described in earlier chapters. This indicates that with a low intensity pulse present the field reduces from ~7.0 TVm^{-1} (no plasma expansion) to 5.3 TVm^{-1} (with plasma expansion). By contrast, the maximum proton energy increased with the pre-plasma expansion. The reason that the field that the carbon ions observe decreases could be because the increased proton flux (see later discussion) leads to greater shielding of the electric field experienced by heavier and slower ions. When the same phase plate is used in the TAP experiment, for similar laser conditions, similar changes to the proton beam parameters are measured. Fig. 5.5
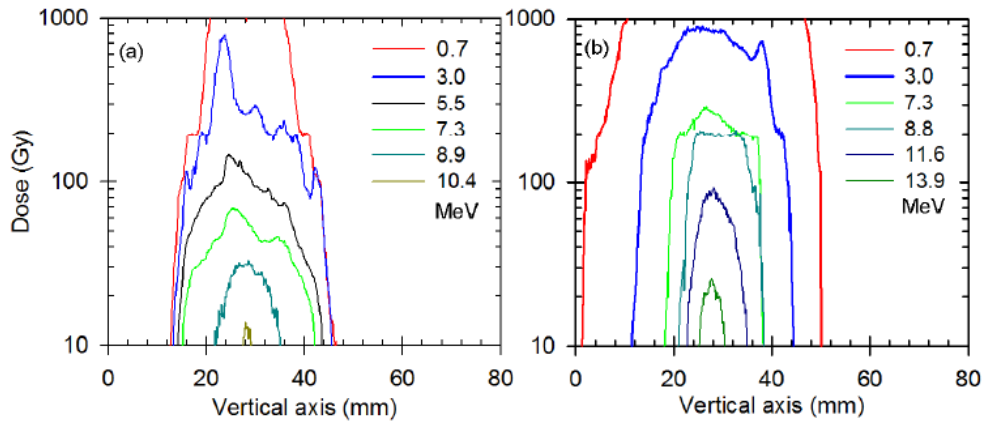
Figure 5.4: Beam profile lineouts as a function of proton energy, taken vertically across the RCF images shown in Fig. 5.3 for the 5 µm target; (a) without and (b) with the low intensity pulse present.

shows optical interferometric probe images of the front surface plasma expansion at 5ps after irradiation by the main laser pulse. The target is irradiated with the low intensity pulse with an annular ring focus for times ranging from 1.0 ns to 5.0 ns prior to the main pulse. The ablation caused by the low intensity pulse results in the contraction of the area with no pre-plasma within the ring. The ablated plasma expands laterally as well as longitudinally, resulting in closure of the ring after a certain expansion time. This results in a jet of plasma shooting outwards from the target. In Fig. 5.5 the secondary point of self emission (bright spot) away from the expanded target surface is observed only for a relative timing of 3.6 ns, and is interpreted as a result of the main pulse interacting with this plasma jet. Further work is required to understand the origin of this emission. To determine the extent that the profile of the pre-plasma at the front of the target influences proton acceleration, the low intensity laser pulse at target is defocused to a spot size comparable to the size (470 µm) of the annular ring focus. It is found that the changes to the proton beam are similar when the defocused low intensity spot is used compared to the `ring'

distribution. To investigate this further, the pre-plasma conditions at the target front surface are varied with the pre-plasma generated using the defocused spot distribution of the low intensity pulse,
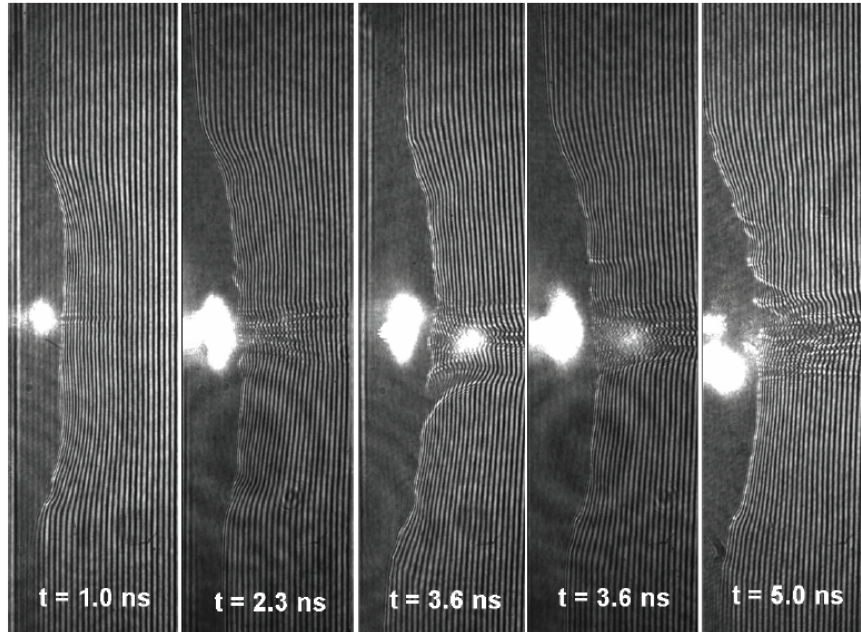

Figure 5.5: Optical interferometric probe images from the TAP experiment, in which a low intensity pulse ($1x10^{12}$ Wcm^{-2}) with an annular ring focus irradiates the target at different times relative to arrival of the main high intensity ($4x10^{20}$ Wcm^{-2}) pulse. The laser pulses are incident from the right. The areas of the image that are dark and have no fringes indicate areas where the plasma density is too high for the probe pulse to penetrate. The bright spot at the point of target expansion is self emission from the target generated from the interaction of the main laser pulse with the expanding surface plasma at critical plasma density. A second bright spot of self emission is observed for the measurements made at 3.6 ns and is believed to be due to interaction between the main laser pulse and the resulting plasma jet from the collapsed ring focus.

as this is a simpler physical system to model. The pre-plasma conditions, characterised by the measured plasma scale length in the underdense region, are varied as a function of two different parameters: the low intensity pulse intensity (I_L) and the delay (Δt) between the arrival of the low intensity pulse and the main pulse. Due to the fact that the optical probe beam diagnostic does not enable measurement of electron densities greater than $\sim 4 \times 10^{19}$ cm^{-2}, computer simulations are required to determine the full initial plasma density profile. 2D hydrodynamic simulations are performed using the Pollux code [184]. A 300 μm by 300 μm grid with a cell size of 1.5 μm is used with the target material set as Cu. The laser wavelength and spot

radius are set at 1.06 µm and 220 µm, respectively, with cylindrical symmetry being exploited to maximise computing efficiency. The pulse has a rise time of 0.2 ns after which it remains at a chosen intensity of $I_L = 1 \times 10^{12}$ Wcm^{-2}. The simulations show two distinct regions of pre-plasma expansion with quite different scale lengths. One region has the scale length that is measurable using the optical probe in the outer part of the pre-plasma and is denoted by L_o.
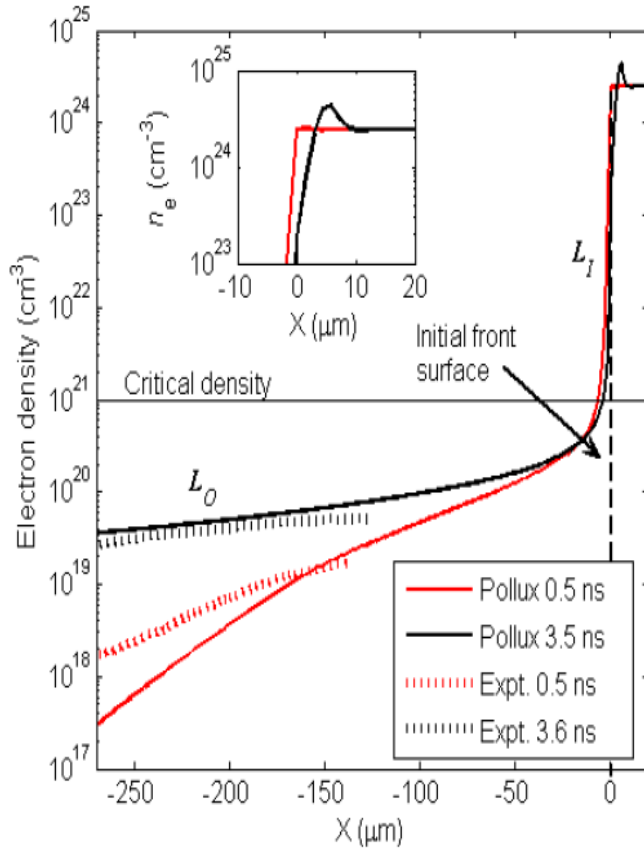

Figure 5.6: Cu target front surface density pro_le as a function of expansion time with onstant I_L = 1 x10^{12} Wcm^{-2}; the solid lines represent the results of the Pollux hydrodynamic code and the dashed lines are the experimentally measured values from the optical probe. X = 0 corresponds to the initial target front surface and is shown on the diagram by the dashed black line. The inset shows the shock wave instigated by the low intensity pulse, represented by the peaks in electron density, propagating inside the target but not reaching the rear surface (X = 25 µm).

The second region is within the area that cannot be measured experimentally due to the higher electron density. The characteristic scale length for this inner area is

denoted by L_I. Fig. 5.6 shows example results with the two regions labelled. For an increase in Δt from 0.5 ns to 3.5 ns, L_o is predicted to increase from 31 µm to 182 µm, which corresponds quite well with the measured value of 50 ± 10 µm increasing to 200 ± 40 µm (Fig. 5.6). The simulation results show that the value of L_I increases from ~0.6 µm to ~ 0.9 µm for Δt increasing from 0.5 ns to 3.5 ns. Experimentally the target and main pulse parameters are kept constant as I_L is varied from 5 x10^{11} to 5 x 10^{12} Wcm^{-2}, for constant $\Delta t = 0.5$ ns. A second parameter scan is performed with I_L kept constant at ~1x10^{12} Wcm^{-2} and Δt varied from 0.5 ns to 3.6 ns. The sample spectra resulting from these parameter scans are shown in Fig. 5.7, with the corresponding plasma scale length values measured from the optical probe for the underdense region also shown. It can be seen for both cases that a plasma scale length $L_o < 60$ µm results in an enhanced proton spectra with higher fluxes for all energies and a higher maximum proton energy compared to the case with no or very little pre-plasma. As the plasma scale length is increased to $60 < L_o < 120$ µm the maximum proton energy and the proton numbers at all energies are reduced to similar values to the case without a low intensity pulse. Increasing the plasma scale length yet further, $L_o > 120$ µm, results in a proton spectra with smaller proton flux and a lower maximum proton energy. The spectra shown in Fig. 5.7 indicate that there is an optimum range for the plasma scale length. Fig. 5.8 presents the measured maximum proton energy (a) and the conversion efficiency of laser energy into proton kinetic energy (b) as a function of L_o. The measured maximum proton energy increases by ~25% for an increase in L_o from ~ 0 to ~ 60 µm and the conversion efficiency improves by a factor of ~ 2. Note that the conversion efficiency only includes proton energies above 2.4 MeV, as this is the lower detection threshold for the RCF stack design used. Above $L_o = 100$ µm the maximum proton energy and conversion
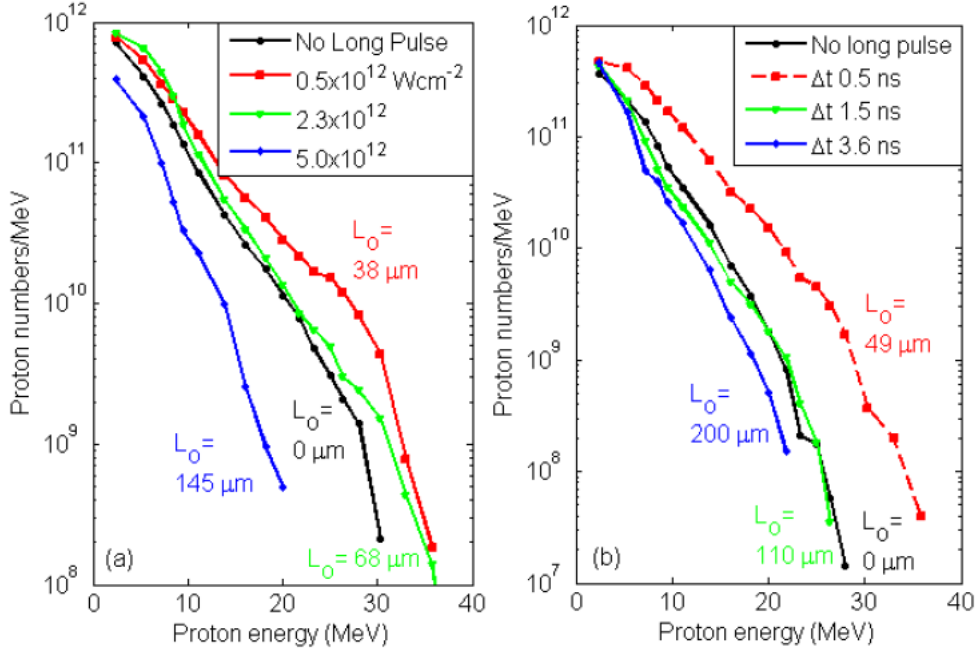
efficiency

Figure 5.7: Example proton energy spectra measured using a RCF stack; (a) for different I_L and fixed $\Delta t = 0.5$ ns and (b) for constant $I_L \sim 1x10^{12}$ Wcm^{-2} and different Δt. The values beside each curve is the measured plasma scale length (L_O) obtained from the optical probe.

drop below the values measured for the case where no pre-pulse is used. An optimum plasma scale length is observed for increasing the maximum proton energy and conversion efficiency. However, the proton beam spatial profile is found to improve with increasing plasma scale length. Lineouts and sample RCF images are shown in Fig. 5.9, which shows that the flux distribution becomes smoother with increasing I_L and therefore increasing L_o. Using the same technique used above for the TAW experiment the uniformity of the proton flux is quantified by the standard deviation from a flat distribution for a central sample region of the beam that corresponds to 50% of the beam area. It is found that the standard deviation of the proton dose for 9.5 MeV protons decreases from 36% of the mean value, with no low intensity pulse used, to 19% for a shot where $L_o = 145$ μm. It is observed that the proton beam, in the case of preplasma expansion, becomes more circular. This can be quantified by using the following formula, circularity $=4\pi$.Area=(Circumference)^2. It is found that the proton beam spatial profile for 9.5 MeV protons for a typical shot without a pre-plasma deviates from a perfect circle by 4% and for the same proton energy with Lo = 145

µm the deviation is reduced to 1%. To determine the size of the area on the rear surface of the target that the proton beam is emitted from, Au targets with the groove structure shown in Fig. 5.2 are used. Because the structure on the target surface is imprinted into the proton beam, as shown by Roth et al [72], this can be used to
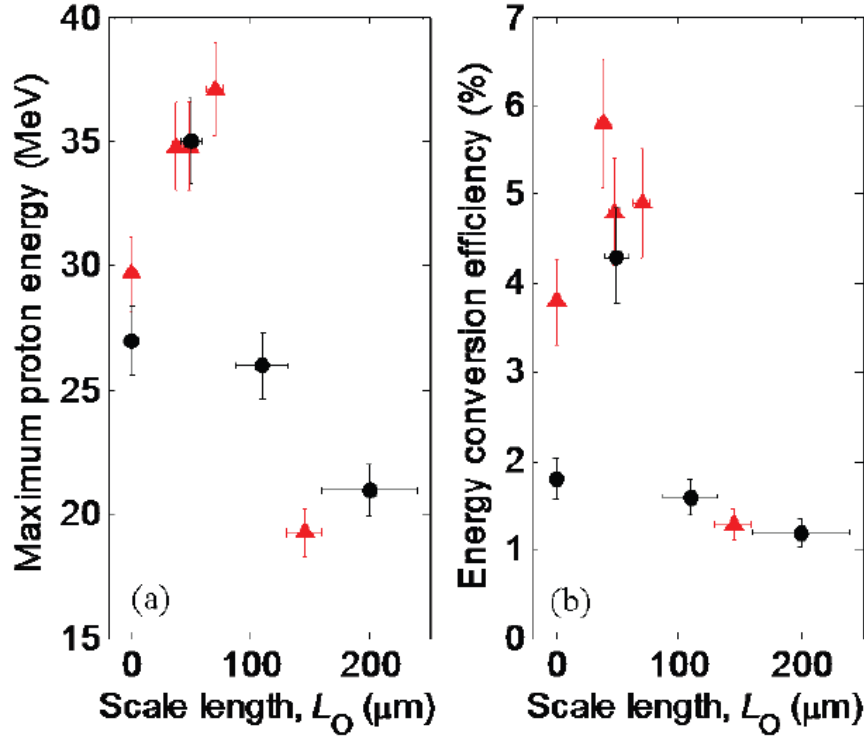

Figure 5.8: (a) Maximum proton energy and (b) Laser-to-proton energy conversion efficiency as a function of L_o, obtained for different I_L up to $5x10^{12}$ Wcm^{-2} for fixed $\Delta t = 0.5$ ns (Red triangles), and for different Δt up to 3.6 ns for fixed $I_L \sim 1 \times 10^{12}$ Wcm^{-2} (Black circles).

determine the proton source size. By counting the number of lines (of known separation on the target, 10 µm) observed in the proton beam image the source size for different energies can be determined. The sources sizes obtained in this way for the I_L parameter scan are shown in Fig. 5.10. It is observed that the proton source size decreases for increasing proton energy, going from ~ 600 µm at 4 MeV to ~ 50 µm at 30 MeV. An increase in source size is measured for all energies for the case where the plasma scale length is within the optimum range, $L_o \sim 40$ µm ($I_L = 5 \times 10^{11}$ Wcm^{-2}).
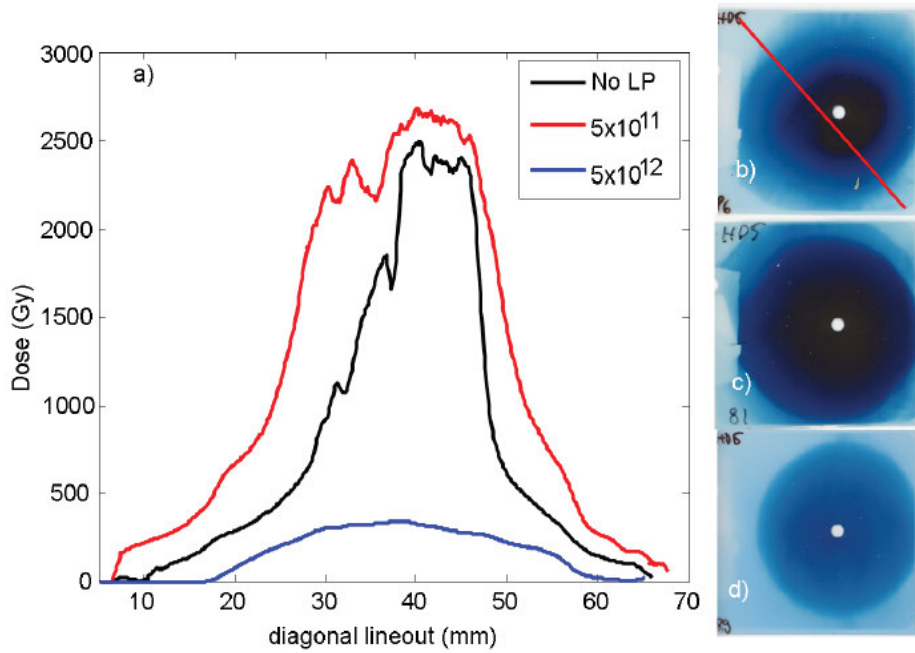
*Figure 5.9: a) Diagonal lineouts of RCF images for 9.5 MeV protons. RCF images for b)
without the presence of the low intensity pulse , c) with the low intensity pulse equal to 5 x10^{11}
Wcm^{-2} and d) with 5 x 10^{12} Wcm^{-2}.*

Source size measurements for large values of L_0 could not be made because the line
structure is not resolvable. The virtual source size, the parameter most useful for
imaging applications, can be calculated by tracing the line structure in the proton
beam back through the known groove structure on the target rear surface to an
effective (virtual) source. The virtual source size without the low intensity pulse is 11
µm for 6.2 MeV and 17.6 MeV protons. With the addition of the low intensity pulse
at 5x10^{11} Wcm^{-2} the virtual source size is 12 µm and 7 µm at 6.2 MeV and 17.6 MeV
energies respectively. The interferometric optical probe images shown in Fig. 5.12
indicate that the observed changes in the proton beam are likely due to changes to the
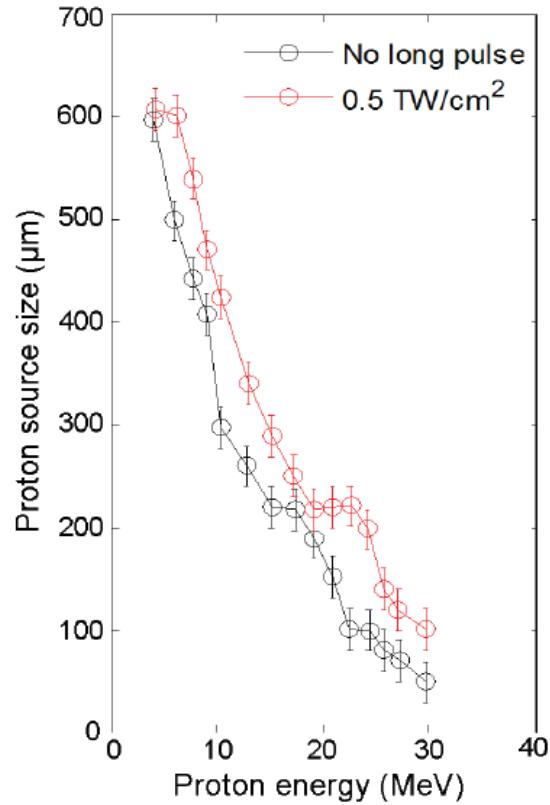main laser pulse propagating in the expanding pre-plasma. In Fig. 5.12(a) a single

Figure 5.10: Source size measurements obtained from grooved targets by counting lines in proton beam. Source size measurements for a pre-pulse intensity of $5x10^{12}$ Wcm^{-2} could not be made as it is not possible to resolve the line structure signal in the beam profile

channel can be observed which is narrower than the focusing cone of the main laser pulse and is evidence for self-focusing of the main beam. The self-focusing of the beam results in a smaller focal spot near the critical density surface and hence a higher intensity than the case where there is no pre- plasma. The enhanced conversion efficiency for this case also indicates that the absorption of the laser pulse is enhanced. By contrast, for a very long scale length pre-plasma the main laser pulse is observed to filament [73, 74], as shown in Fig. 5.11(b), resulting in energy deposition over a larger area than the normal focal spot size, thus reducing the laser intensity at target. Self-focusing occurs in the underdense plasma as the laser intensity alters the refractive index profile of the plasma and causes it to act as a focusing lens. Laser pulse propagation instabilities due to the plasma grow becomes more dominant in larger scale length plasma.
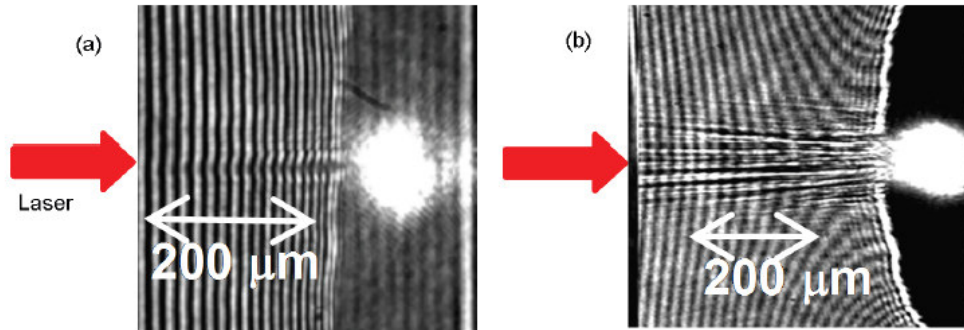
Figure 5.11: Example interferometric probe images (a) showing channelling of the CPA laser beam in relatively short scale length pre-plasma and (b) showing filamentation of the CPA laser beam in long scale length pre-plasma. The bright spots in the images are self emission near the critical density surface.

5.4 PIC simulations

To give insight into the importance of changes to the fast electron generation and transport in the inner pre-plasma region, which cannot be directly measured, OSIRIS [75] PIC simulations are performed (by Prof. R.G. Evans). A 40 µm (axial) by 20 µm (transverse) grid with 8000 by 4000 cells, and 4 electrons and 4 ions per cell, is used. The laser is linearly polarized with the E-vector in the simulation plane, and the focal spot is 10 µm. The laser pulse duration is limited to 60 fs (at top) due to available computing resources, and the measurements are made 40 fs after the start of the pulse. Shown in Fig. 5.13(a)-(c) are the electron density maps for three different plasma density profiles. Fig. 5.13(a) is the case where there is a relatively sharp density gradient. In Fig. 5.13(b) the density gradient profile used is the Pollux code simulation result after 0.5 ns expansion, i.e. $L_I = 0.6$ µm and $L_o = 31$ µm (Fig. 5.6). It can be seen that the size of the laser focus is smaller than the sharp density gradient profile case, which implies self-focusing of the laser pulse, in qualitative agreement with the experimental observation. For the result shown in Fig. 5.12(c) the initial density profile is obtained from the Pollux simulation after 3.6 ns (Fig. 5.6). The channel of the laser pulse is still narrowing, but propagation instabilites are observed, again in qualitative agreement with the experimental observations. The electron spectra for the three different cases, integrated over all forward moving electrons, are shown in Fig.

5.12(d). For the cases in which the plasma extends over a large distance from the target the electron flux has significantly increased, especially above 10 MeV. However, little difference between the two cases is observed when comparing the spectra for the 0.5 ns and 3.5 ns expansion cases.
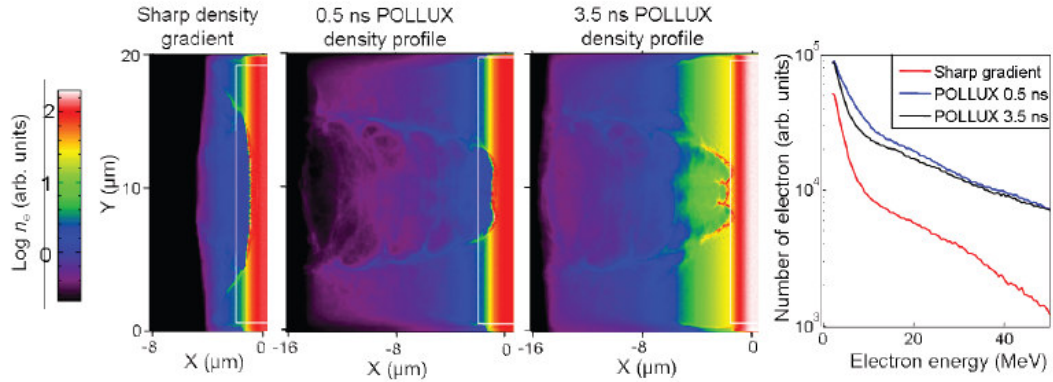

Figure 5.12: Electron density, ne, maps illustrating the shape of the laser plasma interface for different density gradient profiles. (a) The case of a sharp density gradient where there is little pre-plasma expansion. (b) The density profile provided by the Pollux simulation for Δt = 0.5 ns. Note that the laser focus is narrower vertically than for case (a). (c) This case uses the Δt = 3.5 ns output density profile of the Pollux simulation and shows that instabilities are starting to appear. The colour scale varies from red through blue to black, where red represents the highest densities (initial target density) and black is vacuum. (d) Integrated electron energy distribution for forward directed electrons for simulation results (a)-(c). The CPA laser is incident from the left in (a)-(c).

The Pollux simulations predict a limited range of L_l values, up to 0.9 µm, for the range of parameters experimentally investigated. To determine what effect a larger range of L_l values would have, simulation runs are performed for a single exponential electron density profile with scale length in the range 0.46 to 4.6 µm. Results are presented in Fig. 5.13. A 40 µm (axial) by 20 µm (transverse) grid with 8000 by 4000 cells, and 4 electrons and 4 ions per cell, is used. The laser is
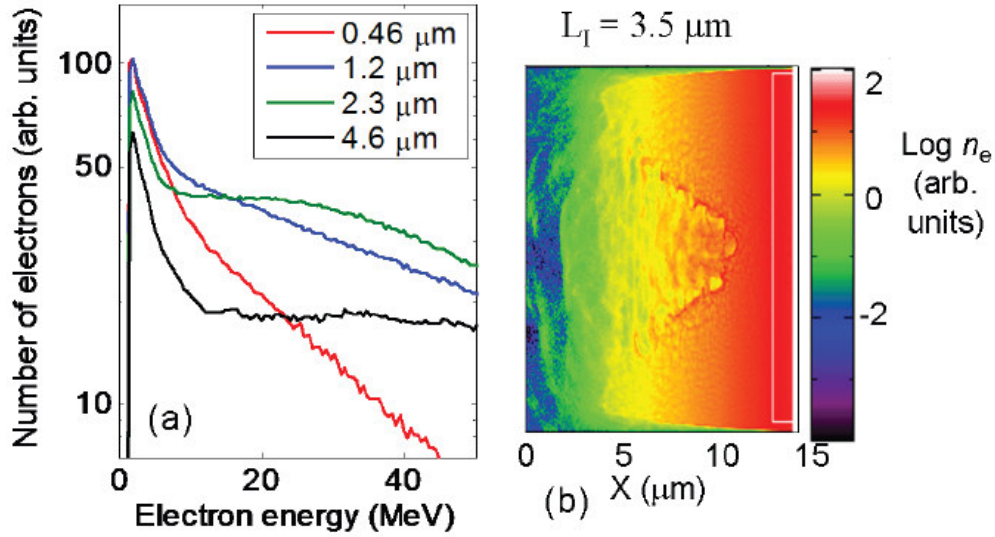
Figure 5.13: (a) Electron energy distribution of forward moving electrons as a function of the density scale length at the critical density surface, L_I ; (b) Electron density, ne, map illustrating the shape of the laser-plasma interface for L_I equal to 3.5 µm.

linearly polarized with the E-vector in the simulation plane, and the focal spot is 9 µm. Measurements are made 100 fs after the start of the pulse. It is found that as the scale length is increased from 0.46 µm to the order of the laser wavelength, the flux of electrons with energies above 10 MeV is significantly increased, as shown in Fig. 5.13(a). For a larger pre-plasma expansion the laser starts to experience much greater instabilities, as evident from the electron density map shown in Fig. 5.13(b), and the irradiance, in the region of the critical density, decreases, resulting in a reduction of the electron flux accelerated. We note that for these conditions, a small number of very energetic electrons are produced, as evidenced by the flattening of the electron spectrum in Fig. 5.13(a). This suggests that for very long pre-plasma scale lengths underdense acceleration processes, likely similar to the wake field mechanism, become important. The simulation results suggest that optimum pre-plasma scale lengths exist for coupling laser energy into protons, via fast electrons. The simulations also indicate that the main laser pulse begins to be disrupted due to instability growth in long scale length pre-plasma, reducing the coupling efficiency of the laser into the plasma.

Rear surface sheath distribution

The changes in the measured proton beam divergence can be interpreted in the framework of the target normal sheath acceleration (TNSA) mechanism [76]. Fast electrons, which are accelerated through the target by the main laser pulse, become electrostatically confined to the target rear surface, building a sheath with a quasi-static charge separation field, which ionizes and accelerates atoms at the rear surface. Protons are accelerated normal to iso-density contours in the sheath [77], and hence the measured spatial profile of the accelerated proton beam is sensitive to the shape of the sheath. The spatial profile of the sheath, and hence the ion front, is typically Gaussian shaped, as inferred from measurements by Fuchs et al [77] and shown experimentally by Romagnani et al [78]. Any changes to the proton beam divergence can therefore be interpreted as a change in the shape of the acceleration sheath, induced by the presence of the low intensity laser pulse. Evidence of a change to the sheath shape is inferred from observed changes to the angular divergence of the proton beam as a function of energy. It has previously been shown, with single high intensity laser beam irradiation of a target foil, that the angular envelope of the proton beam decreases with energy [79, 80, 81], and that this is due to a decrease in size of the emission region near the peak of the Gaussian-shaped electron sheath [79, 82]. We find that the divergence characteristics of the proton beam changes significantly with a long scale length pre-plasma, as shown in the measurements of Fig. 5.13. In the absence of the low intensity pulse, it is consistently observed that the spatial extent of the beam is fairly constant for low proton energies and decreases only at the highest energies. This manifests itself in the plateau-like distribution at low energies in Fig. 5.14(a) and is quite different to the near-linear dependence of the divergence on proton energy consistently observed with significant preplasma expansion, shown in Fig. 5.14(b), for otherwise identical target and laser conditions. The measured changes to the proton beam divergence as a function of energy can be explained by changes to the spatial distribution of the sheath.
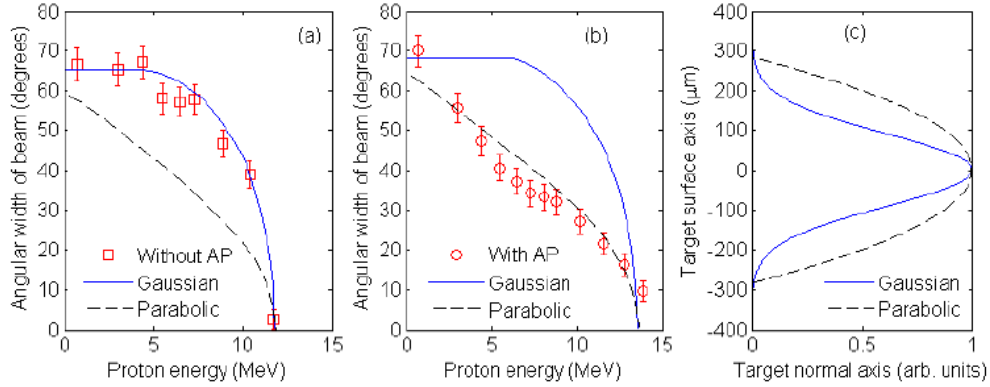
Figure 5.14: (a) Symbols correspond to the measured angular divergence of the proton beam as a function of proton energy for the 5 μm target sample measurements of Fig. 5.4, without the low intensity pulse; (b) corresponding measurements with a pre-plasma expansion. The lines are the calculated divergence as a function of energy using the Gaussian (solid blue line) and the parabolic (dashed black line) sheath spatial distributions shown in (c). With the main laser beam only, a sheath with a Gaussian distribution with a FWHM of 220 μm produces a good Δt to the experimental results in (a), whereas with pre-plasma expansion a better Δt to the experimental measurements is obtained with a parabolic sheath distribution with a FWHM of 400 μm, as shown in (b).

To illustrate this, a model is devised to determine the sheath shape by fitting to the experimental measurements of proton beam divergence. The model calculates the spatial distribution of the expanding ion front, and the divergence and energy of protons produced along the ion front, as a function of time for a defined spatial and temporal distribution of the electric field. The temporal profile of the electric field is assumed to be Gaussian with a FWHM equal to 1.2 ps similar to the laser pulse duration. The peak strength of the field is chosen to reproduce the maximum detected energy of the accelerated protons. The model uses the threshold field for the ionisation of hydrogen (assuming field ionisation to be the dominant ionisation mechanism at the rear surface of the target) to define the spatial extent of the proton source as a function of time. The ion front expands into vacuum and the velocity components and hence proton energy as a function of radius from the centre of the sheath is calculated in 0.1 ps steps over a 4 ps range defined by the temporal profile of the electric field. The local normal at each point along the ion front surface is calculated as it evolves spatially and temporally to determine the angle of proton emission. Using the measured sheath distributions reported by Romagnani et al [83]

as a starting point, the sheath shape is initially assumed to have a Gaussian
distribution. It is found that this results in a calculated proton beam divergence
distribution which fits well to the experimental measurements without pre-plasma
expansion, as shown in Fig. 5.14(a), when the FWHM of the distribution is equal to
220 μm. The normalised spatial distribution of the sheath is shown in Fig. 5.14(c).
Various sheath shapes and sizes are employed to reproduce the measured changes to
the divergence as a function of proton energy when the low intensity pulse is added. It
is found that very good agreement with the experimental data is achieved, as shown in
Fig. 5.14(b), when an inverse parabolic sheath profile with a FWHM of 400 μm is
used (Fig. 5.14(c)). Brambrink et al. used an inverse parabolic profile of the ion front
in their modelling of ion divergence from laser irradiated foil targets as it gives a good
fit to their experimental data. With the low intensity beam present, slightly higher
maximum electric field strength is required to produce the higher measured proton
energy. The calculated divergence as a function of energy for both sheath
distributions and both peak electric fields are shown in Fig. 5.14(a) and (b). When the
divergence of the proton beams produced in the TAP experiment are analysed and the
model applied for these parameters some interesting features are observed. First the
shots without any low intensity beam present are considered. The beam divergence
for two of these shots is shown in Fig. 5.15(a) as the black data points. The plateau
observed in the proton beam divergence extends up to proton energies of 10 MeV,
and decreases linearly with energy up to the maximum proton energy. The beam
divergence data for $\Delta t = 0.5$ ns and $\Delta t = 3.6$ ns is larger and smaller respectively (Fig.
5.15). The sheath shape and size as determined by the above model changes with Δt.
The FWHM sheath size increases from 460 μm to 610 μm for Δt increases from $\Delta t =$
0.5 ns to $\Delta t = 3.6$ ns. Fig. 5.15(b) shows the normalised sheath shapes used to
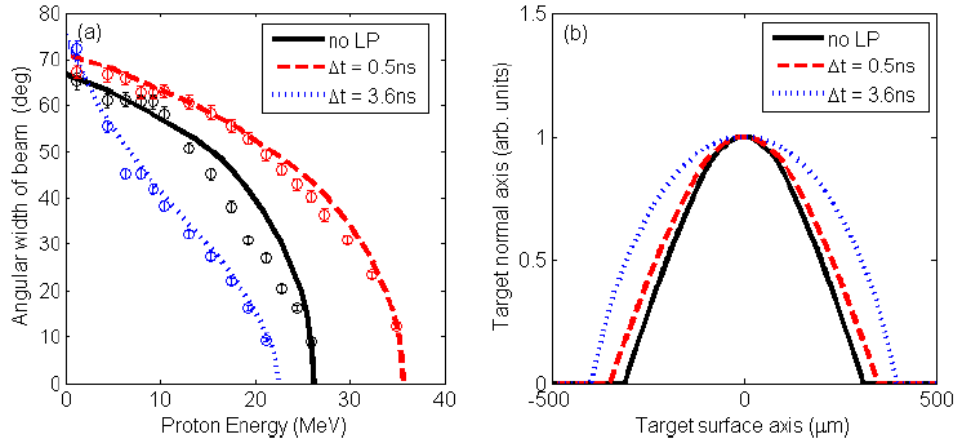provide the fits to the data in Fig. 5.15(a).

Figure 5.15: (a) Beam divergence as a function of proton energy for example Δt, symbols are experimental data. Lines are fits using inferred sheath shapes. (b) the normalised ion accelerating sheath distributions that best fit the beam divergence data in (a).

The shape and lateral extent of the sheath, and the uniformity and spatial profile of the proton beam, are determined by a number of properties. These include the number and distribution of hot electrons generated at the target front surface and accelerated into the foil, and the transport, including refluxing [84] of the hot electrons within the foil. With the low intensity beam present, the ion front distribution and the profile of the proton beam changes, which suggests that the properties of the hot electron generation at the front surface and/or the lateral spreading of the hot electrons within the foil are modified.

5.5 Summary

The first systematic study, in which the effects of a well controlled and characterised pre-plasma at the target front surface on proton acceleration from the rear surface is reported. It is shown that optimum pre-plasma expansion conditions exist for coupling laser energy to protons, via fast electrons. The measured enhancement in proton beam maximum energy and conversion efficiency are likely due to changes to the propagation of the laser pulse in the low density large scale length pre-plasma. Self-focusing and beam breakup are observed experimentally and in PIC simulations and can explain the observed changes to the proton acceleration.

Chapter 6

Proton Radiography of Laser Driven

Cylindrical Implosion

6.1 Introduction:

One of the most important scientific breakthroughs in the past century was the discovery that a beam of x rays could penetrate matter and produce a radiograph that revealed the inside of objects. X-radiography is today an indispensable tool for medicine, industry, and science. Physicists have considered using protons, the positively charged constituents of atomic nuclei, as a way to penetrate thick materials more effectively than x rays. Proton radiography has been used for medical imaging and to treat some types of cancer. Early tests with protons as a radiographic probe were not promising: the radiographs were blurred, an effect caused by the scattering of protons as they move through an object because of their electrical charge. The quest was largely abandoned until 1995, when physicists at Los Alamos National Laboratory came up with the idea of using a magnetic lens to focus the scattered protons into a clear image.[85]
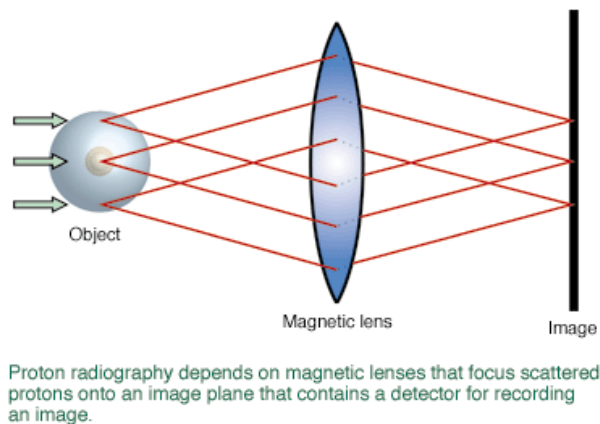

Proton radiography depends on magnetic lenses that focus scattered protons onto an image plane that contains a detector for recording an image.

Figure 6.1

protons interact with other protons and neutrons by colliding with them by way of strong and electromagnetic interactions. The strong interaction has a short range (about 1 fermi, or 10-15 meters), In case of proton-proton interaction the main acting force is electric one, because in the case of proton-neutron interaction it is instead the strong (nuclear) force and neutrons don't have the electric field. The probability of collision with the nuclei is indicated by a material cross section and is dependent upon the number of protons and neutrons in the nucleus.

6.1.1 How Protons interact with Matter

A proton interacting with a nucleus via the strong interaction can do so either

1- elastically or

2- Inelastically

If the interaction is elastic, the proton scatters at some angle, retaining its identity as a proton and maintaining most of its original momentum. If the interaction is inelastic, the proton is "absorbed" in the interaction. That is, it transfers most of its energy to breaking up the nucleus, in the process producing subatomic particles called pions. Because protons carry an electrical charge, they also interact with matter through long-range electromagnetic forces. This interaction takes two forms: with the electric field of nuclei and with the atomic electrons orbiting nuclei. The effects are quite distinct. Interacting with nuclei's electric field is termed elastic scattering and produces a small change in the proton's direction. The effects of each of the small scatters can accumulate, a phenomenon called multiple coulomb scattering. The consequence of multiple scattering for proton radiography is important, especially for dense materials, because ultimately it blurs a radiograph.

The proton interactions with atomic electrons are generally inelastic; that is, the proton loses a small amount of energy by ionizing atoms (kicking an electron out of its orbit). These interactions generally do not result in much change to the proton direction, but many scatters do reduce the proton energy. With dense materials, the energy loss can be quite large. The amount of energy loss can be important, depending on the energy of the beam.
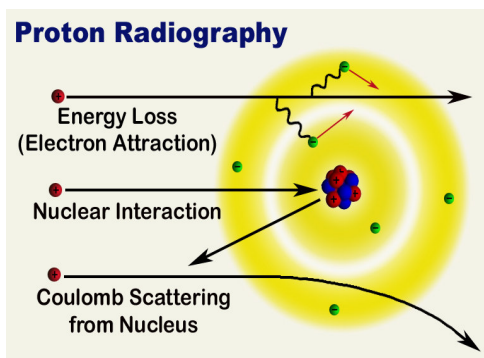

Figure 6.2

6.2 Proton Radiography (in the context of Fast Ignition):

Theoretical and experimental studies of the properties of highly compressed matter are of fundamental interest to several branches of physics, including inertial confinement fusion (ICF), astrophysics and geophysics. For example, in the conventional, isobaric approach to fast ignition, cryogenic deuterium tritium fuel has to be compressed from an initial diameter of 2 mm to a 60 µm diameter hotspot, resulting in mass density 'ρ' ranging from 100 g/cc to 600 g/cc around the cold fuel-hot spot interface region, with an areal density 'ρR' of 0.3 g/cm^2. In order to achieve these extremely high densities, the compressed core must be spherically symmetric with a relatively smooth interface between the cold fuel and the central hot ignition region [86]. Diagnosing density perturbations and general deformity of the core shape in these conditions is required in order to understand the underlying physical process.

Similarly, the knowledge of 'Equation of State' (EOS) of heavily dense and compressed matter is important for several fields of physics. For instance, the evolution of the stars is mainly governed by the thermodynamic properties of matter at very high temperature and pressure. EOS of the planet cores is also a fundamental requirement for the understanding of their internal structures [87]. Moreover, success of ICF also relies on the knowledge of EOS of the extreme state of DT fuel, which is required in order to understand the phenomenon of shell pellet implosion and the final core compression.

In recent day shock-wave-EOS experiments, dense compressed matter is created by means of laser produced shock waves. Measurement of the shock/fluid velocity or the density profile of the compressed medium is required, with high precision, in order to obtain the EOS values.

While a few experiments have used X-ray radiography in order to obtain the density profile of compressed low-Z materials [88], most of them [89,90] rely on the shock velocity measurement (via optical interferometry in transparent media or by observation of shock breakout times on steps of known thickness in optically opaque materials). In opaque high/average Z materials, it is not possible to obtain information about the density profile of the shocked sample and also to measure the fluid velocities directly. Moreover, in measurements based on velocity determination, it is impossible to have a good precision, contrary to the measurement based on density

diagnosis, due to error amplification going through Rankinee Hugoniot relations [91,92]. It is a challenge to the conventional radiographic techniques to probe the above-said dense matter states. Similarly, in ICF experiments, the ideal diagnostic would penetrate densities up to 600 g/cc and resolve features of less than 5-10 μm. Imaging of neutron/proton emission from an igniting core is capable of providing such resolution during ignition shots, however, it is not certain that a target that does not reach ignition will not produce the large number of neutrons/protons required to image the core using this technique [93-95]. Another possibility, currently under development, is X-ray imaging in the range of 15-30 KeV [96].

6.3 Comparison of Laser-Driven Protons and Conventional protons for Radiography

The proton radiography technique (as will be discussed in the following section), employing proton beams driven by high power lasers, can be developed as an alternative, or perhaps complementary, technique to probe the density perturbations in highly dense materials. The idea of using ion beams, and particularly proton beams, for radiography purposes has been circulated for several decades [97,98]. High energy (~GeV) and monochromatic beams of ions from conventional accelerators have been used for detecting the areal density variations in samples by exploiting the energy deposition and scattering of the incident particles [99]. However, the long pulse duration and high production cost of such ion pulses have been major drawbacks, in view of employing them as a particle probe in many cases, such as in high power laser plasma experiments. On the other hand, the unique properties of high power laser accelerated multi-MeV protons [100], such as high brilliance in a very short duration, high directionality and highly laminar flow, are favourable for achieving high spatial resolution with desired magnification, when back illuminating an object with the proton beam via point-projection imaging scheme. Proton beams with substantial flux in the range of 50-60 MeV can be produced by focusing a petawatt-class laser on a thin foil target [101,102] and it is reasonable to expect that higher energies will be obtained soon due to the rapid growth in laser technology and extensive scientific research in the field. Therefore, picosecond laser-driven proton radiography appears as a potential candidate to probe dynamic events in very dense matter, such as the imploded ICF cores where density of about 500 g/cc can be found. One of the

attractions of the proton radiography technique is the intrinsic high spatial resolution (of a few microns [99,102]). In a point-projection imaging scheme, resolution depends upon the source with diameter unless it is a perfectly laminar source. The results of a series of investigations on the source properties consistently showed that protons are emitted in a laminar fashion from an area of the target much larger than suggested by the resolution tests [99,103-105] Indeed. The magnification test suggested that the virtual source of protons is located at few hundred micrometers behind (on the side of laser incidence) flat foil generating the protons. Several experiments have been carried out in which laser-driven proton beams have been employed as a backlighter for static and dynamic objects (produced by laser interaction). Particularly successful has been the application of these proton beams to the detection of highly transient electric and magnetic fields generated during laser-matter interactions. The structure and dynamics of the fields is in this case was retrieved by matching experimental proton deflection patterns to synthetic maps obtained with particle tracing codes, modelling the propagation of protons through prescribed field distributions. A description of the principles and results of this particular application can be found in Ref. [99]. Transverse (to the probe proton beam) density variations in the object can be imprinted over the detector films via modifications in the proton beam cross-section, caused by differential stopping and scattering.

6.4 Fundamentals of proton radiography

Each atom in matter behaves like a scattering centre for incident charged particles, due to the presence of the surrounding Coulomb potential barrier. Therefore, the final velocity (i.e. the energy as well as the direction) of the incident particle after passing through a given object depends on the total number of scattering centres with which the particle has interacted along its way [107]. Consequently, the final velocity of the incident particle will be different after crossing different sections of a probed object having different areal densities (density thickness). We can imagine a diverging proton beam of broad energy spectrum (example, high power laser accelerated proton beam from solid targets) as composed of many monoenergetic beamlets. When probing an object with a given transverse areal density profile, each monoenergetic incident beamlet will emerge with a certain transverse straggling (due to multiple small-angle scatterings) and energy spread (mainly due to electronic energy losses

[107, 108] during scatterings) depending on the areal density of the object they experience. Information on the transverse distribution and energy of the protons emerging from the sample can be obtained employing thin sheet detectors, such as radiochromic film (RCF) [109,110], in a multilayer stack. Radiochromic films (RCFs) are self-developing ionizing radiation (e.g. electrons, ions, ionizing radiations such as X-rays and Gamma rays) sensitive detectors which change its optical density upon exposure. The main component of these films is the thin layer of radiation-sensitive material (also called active layer), which is sandwiched between optically transparent plastic layers, in order to provide mechanical support. The final optical density (o.d.) profile across a given radiograph thus produced will be due to the sum of the contributions from each proton passing through it. Most of the deposited dose is contributed by protons within a narrow energy band, depending upon the type of RCF and its position in the stack. This is because of the property of ions having a sharp and narrow peak, called Bragg peak, in their dose deposition curve close to their stopping range.

There has been significant interest devoted to developing analytical theories of multiple Coulomb scattering of an incident particle by matter [107]. However, due to the statistical nature of the process, these theories are only capable of providing estimations of scattered beam parameters, such as energy and transverse spread. For example, Highland's formula [111] is given by

$$\theta_{FWHM}[radian] = E_s \frac{z}{2E[MeV]} \sqrt{\frac{\rho[g/cm^2] \times l[cm]}{L_{rad}[g/cm^2]}}$$

And can be used for a quick estimation of the FWHM spread of particle beamlet (of energy E and charge Ze) scattered by an object of density ρ and thickness l. Here L_{rad} (called radiation length) is a term dependent on the scattering material and can be found in the literature [112]. 'E_s' in Eq. (1) is a constant which in fact depends on various parameters of the target and the incident particles.

Even when the energy loss of the protons while passing through the object is negligible, changes in their directions of motion due to the multiple small-angle scatterings are sufficient to produce an imprint of the object over the detector [19,27].

The transverse straggling of probe proton beam, which depends inversely on the energy of the probe protons, determines the minimum resolvable (threshold) areal density of the object. Let us assume a Gaussian spreading of probe proton beamlets with FWHM spread angles of θ_{obj} while propagating through an infinitesimal object. If D is the unperturbed dose level of the detector, the normalized dose depression ($\Delta D/D$), at the respective magnified position of the object over the detector, will be

$$\frac{\Delta D}{D} = 1 - \sqrt{\frac{\ln(2)}{\pi}} \frac{2t}{x\theta_{obj}}$$

where, t is the transverse extent of the object and x is the distance of the detector from the object. Depending on the dynamic range of the detector sensitivity as well as the 'noise' fluctuations in dose level, the threshold areal density for a given incident probe proton energy can be easily estimated.

Similarly, the FWHM of the resulting Gaussian dose depression profile on the detector (ξ) will be equal to the FWHM of the scattered beam from the probed object, i.e. $\xi = x\theta_{obj.}$ ξ can also be seen as a blurring coefficient, because, in the case of an object with finite transverse dimension t, the FWHM size of the image over the detector will be the convolution of the x and the magnified size of the object. In a point-projection imaging scheme, it would correspond to $\sim \sqrt{\xi^2 + (L \times t/l^2)}$, where L and l are the distances of the object and the detector from the proton source, respectively. Clearly, the transverse spread of the probe beam controls the blurring of a radiographic image. Hence increase in the probe proton energy is essential in order to reduce the blurring effect.

6.6 Goal of the Experiment

The experiment was performed at the Rutherford Appleton Laboratory (UK) to study fast electron propagation in cylindrically compressed targets, a subject of interest for fast ignition. The fast-ignition approach to the inertial confinement fusion scheme requires warm and dense plasma in which hot electrons propagate [**Error! Reference source not found.**13]. Until now, many of the experiments carried out on this subject were designed to study transport in cold planar targets at standard density. Such experiments may exhibit a different behaviour of the hot electrons transport issues,

compared to the final design. In order to get closer to this objective, the cylindrical geometry can be an important step to be studied [114]. I have used this geometry in this experiment performed on the VULCAN TAW laser facility at RAL in two phases as shown in figure 6.3.
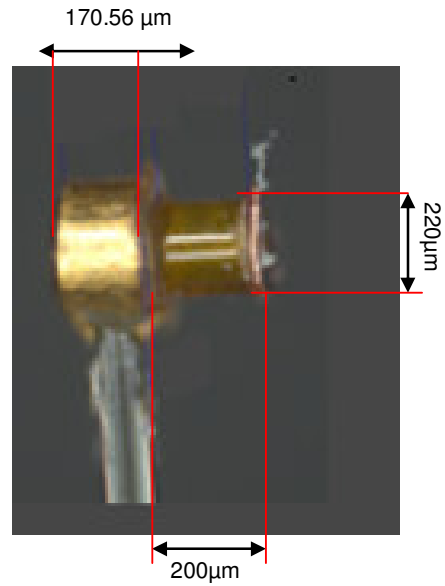

Figure 6.3: It shows the REAL CYLINDRICAL TARGET used in the reported experiment. This target is prepared at RAL by M.Tolley and Ch. Spindloe
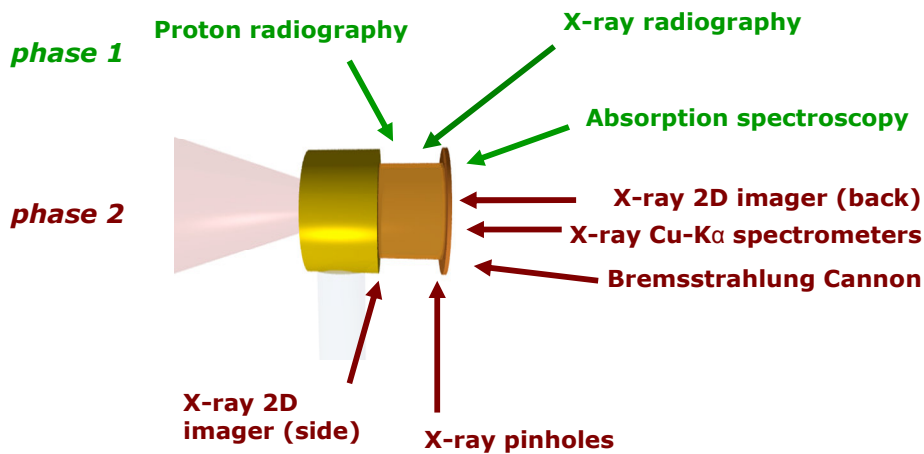

Figure 6.4: It shows the schematic of the experiment in two phases. In phase 1, the density and temperature radial profile of the imploding target was measured. In phase 2, transportation of hot electrons was studied in the compressed core which is not part of this thesis.

Figure 6.3 shows the real cylindrical targets used in this experiment and figure 6.4 shows the schematic of the diagnostics used in phase 1 and 2 of this experiment.

1- The first phase is being reported in this thesis, consisted in studying the cylindrical target compression to evaluate the core density and temperature radial profiles at different moments of the cylindrical imploding targets.

2- The second phase was devoted to the study of fast electrons propagation in such compressed targets, which is not being reported/concentrated as part of this thesis.

Very few laser installations are now able to be set up in such geometry, while having an additional short-pulse beam to produce the hot electrons as necessary for fast-ignition.

6.7 Proton radiography diagnostics

Outline of the experimental and analytical scheme:

I will emphasise the diagnostics used in phase 1. In the experiment, protons accelerated by a ps laser pulse have been used to radiograph the 220 μm-diameter, 20 μm-wall cylinder filled with 0.1 g/cc foam, imploded with ~200 J of green laser light in 4 symmetrically incident beams of pulse length 1 ns. Point projection proton backlighting was used to measure the compression history and the stagnation time. Results were also compared to those from a hard X-ray radiography diagnostics.

Moreover, in this thesis I report the first complete time dependent MC simulation of proton propagation in compressed target in which all the relevant physical effects such as the Multiple Scattering (MS) and Stopping Power (SP) are modified as a function of time and space variation of the temperature and ionization degree of the compressed target. This analysis shows that in the low proton energy regime (Ep<10 MeV) the expected simple correspondence between layer position and protons time-energy foils, forcing us to a more careful analysis. Finally a detailed comparison with simulations from the 2D hydrodynamical CHIC code [115,116] has been done.

6.7.1 Analytical details

Proton radiography was used together with hard X-ray radiography to record the implosion history of the cylindrical target. Simulations were performed in Monte Carlo (MC) MCNPX Code [117] using 2D Hydro-dynamical CHIC code [115,116] density profiles of the imploded cylinder. Laser based protons are characterised by

small source, high degree of collimation and short duration. The multi energetic proton spectrum also allows probing the implosion at different times in a single shot, thanks to the difference in time of flights for protons at different energies. This is a clear advantage over other kind of diagnostic (e.g. hard X-ray) which require several shots in order to reveal complete implosion history. Another advantage of using proton radiography is a simple experimental setup keeping the imploding cylinder between the proton target and the proton detector on the same axis whereas X-ray radiography needs complex geometry and crystal collimator and detector alignment). Proton radiography using laser-generated protons has already been used in an experiment at RAL [118] to probe the implosion of a spherical shell. However in [118] the authors did not take in to account or oversimplify same important physical effects which are:

1) The MS effects which becomes important at relative low proton energy (<10 MeV) regime.

2) The temperature and density variation from warm-dense matter (compressed cylinder) to cold-dense matter (uncompressed part of the cylinder) till to warm-low density matter (plasma corona) that must be described each by different stopping power formula.

3) The energy loss by protons passing through the compressed target which lead to a time mixing and image superposition due to different energy deposition in each layer.

In this letter we will show the correct physical interpretation of the proton radiography at low energy regime proposing a standard procedure in order to obtain a complete simulation of the compression history. In addition, let's notice that from the experimental point of view, we could compare proton radiography results with those obtained by other diagnostic (hard X-ray radiography, X-ray pin-hole camera, X-ray crystal images) allowing to better understand the performance as well as the limitation of proton diagnostic

6.8 Experimental Setup

The experiment was carried out at Vulcan facility using the 100TW, 10 ps laser pulse coupled to 4 long-pulse laser beams driving the implosion of the cylinder. The beams (~ 4×50 J in 1 ns) at 0.53 μm, were focused at ~150/160 μm FWHM circular focal spots as shown in fig 1. Short pulse beams (SP) (100-150 J in 1ps) was focussed as a

backlighter source by an F=3.5 off axis parabola with a focal spot 10μm at FWHM with a peak irradiance of 1.5×10^{19} W/cm^2 to produce protons for radiography. Another 10ps beam was focused on a 25μm Titanium foil providing source for hard X-ray radiography working at hυ=4.5KeV.
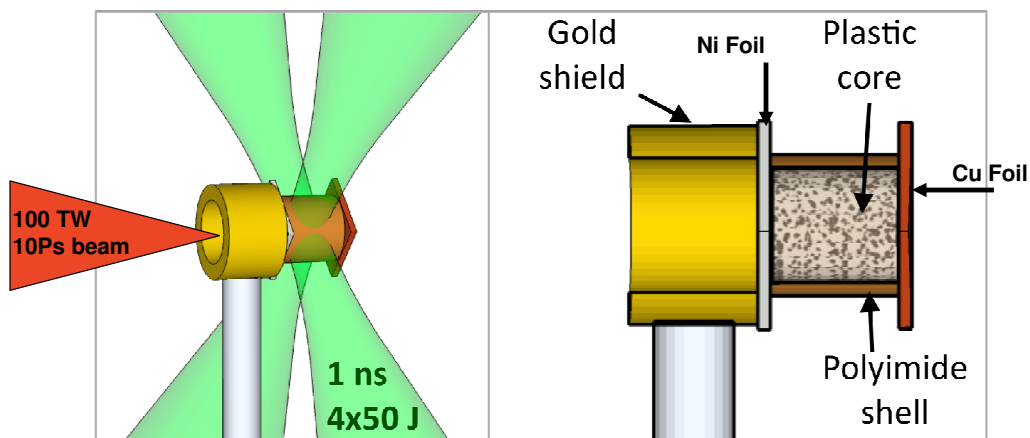

Figure 6.5: Schematic of the 4 compression beams (each of 1ns) focussed on the plastic cylinder. Also shows the 100TW beam (not used in the first phase of the experiment) propagating along the direction of the cylinder axis (b) Geometry and composition of cylindrical target, left side is the gold shielding cylinder and right side is the plastic cylinder filled with low density foam

The 200μm long polyimide cylindrical tube with 220μm outer diameter and 20μm wall thickness was filled with foam (acrylate) at density 0.1 g/cc. One side was closed with a Cu foil and the other with a Ni foil, respectively providing a tracer layer for diagnostics and the source for fast electrons. The Ni foil side was also shielded with a gold cylinder as shown in figure 6.5. The four LP beams timing was set so that they hit the target at the same time with precision of ± 50ps.

A second short pulse beam (SP) (100-150 J in 1ps) was focussed, as a backlighter source, on a 20μm thick gold foil, by an F=3.5 off axis parabola with a focal spot 10μm at FWHM giving a peak irradiance of 1.5×10^{19} W/cm^2 to produce protons with an approximated exponential spectrum with high energy cut off of about 10MeV.

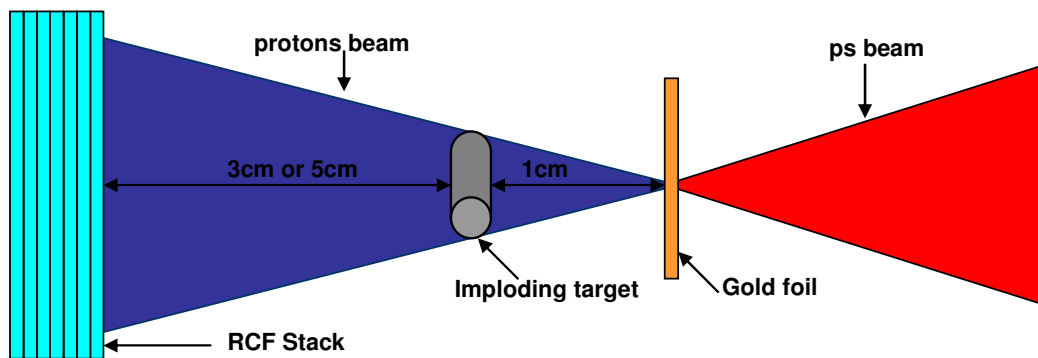The delay, τ, between LP and SP was adjustable between 0 and 3.6ns. The schematic is shown in fig.6.5.

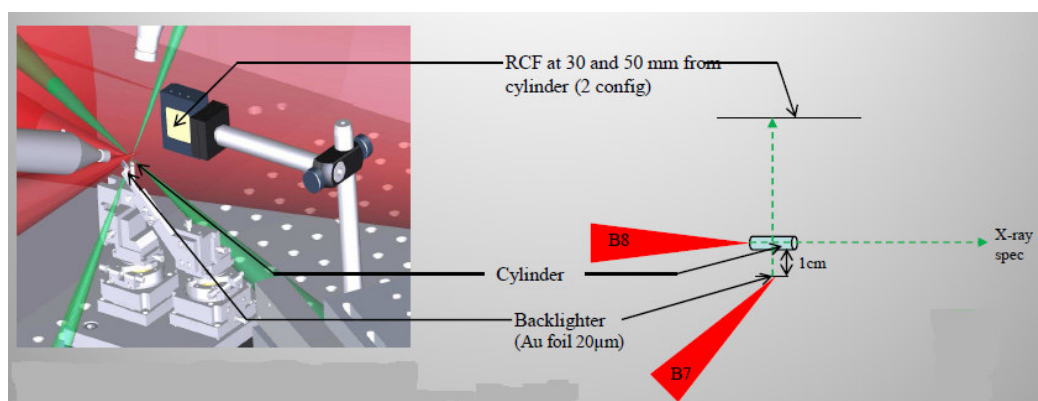*Figure 6.6 . **Schematic of proton Radiography Setup***

Figure 6.7: It shows the position of RCF stack holder inside the target chamber at 30 and 50 mm from the cylinder, Beam 7 was used to hit the gold foil for generating protons and beam 8 was used for X-ray spectroscopy which is not part of this thesis.

The proton detector used in this experiment consisted of a multilayer film pack containing spatially resolving radiochromic (RCF) dosimetry film (types: MD-55 and HD- 810) as shown in figure 6.6 and 6.7. This arrangement, which has been extensively used in laser-driven proton acceleration experiments, gave a diagnostic in which each layer was filtered by the preceding layer, giving a series of images per shot as shown in the figure 6.8, each corresponding to a different proton energy and hence a different probing time [119]. The first layer, HD1 was shielded with an aluminium foil of 12 micron. In some shots we could see the debris of aluminium foil on the first layer (HD1) of the RCF stack. This is also shown in the figure 6.8.
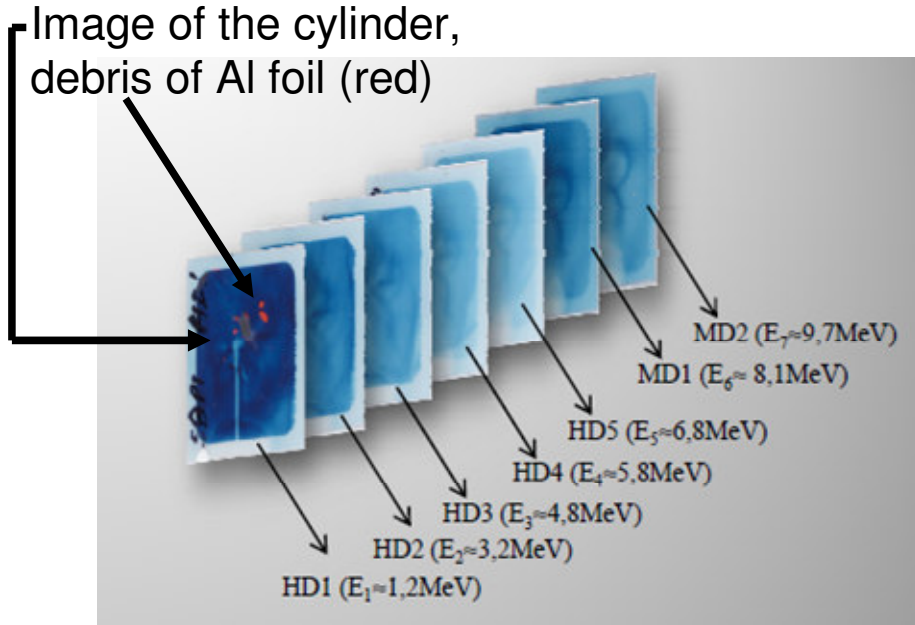
Figure 6.8 shows the two types of RCF ,HD 810 and MD 55, in a sequence.The first five layers are HDs and the last two layers are MDs. Image of the cylinder is sown on the first RCF layer and debris of Al foil(red) can also be seen on HD1,as it was shielded with a 12micron Al foil.
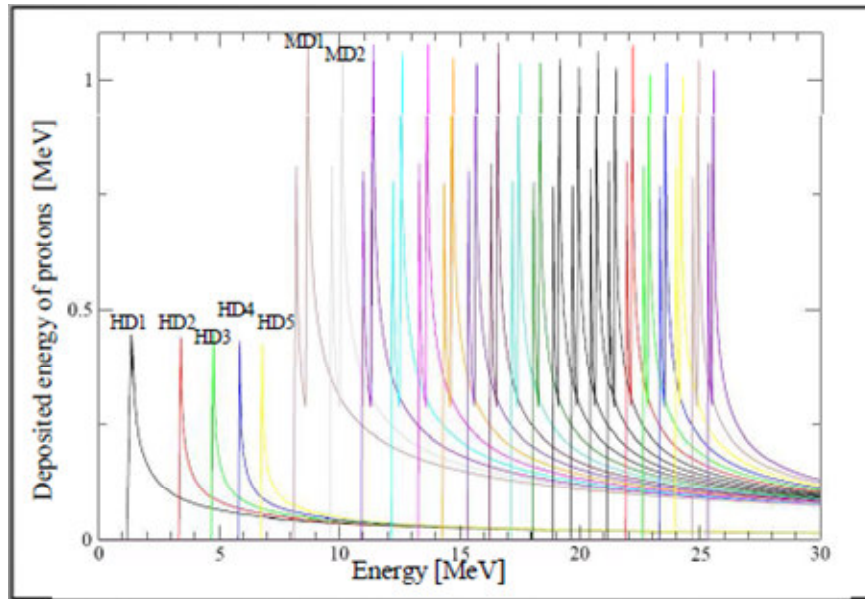

Figure 6.9 shows the energy deposited by protons in the Braag Peaks on each layer of RCF in the given configuration as shown in the above figure

This arrangement, which has been extensively used in laser-driven proton acceleration experiments, allows obtaining spatially resolved images of the imploding cylinder which is based on the fact that the proton spectrum is continuous in energy. Therefore

on one side protons of different energies have different velocities and hence probe the imploding cylinder at different times. On the other side protons preferentially deposit their energy at a given depth (corresponding to their Bragg peak) and hence a given RCF layer provides an image roughly corresponding to a given probing time. In our case the time resolution corresponding to difference in Bragg Peak energy between two successive layers was a few ps. However we will see later how this "simple" picture which relies one RCF layer to one time fails, at least partially, in our case.

In our experimental set up the geometrical magnification was M=4.5 allowing a spatial resolution less then 1 µm. We typically got 7 impressed RCF layers per shot covering a full time span of 400 ps, therefore we could not follow all the target implosion in one shot, which imply the need to change the delay between SP and LP and reconstruct the full implosion with different laser shots (typically 3).

6.9 Results and Analytical Techniques

The obtained images of RCF are scanned with Nikon 4.0 scanner. The optical resolution of the Nikon scanner is 4000 dpi (e.g. ~6.5 µm). The images are then opened in a stack of red, blue and Green channels. The red channels because of their best resolutions were selected to further analyse the density profiles of the compressed cylinders. The directly exposed radiographs and their red channels are showing the reference cylinder and different stages of the compressions in figure 6.10. The minimum observed diameter is ~140µm.
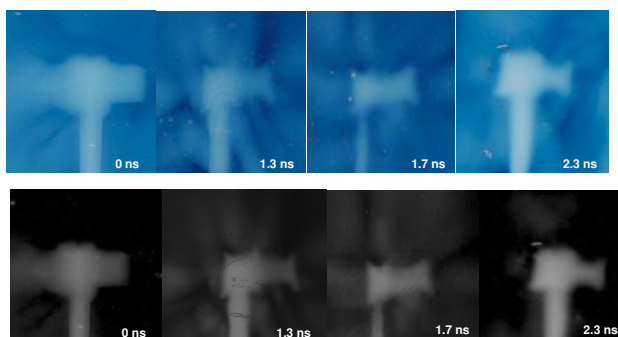

Figure 6.10 shows the directly exposed radiographs in blue colour, as protons polymerises the material of RCF which turns blue progressively, the absorbed dose can be determined by the optical density of the exposed area. The black ones are the red channels of the same radiographs.

The scanned radiographs and their red channels were analysed using imagj and Kaliedagraph softwares. During the analysis it was seen that the profile of the uncompressed reference cylinder and less compressed cylinders could be fitted with "supergaussian" shape, while the finely compressed plastic cylinders were fitted with "gaussian" shape. It has been noticed starting from the reference cylinder, each progressive compression is being shifted from super Gaussian to Gaussian shape, e.g. at t=0ns the uncompressed cylinder fits with superguassian shape by substituting n=6 in the Gaussian formula, we see the minimum compression at t=1.2ns - 1.5ns and these profiles fit with supergaussian shape by substituting n=4 in Gaussian formula, it is shown in figure 6.11.
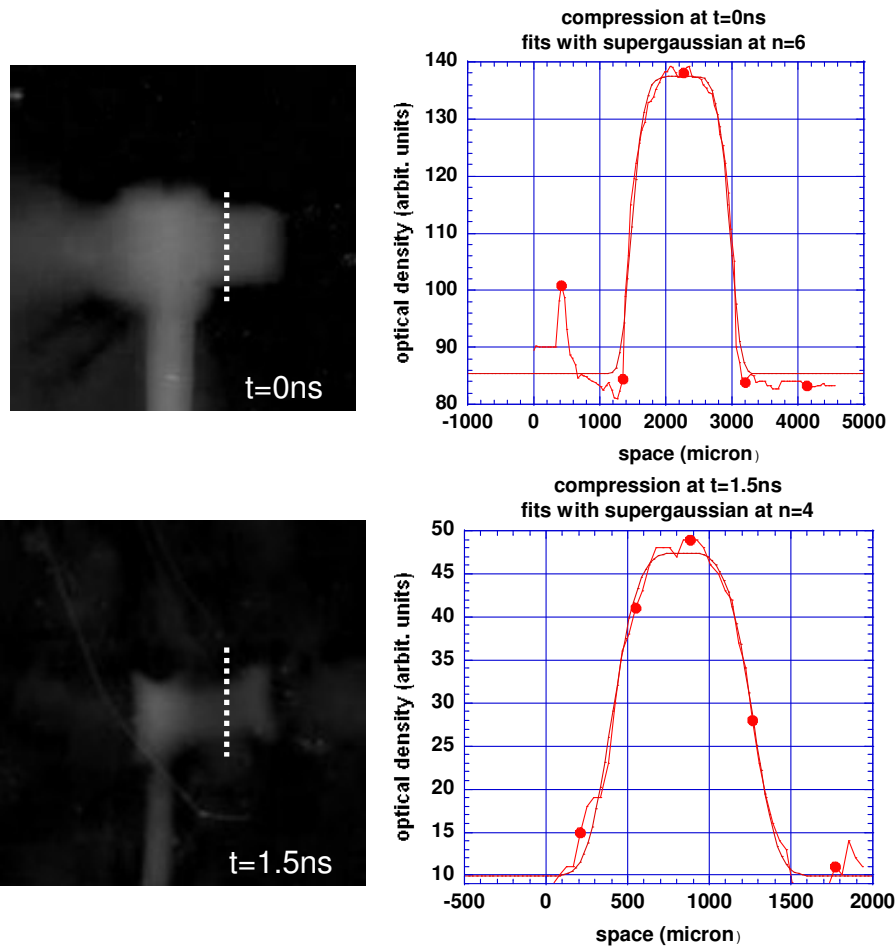
Figure 6.11 shows the profile of uncompressed cylinder at t=0ns and minimum compression at t=1.5ns, both fit with supergaussian shape.

136

Whereas at t= 1.6ns - 2.3ns, the compressions are being fit with perfect guassian shape. This is shown in figure 6.12.

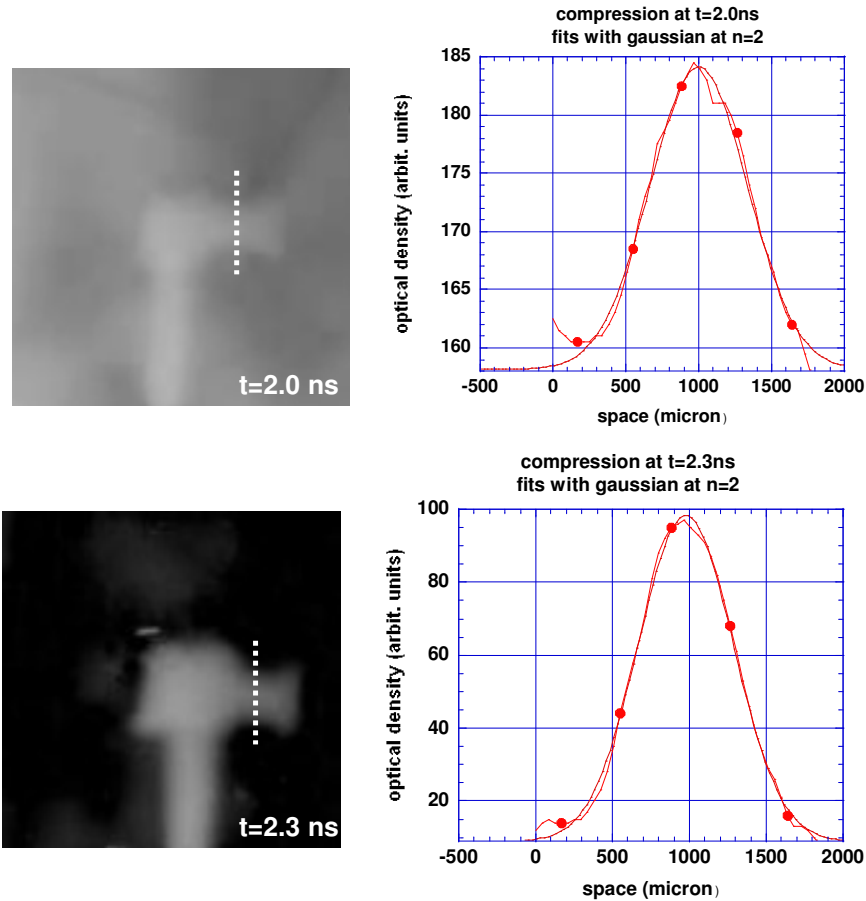*Figure 6.12 shows the profile of compressed cylinder at t=2.0ns and maximum compression at t=2.3ns,both fit with gaussian shape.*

The experimental data history of proton radiography is shown in a table on the following page. The cylinder was radiographed with protons in 4 laser shots. Shot 9 was taken at delay time=0.9ns between SP and LP, giving a scan over a time between ~1.1-1.6ns. The τ, is the time in which protons of given energy probe the dense core or plasma. This is given below in an empirical formula:

$$\tau = \text{Delay} + \text{Time of Flight (TOF)}$$

Experimental compression data of the cylindrical targets obtained from proton radiography at different time delays in different laser shots.

Shot numbers	Time of flight + Delay b/w LP and SP (ns)	Diameter (micron/magnification)
Reference Shot		
HD1	0.0	~ 220
HD2	0.0	~ 220
HD3	0.0	~ 220
Shot 3		
HD1	2.3	147
HD2	2.1	154
HD3	2.0	163
Shot 4		
HD1	2.3	159
HD2	2.1	160
HD3	2.0	163
Shot 5		
HD1	1.96	147
HD2	1.70	165
HD3	1.63	172
HD4	1.6	169
HD5	1.57	177
MD1	1.55	184
MD2	1.53	189
Shot 9		
HD1	1.56	163
HD2	1.30	185
HD3	1.23	186
HD4	1.20	195
HD5	1.17	200
MD1	1.15	198
MD2	1.13	179

Table 6.1

Where $$\text{TOF} = \frac{d}{v} = \frac{d}{\sqrt{\dfrac{2E_p}{m_p}}}$$

Where d is the distance between the proton source and the cylindrical target, E_p is proton energy and m_p is the mass of proton, where $\tau = 0$, the beginning time of the ns beams interaction with the plastic cylinder and the duration of each compression laser beam is 1ns as is mentioned above in the experimental setup. The laser shot 5 was taken at delay time 1.3ns which covers the range ~1.5-2.0ns. The analysis of the laser shots 9 and 5 shows that the shock starts penetrating at ~ 1.5ns as a reaction of the ablation of plastic shell and hence cylindrical compression starts establishing after ~1.5ns, and we don't see much difference in the initial diameter of the cylinder and the compressions obtained at 1.1-1.5ns, which could be an evidence of the supergaussian fits of uncompressed cylindrical profiles and the compressed cylindrical profiles at the time range between 1.1-1.5ns implies the minimum compression in this time scan.

The laser shots 3 and 4, both are taken at the delay time= 1.7ns giving the compression history between 2.0-2.3ns. So the analysis of shots 3 and 4 leads us to the fact that the maximum compression is observed in shots 3 and 4, the compression at 2.3ns in shot number 3 is ~147µm, whereas in shot number 4 the maximum compression obtained at 2.3ns is ~158µm. Shot 4 does not show any difference in compressions at 2.0 and 2.1ns, instead showing invariance in compressions. Whereas shot number 3 is showing a increasing trend in the compressions from 2.1 to 2.3ns It has been assumed that this difference could be due to the couple of factors, 1) the fluctuations in laser energy 2) the misalignments of the ns beam which is why we may not have all the laser energy on the target. The misalignments of the ns beams were monitored from the results obtained with the pinhole camera (PHC). It will be discussed and shown in the following sections in more details; the shot number 4 is the victim of misalignments of ns beams (which will be show in figure in the following section of PHC). According to the 2D-hydrodynamical CHIC code simulations the stagnation time for the plastic cylinder filled with 0.1g/cc foam is predicted at ~ 2.2ns, and the same is evident from our experimental analysis, so we can say that we have been successful in reproducing the stagnation time correctly as predicted from 2D-hydro CHIC simulation which is shown in figure 6.13.

Ablation of plastic shell and expanding plasma,

Shock wave starts penetrating the plastic cylinder after about 1.5ns, and the stagnation time seems to be ~2.2 ns
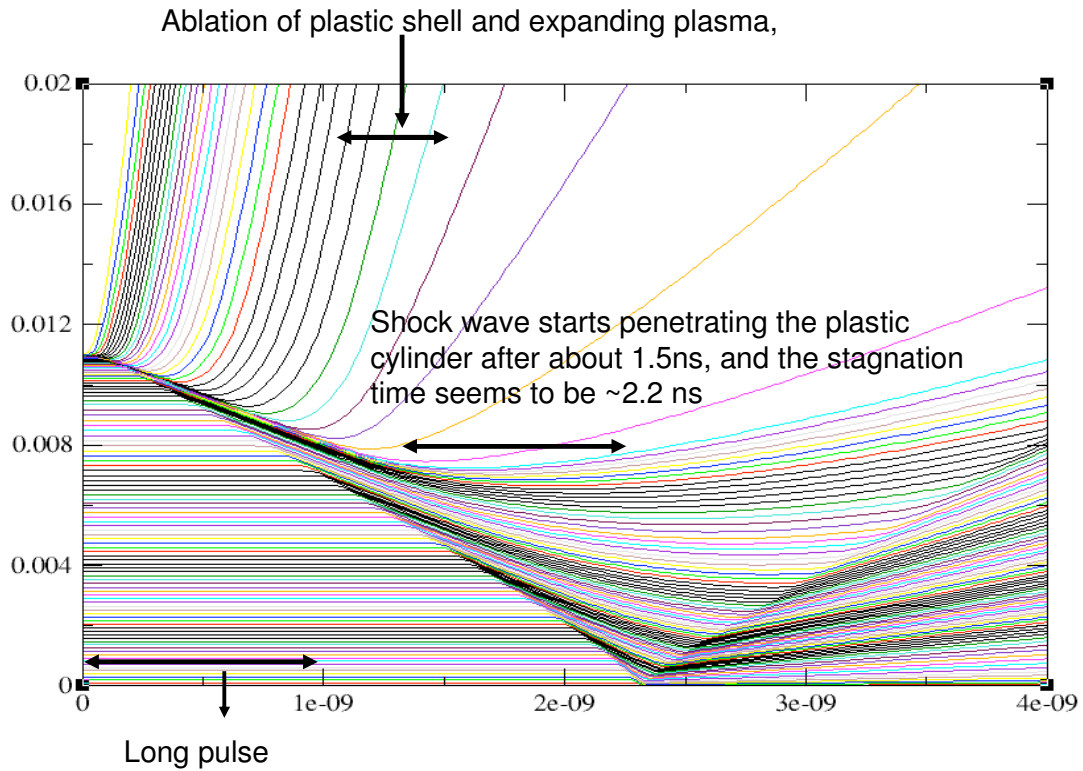
Long pulse

Figure 6.13 shows 2D-hydro CHIC code simulation for the plastic cylinder filled with 0.1g/cc foam, it shows that shock starts travelling at about ~1.5ns and compression is being established after ~1.5 ns. The stagnation time is 2.2ns for the foam density 0.1g/cc. The time on x-axis is in ps and the radii on y-axis is in cm

The implosion graph of the plastic cylinder filled with 0.1g/cc foam comprises the 4 shots discussed above in details is shown in figure 6.14. The results obtained from the 4 laser shots are plotted together on the same graph which shows increasing trend of the plastic cylinder compression from 0-2.3 ns. The diameter of the uncompressed cylinder is shown at 0ns and the maximum compression obtained ~ 147μm is shown at 2.3ns. Because of the laser energy fluctuations and the laser beam misalignments we can assume the stagnation time as ~ 2.2ns which is also evident from 2D-hydro simulation as shown in the figure above.
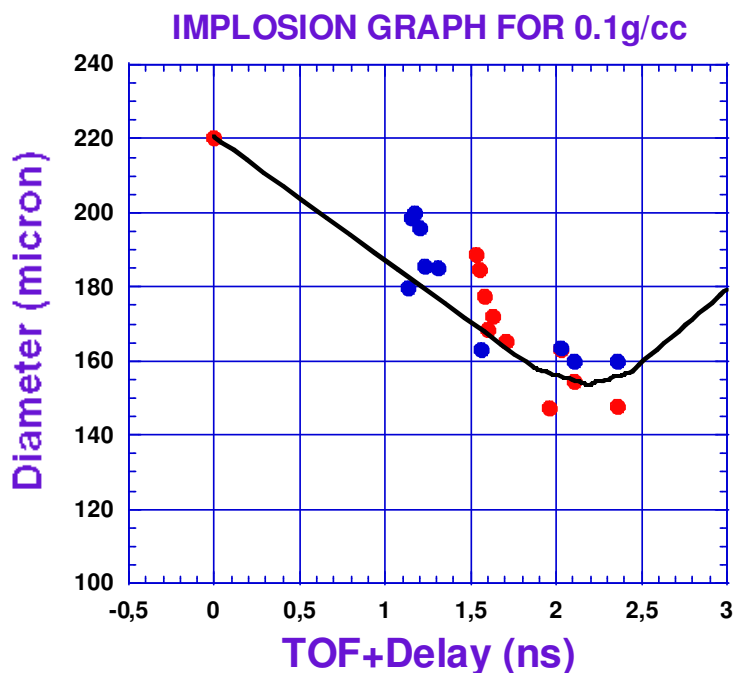
Figure 6.14 shows the implosion history of the plastic cylinder obtained at different time delays, it shows the beauty of the increasing compression of the plastic cylinder, the red dot at 0ns shows the uncompressed diameter. The top blue and red dots from 1.1-1.96ns show the results of the shots 9 and 5 respectively, whereas the below red and blue dots from 2.0-2.3ns show the maximum compression and the stagnation time in the twin shots 3 and 4 respectively. The little difference in the diameters obtained in the twin shots is assumed to be because of the fluctuation in laser energy and misalignment of the ns beams in the shot 4. The black curve is free hand drawing just to beautify the compression trend.

The implosion trend can also be visualised in the following densitometries along the minimum diameters, which is shown in the figure 6.15.

The proton radiography results were also compared with the results obtained from PHC and the x-ray radiography for the pointing of the ns laser beam alignments and the evolution of the imploding cylinder respectively. In the following sections, the proton radiography vs PHC and x-ray radiography will be discussed in details and the comparison of their results will be discussed analytically and the problems will be highlighted.
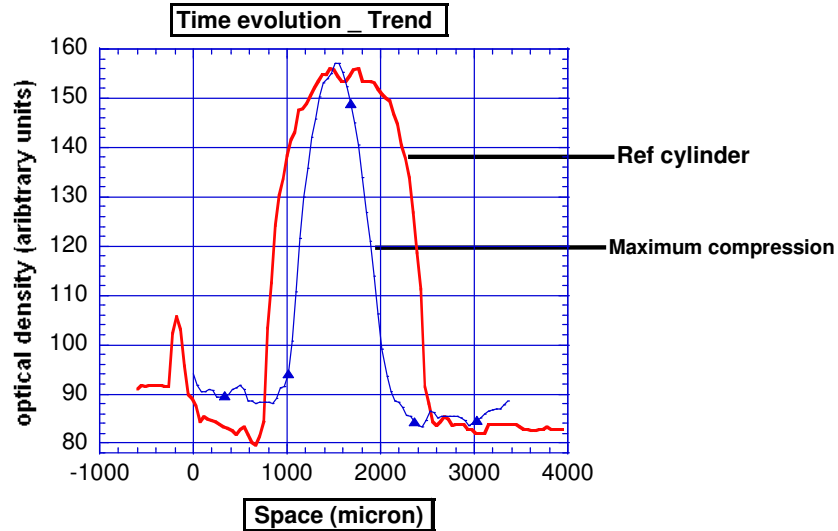
Figure 6.15 shows the densitometries along the minimum diameters. The uncompressed plastic cylinder could be fitted with supergaussian (red) while the compressed cylinder (blue) fits with gaussian shape.

6.9.1 Proton radiography VS PHC

Alignments of the ns beams were also crucial for the success of the experiment. An x-ray pinhole camera (PHC) was used to look at the interaction area allowing monitoring of beam alignments. The PHC was set at 90° to the cylindrical axis from the top. The PH array was set 13cm away from TCC (Target chamber centre) and 123cm from the image plate (detector for x-ray emission). Thus magnification was 9.46. The image plate was shielded with a filter of 24µm aluminium mylar which sees energies greater than 3KeV. The schematic of PHC is shown in the figure 6.16.
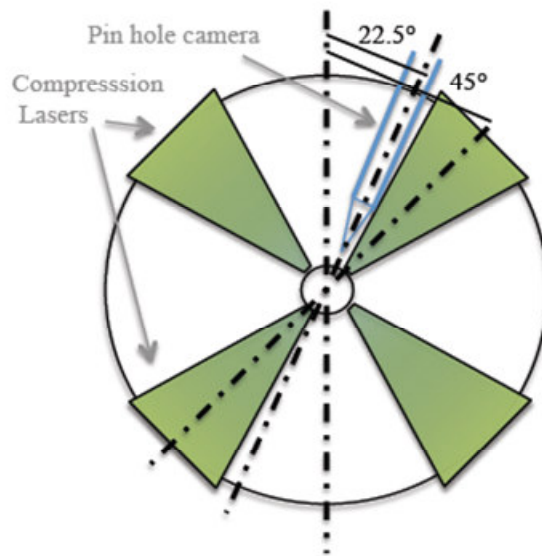
Figure 6.16 shows the schematic of PHC that is set perpendicular to the cylindrical axis at 22.5° from the normal.

Figure 6.17 shows the image obtained with PHC superimposed with an exact cross section of the real cylindrical target.
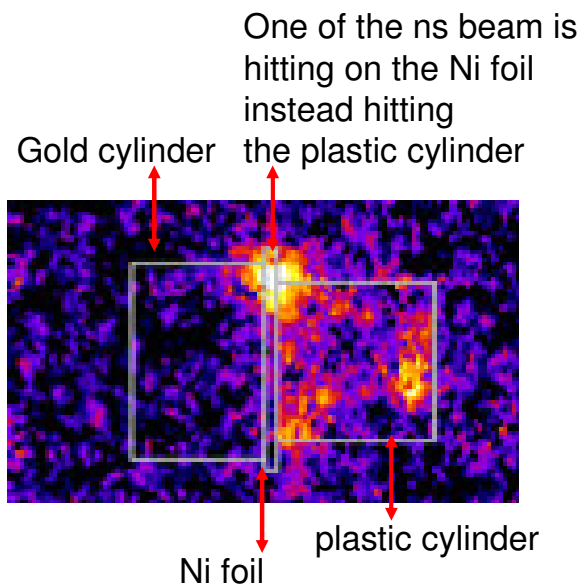

Figure 6.17 shows the image taken from PHC superimposed with cylinder. In this image of the 4 ns beams was hitting the Ni foil rather the plastic cylinder, pointing to beam misalignment.

The PHC diagnostic was though simpler but it was very helpful to point out the misalignments of ns beams onto the plastic cylinder, e.g. a proton radiograph obtained in one shot is shown in figure 6.18 with a curve on gold cylinder which shows that one of the ns beams was hitting the gold cylinder instead the plastic. The PHC image taken during the same shot is an evidence of this misalignment.
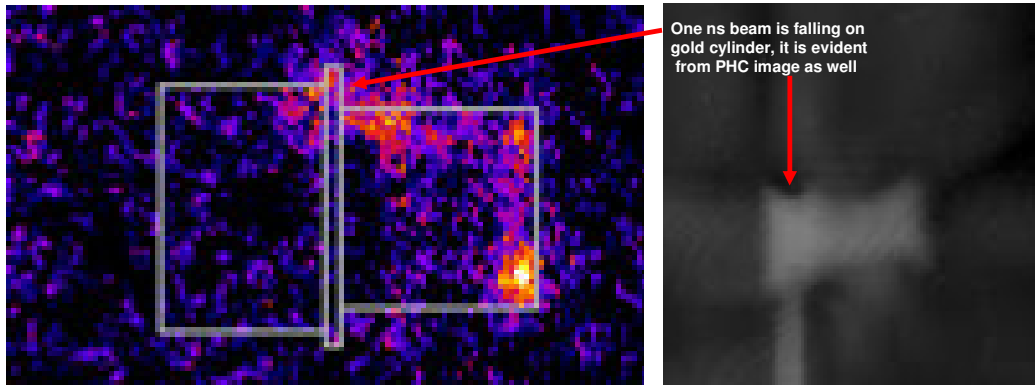

Figure 6.18 shows proton radiograph (right) and PHC image (left) taken in the same shot, one of the ns laser beam misalignment can be seen from the curve on the gold cylinder in the radiograph which is also evident from the PHC image.

So the results from PH-array indicate that pointing was not very well achieved for every shot, which is why we might did not have all laser energy on the target. This could lead to less compression than expected.

6.9.2 Proton Radiography VS X-ray Radiography

Moreover the proton radiography results were compared with the results obtained from x-ray radiography as well. The x-ray radiography was achieved by focussing a 100TW, 10ps (160 J with peak irradiance $5x10^{18}$w/cm^2) laser beam on a 25µm thick Ti foil with a circular focal spot of 20µm at FWHM. The emitted x-rays passed through the cylindrical target and reflected from a spherically bent quartz crystal, with 2d=2.749Å, Rc = 380mm, onto the image plate (IP, x-ray emission detector). The distance between the backlighter and the target was ~ 1cm, and the distance between the target and the crystal was ~20cm as shown in figure 6.19. Thus we got a magnification of 10. The crystal was shielded with 10 micron polypropylene and the IP was shielded with 10µm polypropylene plus 10µm Ti foil. So it could see the

emission > 4KeV. The x-ray radiography schematic is shown in the figure below. The delay range between the LP and Sp time was from 1.7-3.2ns.
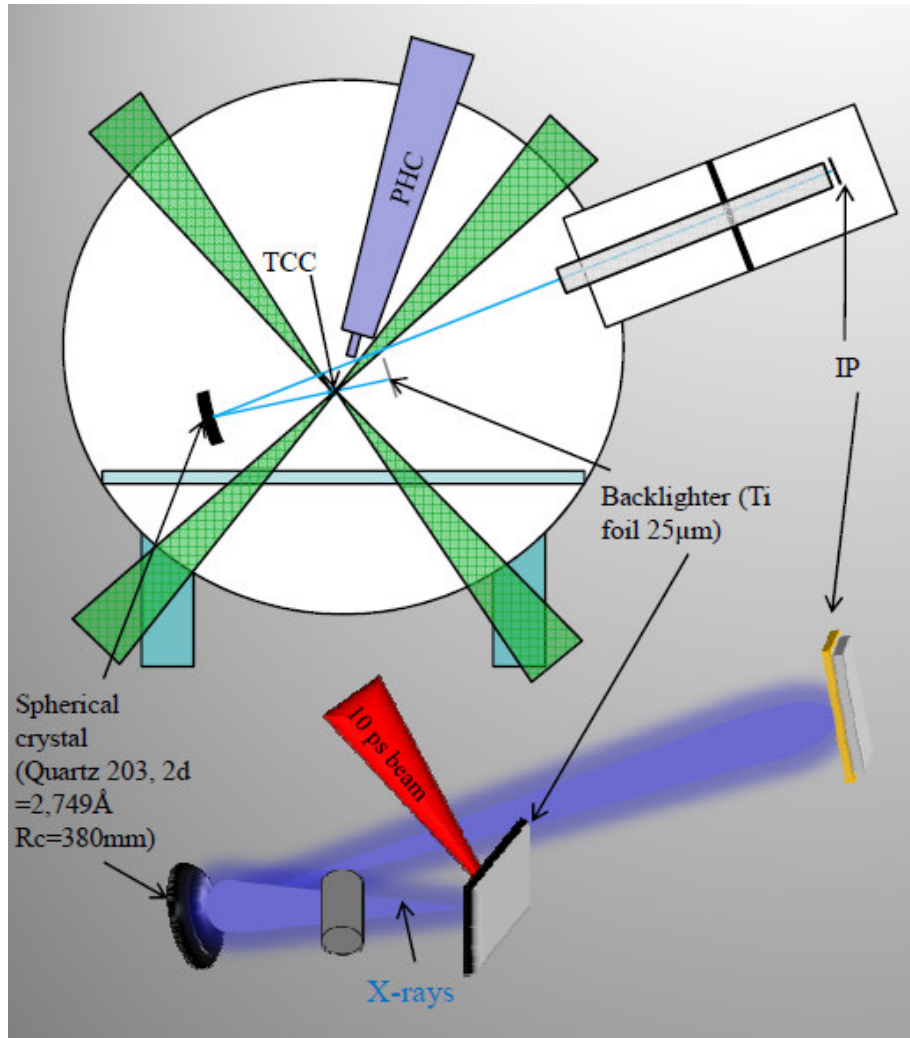

Figure 6.19 shows the schematic of the X-ray radiography setup.

The results obtained from the x-ray radiography for the plastic cylinder filled with 0.1g/cc and 1g/cc of foam were analysed. The results obtained from x-ray radiographs are shown in the figures below both for 0.1g/cc and 1g/cc foam.

The figures 6.20 and 6.21 show the compressions for the plastic cylinder filled with 1g/cc foam taken at different time delays from 1.7-2.7ns. It has been realized that at 3.2ns the x-ray radiograph was showing expansion and the maximum compression observed is ~70 micron at 2.7ns. Thus we could say that the stagnation time for the foam density at 1g/cc is rather between 2.8-3.0ns.

Unfortunately we could have only two laser shots for the cylinder filled with foam at 0.1g/cc. Due to plenty of running diagnostics during this huge experimental campaign, we could not afford very long laser time for only one diagnostic. But we were fortunate to obtain results from the two successful laser shots taken at two different time delays at 2.2 and 3.2ns. The compressions obtained at foam density 0.1g/cc is shown in the figure 6.22
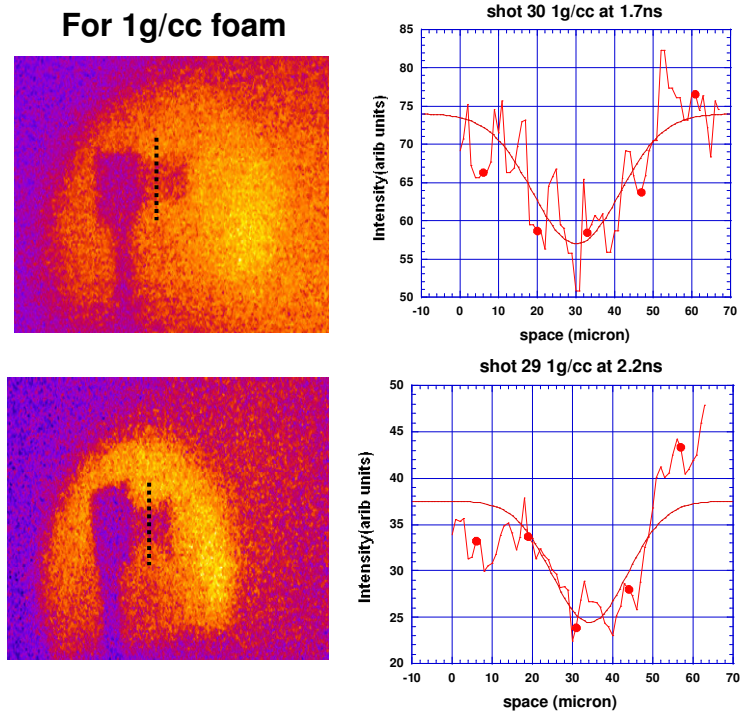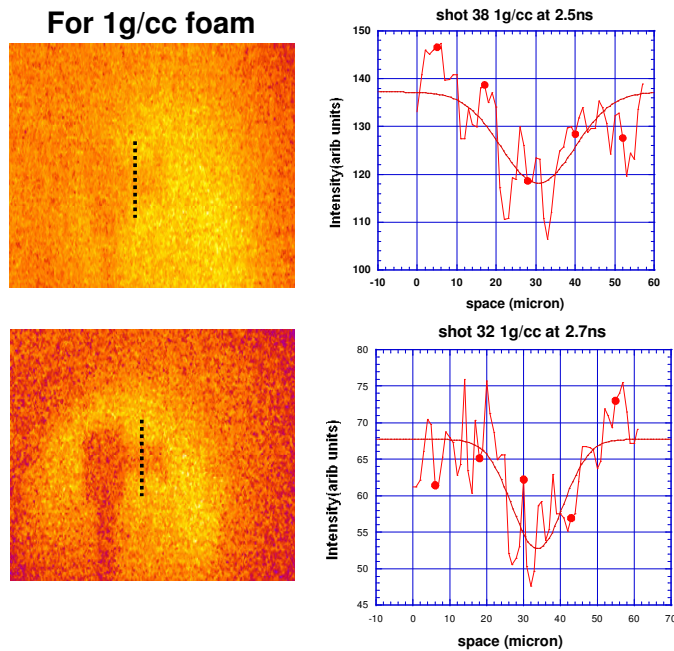

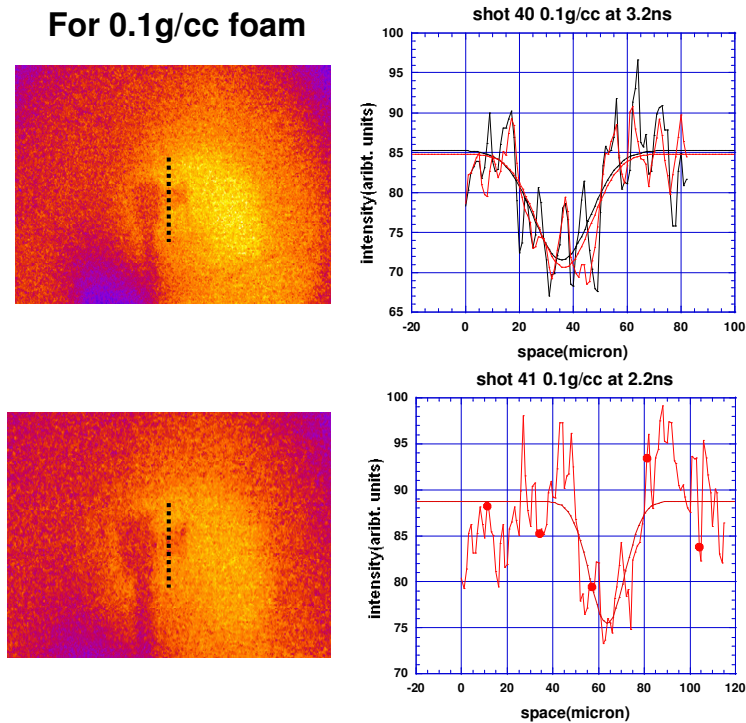Figure 20

For 1g/cc foam

Figure 21

Figures 20 and 21 show the compressions obtained at different time delays between LP and Sp for the plastic cylinder filled with foam at density 1g/cc. The maximum compression was observed at 2.7ns. The maximum compression observed is ~70µm for 1g/cc foam.

For 0.1g/cc foam

Figure 22 shows the compression obtained at 2.2ns in shot 41, whereas the expansion is observed at 3.2ns in shot 40, The shot 40 is showing different curves of the same image at two slightly different positions.

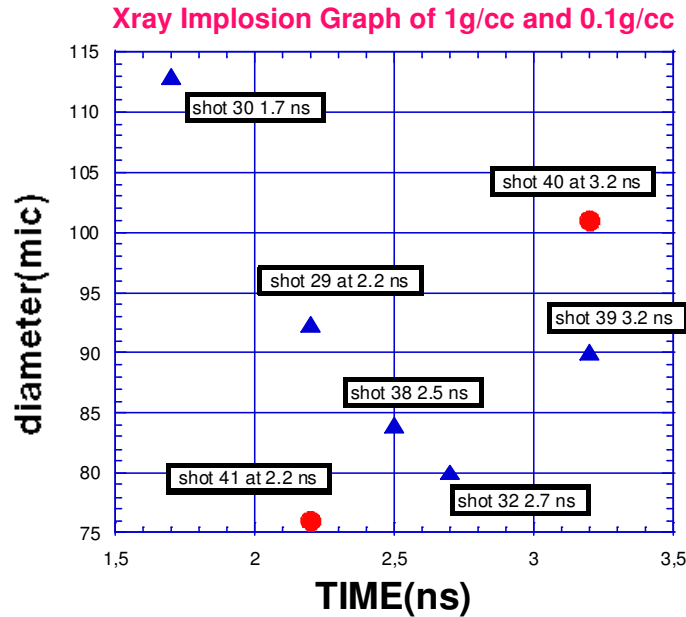**Xray Implosion Graph of 1g/cc and 0.1g/cc**

Figure 23, it shows the implosion history of the 0.1g/cc and 1g/cc foam density of the plastic cylinder. The blue triangle are showing a compression trend until 2.7ns and at 3.2ns it shows the expansion for 1g/cc. The red dot at 2.2ns shows the maximum compression obtained at 0.1g/cc and again at 3.2ns it shows an expansion trend.

The implosion history of the x-ray radiography is shown in figure 6.23. The blue triangles are showing the compression trend for the foam density at 1g/cc, whereas the red dots are showing the maximum compression at 2.2ns for the foam density at 0.1g/cc and the expansion for both densities has been observed at 3.2ns which is clearly shown in the implosion graph above in figure 6.23

.

The main objective to analyse all these x-ray data history was to see whether x-rays penetrate the same depths of the given cylinders as protons do. But it was very interesting to see that x-ray data analysis shows more penetration than that of protons. The comparison of proton and x-ray data is shown below in figures 6.24. The figure shows the comparison of the proton radiography and the x-ray radiography for the foam density at 1g/cc. In this figure, the top blue radiographs are the RCF layers

exposed to protons in different times in proton radiography shots for 1g/cc foam density, whereas in the same figure the bottom images are the obtained x-ray radiographs for the foam density at 1g/cc.
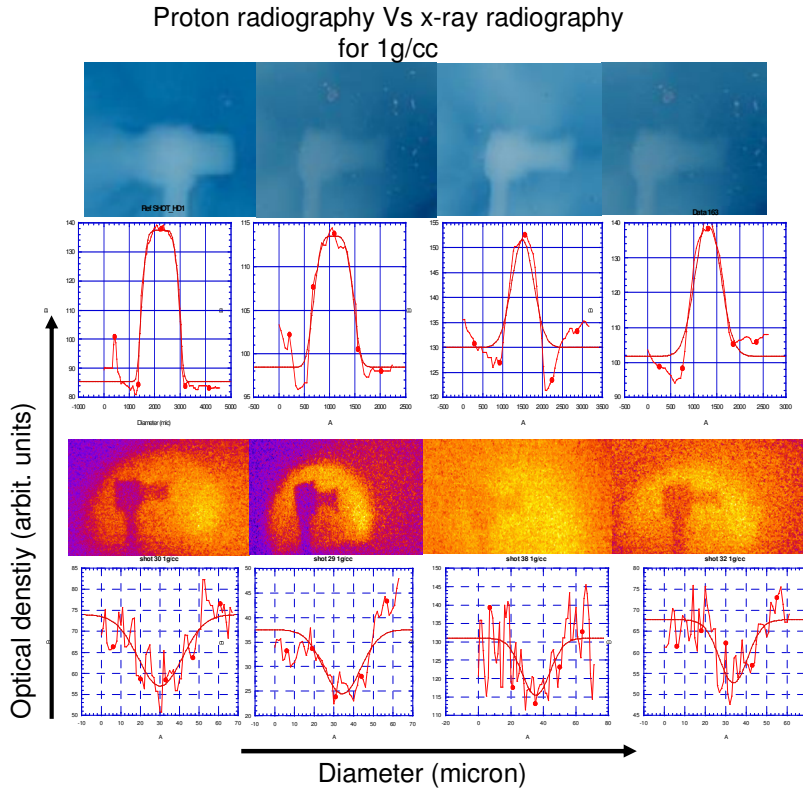

Figure 6.24, it shows the compression obtained at the foam density 1g/cc.The top radiographs are taken from proton radiography and below the radiographs the compression profiles are shown in the graphics. The lower red and blue radiographs are obtained from X-ray emission and the profiles of their compressions are shown in the graphs below the images of the radiographs.

Figure 6.25 shows the comparison the proton and x-ray radiography for the plastic cylinder filled with foam at density 0.1g/cc. In this figure (?), the black and white radiograph is the obtained red channel of the RCF layer at ~2.2ns,wheras the right side image is obtained from x-ray emission at the same delay of time. Their density profiles are extracted using graphic program and are shown in the figure beneath the respective radiographs. The same technique was used to analyse the x-ray data as that was used for proton radiography data analysis. So here we noticed that the maximum compression obtained in proton radiography is ~147µm, whereas the maximum compression obtained in x-ray radiography is ~85µm.
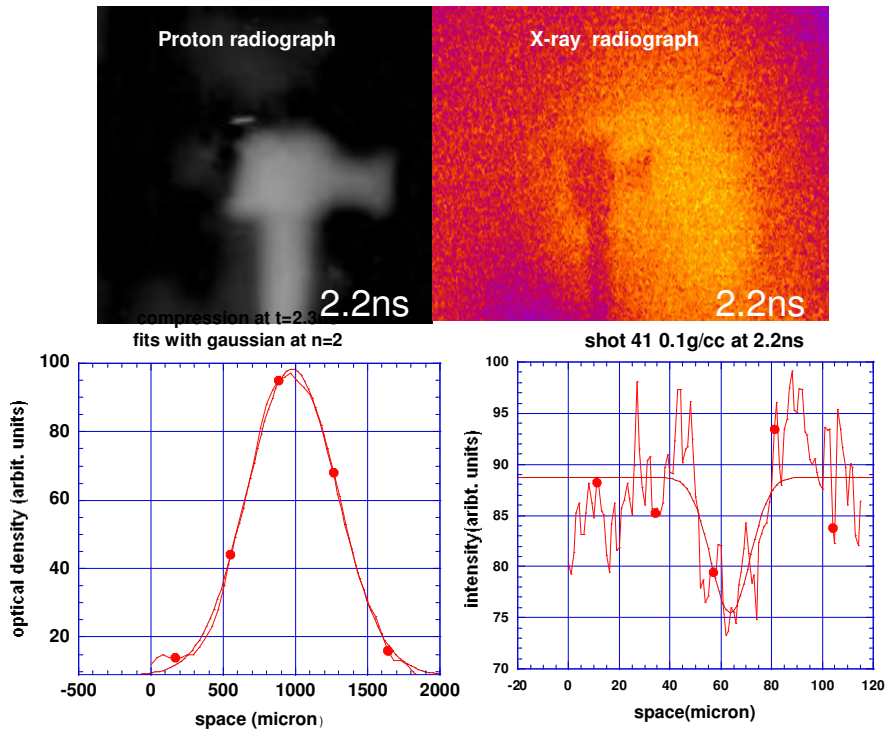
Figure 6.25, the left side of the figure shows the results from proton radiography at delay 2.2ns, whereas the right side of the figure shows the results obtained from the x-ray radiography at the same delay. Their compression profiles are shown in the graphics.

The implosion history obtained from the two diagnostics is shown in the graph in figure 6.26.
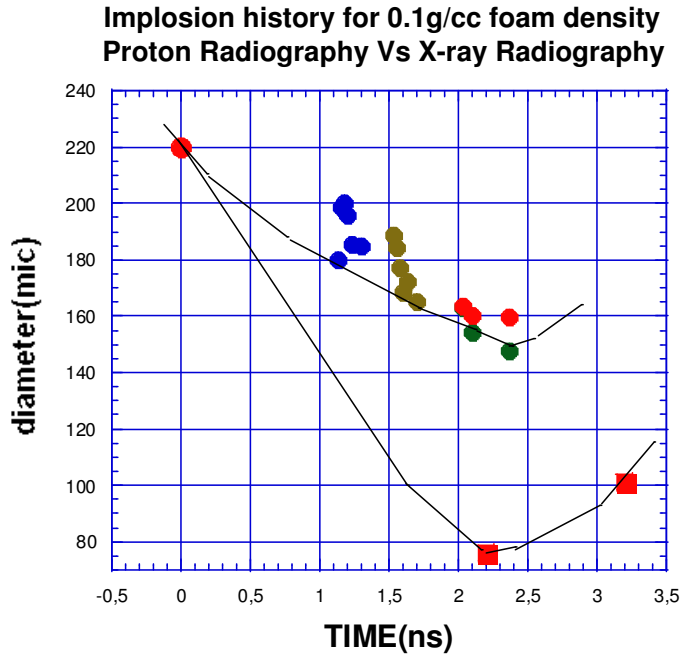
Figure 6.26, this shows the imploding trend obtained from the two diagnostics .The reference is shown at 0ns. The red and pink dots are proton radiography results whereas the gray dots are the results from x-ray radiography which are showing ultimately more compression than that of protons.

Finally, the obtained peak densities from the two diagnostics were compared with 2D-hydro CHIC simulations, as shown below in figure 6.27. It was noticed that the stagnation time from both diagnostics was reproduced correctly as was predicted from 2D-hydro simulations. It is also shown in the same figure that the x-rays are more penetrating than protons. The different colours of the curves in the 2D-hydro simulations are showing the density distribution of the cylinder at different times. Each time reveals a particular behaviour of the exploding and imploding phenomena of the plastic cylinder from 0-4ns depending upon the beginning of interaction of the heating LP laser beams at 0ns and the resulting shock propagation impact.
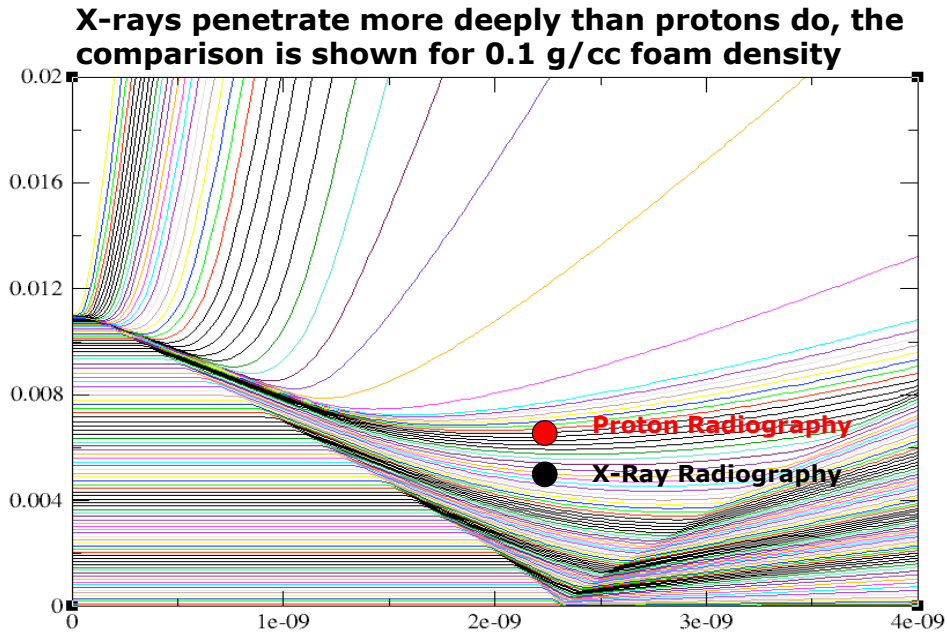
Figure 6.27, shows the comparison of x-ray and proton radiography with the 2D-hydro CHIC simulations. The stagnation time is 2.2ns for 0.1g/cc foam density is predicted in 2D-hydro simulations, the multi colours of the curves are indicating the different radii of the cylinder at different times after and before the impact of shock wave (obtained from 2D-hydro CHIC). The x-rays show more penetration than that of protons.

In order to investigate these physical effects we have run a "start to end" simulation of the process using MCNPX code developed at LANL. In this code the SP and MS effects are taken into account respectively with Bethe [9] and Rossi [10] theories. This facts will be discussed in more details in the following section.

6.10 MCNPX Code

MCNPX is a general-purpose Monte Carlo N-Particle code that can be used for neutron, photon, electron, protons and other particle transport that can be used for neutron, photon, electron, protons and other particle transport. The basic idea is to simulate every single particle 'history', following suitable physical laws under given probability distributions.

The user can interact with the code by the input file. This file is divided in three parts the first and the second parts are dedicated to the geometrical setting whereas the third part is dedicated to the source specifications, material specifications and tally (e.g. Output physical observable).

6.10.1 Outline of the simulation:

The code is able to reproduce the experimental set-up in all its relevant part which are:

The protons source (energy spectrum and divergence of isotropic point-source), the target (material composition, density profile, and geometry) and the detector (material composition) which is composed by different parallelepiped at different positions representing the different active layers.

The SP and MS effects are taken into account in the code respectively with Bethe [9] and Rossi [10] theories. Moreover the variation of temperature, density and ionization degree are taken into account modifying the original hydro density profile.

We assume a time sampling of hydro profiles (density temperature and ionization degree) obtained by CHIC code [114,115]. For each hydro time we run a MC simulations collecting the energy deposition (the measured optical density on active layer is proportional to energy deposited in it [120] in each parallelepiped (RCF layer). which form an image of the cylinder. Thanks to the above mentioned properties of protons, at each hydro time will correspond to a discrete proton energy. The full proton spectrum will be covered running different simulations changing hydro times (hydro profiles) then, we get a Matrix of mono-energetic, fixed time 2D images. Finally for each RCF layer we convolve the images at different time with the relative spectral probability. The resulting images can be compared with the experimental one. The simulated radiographs of reference cylinder at different stages of compressions are shown in the figure 6.28.
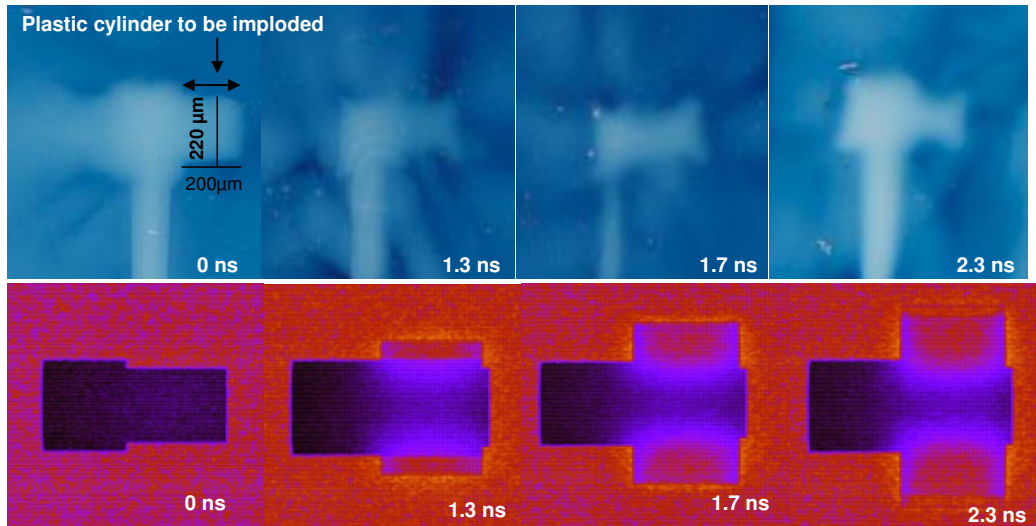
Figure 6.28: Compression history obtained by simulated proton radiographs at times t_1=0ns, t_2 = 1.3 ns t_3 = 1.7 ns t_4 = 2.4 ns. The top images are the experimental radiographs and the below ones are the synthetic images produced by MCNPX code at different stages of compression.

The code also takes into account multiple scattering and it observed after passing through the cylinder. It shows an increasing blur with the increase in the distance from the target as shown in the figure 6.30.

We could also interpret that the agreement between the profiles of experimental and simulated compressions is very good as shown in figure 6.31.
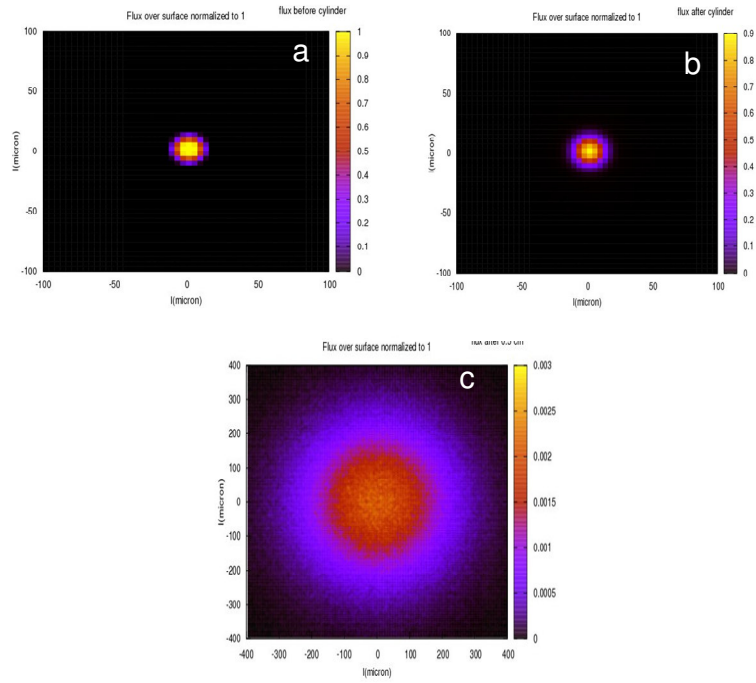
Figure 6.30: It shows increasing blurring as the protons go away from the cylinder. The image shown in "a" is taken just before the cylinder, whereas b and c are taken after the cylinder at 0.1 and 0.5cm respectively. Increase in blurring is observed after the cylinder.
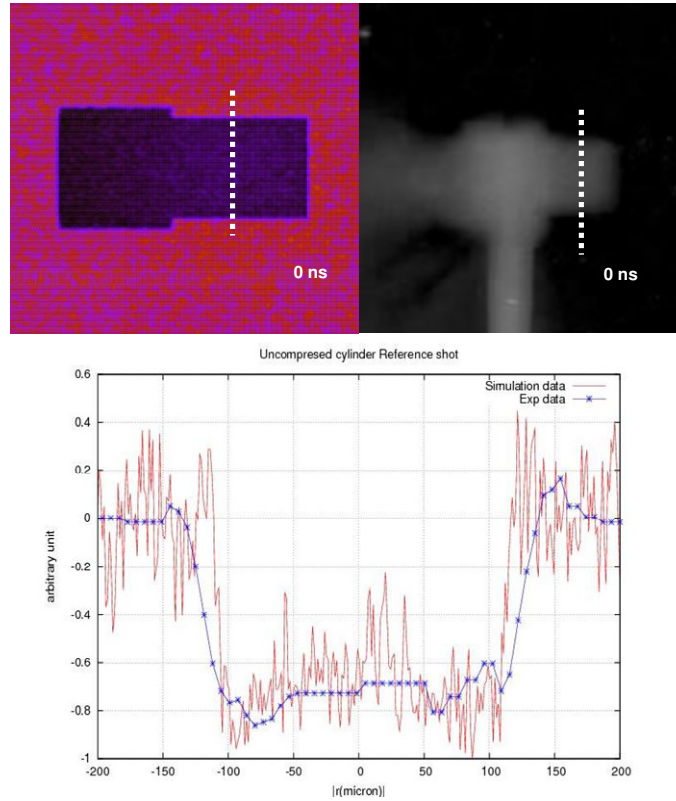
Figure 6.31: it shows the agreement between simulated and experimental uncompressed cylindrical profiles.

Moreover we have taken into account multiple energy contribution of protons on each RCF layer. The final measured image on each layer k,

$$I_k = \sum_{i=1}^{N_i} p_i I_{k,i}$$

is due to the convolution of mono-energetic image with initial spectral distribution of protons starting from RCF intensity measurements, where p_i is the relative probability in approximate discrete spectral energy distribution:

$$P(E) \sim \Delta E \sum_{i=1}^{N_i} P_i$$

The mono-energetic images are obtained by sampling the hydro times t_i and running one simulation for each layer "k" for each discrete energy contribution "i". On the other hand the mono-energetic images I_{ki} will be higher than the real size of cylinder

ϕ due to the MS effects. Following ref [121] we can estimate the effect of the MS on the size of the cylinder defining the blurring factor $\xi=d\theta$ where d is the distance between cylinder and detector,

$$\theta = 10.5\sqrt{\frac{1}{L_r}}\frac{\sqrt{\rho[g/cc]L[cm]}}{E_p[MeV]}$$

is the Highland formula of the mean angular deflection of a particle with energy E_p traversing a material length L with density ρ , where L_R is the radiation length [122] which depend on the composition of the target. The approximate mono-energetic size of the image at the detector,

$$I_{k,i} = \sqrt{\phi_k^2 + \xi_i^2}$$

would then be convolution of the real size ϕ with the blurring coefficient ξ, and the approximate multi-energetic images would be,

$$I_k = \sum_{i=1}^{N_i} p_i \sqrt{\phi_k^2 + \xi_i^2}$$

Finally knowing the respective blurring coefficient we can deduce the real size of the cylinder for each layer inverting the last equation.

The figure 6.32 shows the synthetic images formed by the multi and mono energies of protons.

Comparison of simulations
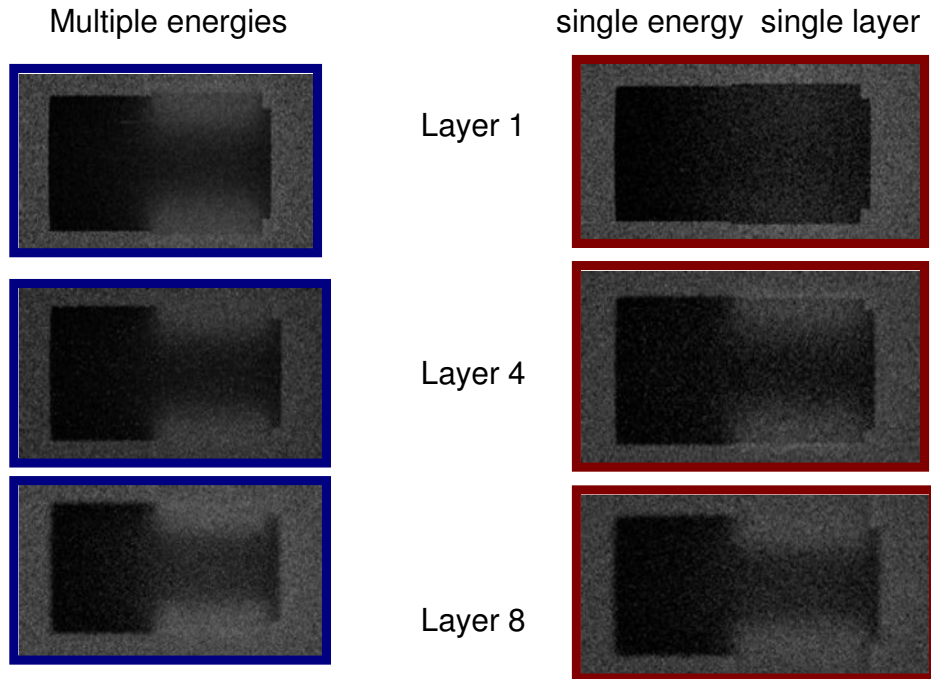
Figure 6.32: it shows comparison between the images formed by the multiple and mono proton energies.

Finally following the experimental analysis we have extracted FWHM by using Gaussian fits and in simulations we have got the similar results as shown in figure 6.33, by taking into account the physical effects which are told above. This shows a very good agreement between experimental and simulated results.

6.11 Conclusions:

My conclusion is that at relative low energy of the probe beam the image on the detectors are mainly formed in negative by protons passing trough the less dense region of the compressed target (plasma corona) and these images are mostly overestimated in the comparison of real images depending on the blurring coefficient due to the MS. Moreover we have shown that the MS is higher in low density plasma than in low density cold matter and how we can take into account this effect in MCNPX simulation.
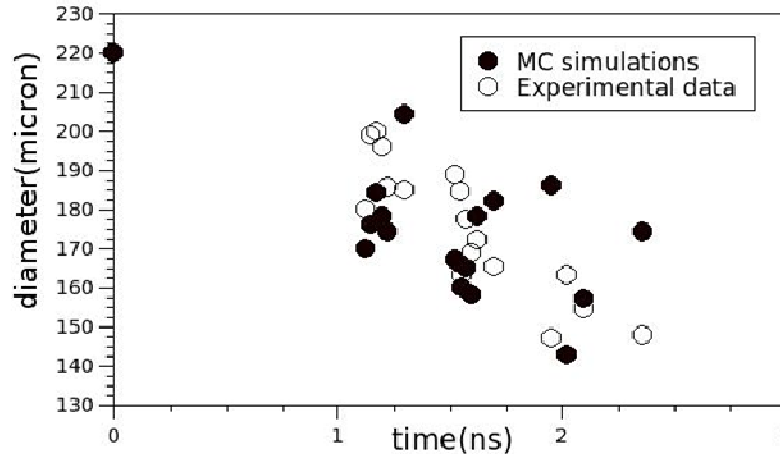
Figure 6.33: Comparison of experimental results with what are obtained in simulations. The black dot at 220µm and 0ns shows the initial diameter of the cylinder whereas all other black dots (Simulated) and circles (experimental) show the compressions at different times. This shows a very good agreement between experimental and simulated results.

Finally we have shown that the simulation can reproduce experimental results exactly if all the above mentioned physical effects are taken into account indeed. Although, at low energy, protons are not able to probe the dense core, the time history and stagnation time are reproduced correctly. The MS is reduced for high proton beam but till now is not clear what is the minimum energy needed to reach a good resolution in ICF experiments, with respect to this we have deduced a simple scaling law for proton energies to overcome certain densities.

General Conclusions and Future Challenges:

Laser-driven proton sources allow the generation of very short pulse (ps) high-charge bunches of protons. This can add new dimensions to present day's application (e.g. the time domain) but above all it can offer the possibility of a cheaper approach to fundamental applications of high-social impact such as proton therapy of cancer. It is shown in this thesis that optimum pre-plasma expansion conditions exist for coupling laser energy to protons, via fast electrons. The measured enhancement in proton beam maximum energy and conversion efficiency are likely due to changes to the propagation of the laser pulse in the low density large scale length pre-plasma. The ultra-low emittance of laser-accelerated protons allowed radiography of dense objects with excellent spatial resolution.

In my opinion, today's challenges in the laser-driven proton sources can be summarized as follows:

1-being able to increase the energy of proton beams up to 300 MeV (for applications in cancer treatment or for radiography of dense / thick samples)

2-being able to achieve such energy by using relatively compact and high-repetition laser systems (therefore system which are characterized by relatively low energy and very short pulses). Indeed such systems are the only ones, which can be really scaled to a real application environment.

3-being able to obtain quasi-monoenergetic spectra (for applications in proton radiography or, again, cancer therapy) or, more in general, to control and shape the proton spectra

4-being able to obtain much larger proton currents and show the focusability of such beams (for applications in fast ignition). Already several approaches have been discussed in the literature concerning focusability: use of bended foils, uses of laser-irradiated cylinders.The focusability of the proton source is related to the very good source emittance (i.e. the fact that the proton flux is laminar, as if it was originated by a virtual *point-like* source). Therefore in a way this work is also connected to the development of new diagnostics: using quadrupoles it will be possible to "image" the proton source (and diagnose it) as it is normally done with optical beams. We will give priority to using magnetic lenses for development of new diagnostics, while in

the proton-driven fast-ignition context we think that passive approaches should be preferred (e.g. bended targets).

Several technical challenges:

1-being able to allow for target replacement and positioning with µm-scale precision at 10 Hz repetition frequency (all this in a high-vacuum "clean" environment as opposed to the present "dirty environment" experiments)

2- being able to diagnose the proton beam in real time with a precise characterization of energy spectrum, emission angle, emitted species (since proton emission ma be accompanied b acceleration of other species of ions). In comparison today we have either large acceptance diagnostics tools which are not "real-time" or do not easily allow for species/energy discrimination (e.g. CR-39 detectors, radiochromic films), or real time diagnostics which have a too-narrow acceptance angle (e.g. Thomson parabolas associated to MCP and CCD detectors)

3- being able to deal with new targets concepts, e.g. structured targets: targets with dots, targets with foam layers on the laser side (to increase laser absorption), modulated targets (again to increase absorption), targets with a well-characterized hydrogenated layer on rear side, etc.

4-being able to master the temporal and spatial shaping of the laser beam (e.g. by improving adaptive optics capability) with the goal of allowing even large laser intensities on target and/or obtaining such intensities with smaller laser systems. Being able to change the wavelength (by frequency conversion) or the polarization of laser light. Higher intensities or, for instance, a clean circularly polarized pulse, could allow to reach and investigate new regimes of laser-induced proton emission (e.g. the so-called radiation pressure acceleration regime).

5-being able to control the laser contrast ratio (intensity ratio between the main short peak and the laser pedestal / prepulse). The laser prepulse on one side controls the extension of the plasma in front of the solid target and therefore laser absorption [A.Flacco, D. Batani, et al. "Characterization of a controlled plasma expansion in

vacuum for laser driven ion acceleration" J. Appl. Phys., 104, 103304 (2008)], on the other side it produce a shock which may break out affecting the target rear, and either reducing acceleration or producing a deformation which may imply the capability for beam steering [F.Lindau, D.Batani, et al. "Laser-Accelerated Protons with Energy Dependent Beam Direction" Phys. Rev. Lett., 95, 175002 (2005)].

REFRENCES:

[1] A. Jullien and al. 10-10 temporal contrast for femtosecond ultraintense lasers by cross-polarized wave generation. Opt. Lett., 30:920, 2004.

[2] Mainfray and al. Multiphoton ionization of atoms. Rep. Prog. Phys., 54:1333, 1991.

[3] S. P. D. Mangles, C. D. Murphy, Z. Najmudin, A. G. R. Thomas, J. L. Collier, A. E. Dangor, E. J. Divall, P. S. Foster, J. G. Gallacher, C. J. Hooker, D. A. Jaroszynski, A. J. Langley, W. B. Mori, P. A. Norreys, F. S. Tsung, R. Viskup, 181

[4] P. Mulser and D. Bauer. High Power Laser Matter Interaction. Springer, 2004.

[5] P. Agostini and al. Multiphoton ionization of hydrogen and rare gases. IEEE J. Quant. Elec., QE-4:667, 1968.

[6] F. Kruer and J. Estabrook. Jxb heating by very intense laser light. Phys. Fluids, 28:430, 1985.

[7] P. Agostini and al. Free transitions following 6-photon ionization of xenon atoms. Phys. Rev. Lett., 42:1127, 1979.

[8] J. Fuchs and al. Comparison of laser ion acceleration from the front and rear surfaces of thin foils. Phys.Rev.Lett, 94:45004, 2005.

[9] A. G. Litvak, \Finite-amplitude wave beams in a magneto-active plasma," Soviet physics JETP, vol. 30, p. 344, 1969.

[10] P. Sprangle et al., \Relativistic self-focusing of short-pulse radiation beams in plasmas," Plasma Science, IEEE Transactions on, vol. 15, p. 145, 1987.

[11] A. B. Borisov et al., \Stabilization of relativistic self-focusing of intense subpicosecond ultraviolet pulses in plasmas," Physical Review Letters, vol. 65, p. 1753, Oct. 1990.

[12] P. Monot et al., \Experimental demonstration of relativistic self-channeling of a multiterawatt laser pulse in an underdense plasma," Physical Review Letters, vol. 74, p. 2953, Apr. 1995.

[13] M. Borghesi et al., \Relativistic channeling of a picosecond laser pulse in a near critical preformed plasma," Physical Review Letters, vol. 78, p. 879, Feb. 1997.

[14] A. Pukhov and J. M. ter Vehn, \Relativistic magnetic self-channeling of light in near-critical plasma: Three-dimensional particle-in-cell simulation," Physical Review Letters, vol. 76, p. 3975, May 1996.

[15] W. Ehler and al. Effect of target purity on laser produced plasma expansion. J. Phys. D, 13:29, 1980.

[16] J. Fuchs and al. Comparison of laser ion acceleration from the front and rear surfaces of thin foils. Phys.Rev.Lett, 94:45004, 2005.

[17] S. J. Gitomer. Fast ions and hot electrons in the laser-plasma interaction. Phys. Fluids, 29:2679, 1986.

[18] D. Gold. Prepulse suppression using a self-induced ultra-shortpulse plasma mirror. SPIE Proc., 1413:41, 1991.

[19] F. Brunel. Not-so-resonant, resonant absorption. Phys. Rev. Lett., 59:52, 1987

[20] P. McKenna and al. Effect of target heating on ion induced reactions in high intensity laser-plasma interactions. Appl.Phys.Lett., 83:2763, 2003.

[21] P. Gibbon. Short Pulse Laser Interactions with Matter. Imperial College Press, 2005.

[22] C. G. R. Geddes, C. Toth, J. van Tilborg, E. Esarey, C. B. Schroeder, D. Bruhwiler, C. Nieter, J. Cary, and W. P. Leemans. High-quality electron beams from a laser wakefield accelerator using plasma-channel guiding. Nature, 431:538–541, sep 2004.

[23] Geant4 collaboration. Geant4 developements and applications. IEEE Trans. on Nucl. Sci., 53:270, 2006.

[24] P. Mulser. Basic laser-plasma interaction and essential relativity, 2006. Lectures

[25] N. Minkovski and al. Polarization rotation induced by cascaded third-order processes. Opt. Lett., 27:2025, 2002

[26] N. Minkovski and al. Nonlinear polarization rotation and orthogonal polarization generation experienced in a single-beam configuration. J. Opt. Soc. Am. B, 21:1659, 2004.

[27] A. Macchi and al. Laser acceleration of ion bunches at the front surface of overdense plasmas. Phys. Rev. Lett., 94:165003, 2005.

[28] F. Lindau and al. Laser-accelerated protons with energy-dependent beam direction. Phys. Rev. Lett., 95:175002, 2005.

[29] R. Cohen, L. Spitzer, and P. M. Routly. The electrical conductivity of a ionized gas. Phys.Rev., 80:230, 1950.

[30] T. V. Liseikina and al. Features of ion acceleration by circularly polarized laser pulses. Appl. Phys. Lett., 91:171502, 2007.

[31] S. Friztler and al. Ion heating and thermonuclear neutron production from high intensity subpicosecond laser pulses interacting withunderdense plasmas. Phys. Rev. Lett., 89:165004, 2002.

[32] P. Mora. Thin-foil expansion into a vacuum. Phys. Rev. E, 72:56401, 2005.

[33] L. Robson et al., \Scaling of proton acceleration driven by petawatt-laserplasma interactions," Nature Physics, vol. 3, p. 58, 2007.

[34] T. E. Cowan et al., \Ultralow emittance, multi-MeV proton beams from a laser virtual-cathode plasma accelerator," Physical Review Letters, vol. 92, p. 204801, May 2004.

[35] M. Borghesi et al., \Multi-MeV proton source investigations in ultraintense laser-foil interactions," Physical Review Letters, vol. 92, p. 055003, Feb. 2004.

[36] P. K. Patel et al., \Isochoric heating of solid-density matter with an ultrafast proton beam," Physical Review Letters, vol. 91, p. 125004, 2003.

[37] S. Kar et al., \Dynamic control of laser-produced proton beams," Physical Review Letters, vol. 100, p. 105004, Mar. 2008.

[38] H. Schwoerer et al., \Laser-plasma acceleration of quasi-monoenergetic protons from microstructured targets," Nature, vol. 439, p. 445, 2006.

[39] B. M. Hegelich et al., \Laser acceleration of quasi-monoenergetic MeV ion beams," Nature, vol. 439, p. 441, 2006.

[40] E. L. Clark et al., \Measurements of energetic proton transport through magnetized plasma from intense laser interactions with solids," Physical Review Letters, vol. 84, p. 670, 2000.

[41] R. A. Snavely et al., \Intense high-energy proton beams from petawatt laser irradiation of solids," Physical Review Letters, vol. 85, p. 2945, Oct. 2000.

[42] A. Maksimchuk et al., \Forward ion acceleration in thin _lms driven by a high-intensity laser," Physical Review Letters, vol. 84, p. 4108, May 2000.

[43] S. P. Hatchett et al., \Electron, photon, and ion beams from the relativistic interaction of petawatt laser pulses with solid targets," in The 41st annual meeting of the division of plasma physics of the american physical society, vol. 7, (Seattle, Washington (USA)), p. 2076, AIP, May 2000.

[44] E. L. Clark et al., \Energetic heavy-ion and proton generation from ultraintense laser-plasma interactions with solids," Physical Review Letters, vol. 85, p. 1654, 2000.

[45] F. N. Beg et al., \A study of picosecond laser{solid interactions up to 10[sup 19] Wcm[sup -2]," Physics of Plasmas, vol. 4, p. 447, Feb. 1997.

[46] J. Badziak et al., \Generation of energetic protons from thin foil targets irradiated by a high-intensity ultrashort laser pulse," Nuclear Instruments and Methods in

Physics Research Section A: Accelerators, Spectrometers, Detectors and Associated Equipment, vol. 498, p. 503, Feb. 2003.

[47] D. Neely et al., \Enhanced proton beams from ultrathin targets driven by high contrast laser pulses," Applied Physics Letters, vol. 89, p. 021502, July 2006.

[48] T. Ceccotti et al., \Proton acceleration with high-intensity ultrahighcontrast laser pulses," Physical Review Letters, vol. 99, p. 185002, Nov. 2007.

[49] A. J. Mackinnon et al., \Enhancement of proton acceleration by hotelectron recirculation in thin foils irradiated by ultraintense laser pulses," Physical Review Letters, vol. 88, p. 215006, May 2002.

[50] M. Hegelich et al., \MeV ion jets from short-pulse-laser interaction with thin foils," Physical Review Letters, vol. 89, p. 085002, 2002.

[51] K. Krushelnick et al., \Energetic proton production from relativistic laser interaction with high density plasmas," in The 41st annual meeting of the division of plasma physics of the american physical society, vol. 7, (Seattle, Washington (USA)), p. 2055, AIP, May 2000.

[52] M. Zepf et al., \Proton acceleration from high-intensity laser interactions with thin foil targets," Physical Review Letters, vol. 90, p. 064801, Feb. 2003.

[53] M. Zepf et al., \Fast particle generation and energy transport in laser-solid interactions," in The 42nd annual meeting of the division of plasma physics of the American Physical Society and the 10th international congress on plasma physics, vol. 8, (Quebec City, Quebec (Canada)), p. 2323, AIP, May 2001.

[54] Y. Murakami et al., \Observation of proton rear emission and possible gigagauss scale magnetic _elds from ultra-intense laser illuminated plastic target," Physics of Plasmas, vol. 8, p. 4138, 2001.

[55] J. Badziak et al., \Fast proton generation from ultrashort laser pulse interaction with double-layer foil targets," Physical Review Letters, vol. 87, p. 215001, Nov. 2001.

[56] M. Roth et al., \Energetic ions generated by laser pulses: A detailed study on target properties," Physical Review Special Topics Accelerators and Beams, vol. 5, p. 061301, June 2002.

[57] F. N. Beg et al., \Target charging e_ects on proton acceleration during high-intensity short-pulse laser-solid interactions," Applied Physics Letters, vol. 84, p. 2766, Apr. 2004.

[58] S. Karsch et al., \High-intensity laser induced ion acceleration from heavy water droplets," Physical Review Letters, vol. 91, p. 015001, July 2003.

[59] M. Schnrer et al., \MeV proton emission from ultrafast laser-driven microparticles," Applied Physics B: Lasers and Optics, vol. 78, p. 895, May 2004.

[60] L. Willingale et al., \Collimated multi-MeV ion beams from high-intensity laser interactions with underdense plasma," Physical Review Letters, vol. 96, p. 245002, June 2006.

[61] M. Kaluza et al., \Inuence of the laser prepulse on proton acceleration in thin-foil experiments," Physical Review Letters, vol. 93, p. 045003, July 2004.

[62] O. Lundh et al., \Inuence of shock waves on laser-driven proton acceleration," Physical Review E (Statistical, Nonlinear, and Soft Matter Physics), vol. 76, p. 026404, 2007.

[63] F. Lindau et al., \Laser-accelerated protons with energy-dependent beam direction," Physical Review Letters, vol. 95, p. 175002, Oct. 2005.

[64] P. McKenna et al., \High-intensity laser-driven proton acceleration: inuence of pulse contrast," Philosophical Transactions of the Royal Society A, vol. 364, p. 711, Mar. 2006.

[65] N. V. Klassen et al., \GafChromic MD-55: Investigated as a precision dosimeter," Medical Physics, vol. 24, p. 1924, Dec. 1997.

[66] W. McLaughlin, \Colour centres in LiF for measurement of absorbed doses up to 100 MGy," Radiation Protection Dosimetry, vol. 66, p. 197, July 996.

[67] M. A. Stoyer et al., \Nuclear diagnostics for petawatt experiments (invited)," in Papers from the thirteenth topical conference on high temperature plasma diagnostics, vol. 72, (Tuscon, Arizona (USA)), p. 767, AIP, 2001.

[68] P. McKenna et al., \Characterization of proton and heavier ion acceleration in ultrahigh-intensity laser interactions with heated target foils," Physical Review E, vol. 70, p. 036405, 2004.

[69] F. H. Seguin et al. Spectrometry of charged particles from inertial confinement-fusion plasmas," Review of Scientific Instruments, vol. 74, p. 975, Feb. 2003.

[70] S. Sakabe et al., \Modi_ed thomson parabola ion spectrometer of wide dynamic range," Review of Scienti_c Instruments, vol. 51, p. 1314, Oct. 1980.

[71] F. Amiranoff, \Fast electron production in ultra-short high-intensity laser plasma interaction and its consequences," Measurement Science and Technology, vol. 12, p. 1795, 2001.

[72] M. Roth et al., \Energetic ions generated by laser pulses: A detailed study on target properties," Physical Review Special Topics Accelerators and Beams, vol. 5, p. 061301, June 2002.

[73] P. E. Young and P. R. Bolton, \Propagation of subpicosecond laser pulses through a fully ionized plasma," Physical Review Letters, vol. 77, p. 4556, Nov. 1996.

REFRENCES

[74] Z. M. Sheng et al., \Anisotropic _lamentation instability of intense laser beams in plasmas near the critical density," Physical Review E, vol. 64, p. 066409, Nov. 2001.

[75] R. Hemker, Particle-in-cell modelling of plasma-based accelerators in two and three dimensions. Phd thesis, University of California, 2000.

[76] S. C. Wilks et al., \Energetic proton generation in ultra-intense laser solid interactions," Physics of Plasmas, vol. 8, p. 542, Feb. 2001.

[77] J. Fuchs et al., \Spatial uniformity of laser-accelerated ultrahigh-current MeV electron propagation in metals and insulators," Physical Review Let- ters, vol. 91, p. 255002, Dec. 2003.

[78] L. Romagnani et al., \Dynamics of electric _elds driving the laser acceleration of multi-MeV protons," Physical Review Letters, vol. 95, p. 195001, Nov. 2005.

[79] T. E. Cowan et al., \Ultralow emittance, multi-MeV proton beams from a laser virtual-cathode plasma accelerator," Physical Review Letters, vol. 92, p. 204801, May 2004.

[80] R. A. Snavely et al., \Intense high-energy proton beams from petawatt laser irradiation of solids," Physical Review Letters, vol. 85, p. 2945, Oct. 2000.

[81] E. Brambrink et al., \Transverse characteristics of short-pulse laser produced ion beams: A study of the acceleration dynamics," Physical Re- view Letters, vol. 96, p. 154801, Apr. 2006.

[82] M. Borghesi et al., \Fast ion generation by high-intensity laser irradiation of solid targets and applications," Fusion Science and Technology, vol. 49, p. 412, Apr. 2006.

[83] L. Romagnani et al., \Dynamics of electric _elds driving the laser acceleration of multi-MeV protons," Physical Review Letters, vol. 95, p. 195001, Nov. 2005.

[84] Y. Sentoku et al., \High energy proton acceleration in interaction of short laser pulse with dense plasma target," Physics of Plasmas, vol. 10, p. 2009, May 2003.

[85] https://www.llnl.gov/str/Hartouni.html

[86] J.D. Lindl, P. Amendt, R.L. Berger, S.G. Glendinning, S.H. Glenzer, S.W. Haan, R.L. Kauffman, O.L. Landen, L.J. Suter, Phys. Plasmas 11 (2004) 339.

[87] D.J. Stevenson, Science 214 (1981) 611.

[88] R. Cauble, T.S. Perry, D.R. Bach, et al., Phys. Rev. Lett. 80 (1998) 1248.

[89] M. Koenig, B. Faral, J.M. Boudenne, D. Batani, A. Benuzzi, S. Bossi, C. Remond, J.P. Perrine, M. Temporal, S. Atzeni, Phys. Rev. Lett. 74 (1995) 2260.

[90] M. Koenig, A. Benuzzi-Mounaix, A. Ravasio, et al., Plasma Phys. Control. Fusion 47 (2005) 441.

[91] S. Atzeni, J. Meyer-ter-Vehn, The Physics of Inertial Fusion, Clarendon Press, Oxford, 2004.

[92] D. Batani, C.J. Joachain, S. Martellucci, A.N. Chester, Atoms, Solids and Plasmas in Super-Intense Laser Fields, Kluwer Academic/Plenum Publishers, New York, 2001.

[93] M. Moran, S. Haan, S. Hatchett, J. Koch, C. Barrera, E. Morse, Rev. Sci. Instrum. 75 (2004) 3592

[94] M.J. Moran, S.W. Haan, S.P. Hatchett, N. Izumi, J.A. Koch, R.A. Lerche, T.W. Phillips, Rev. Sci. Instrum. 74 (2003) 1701.

[95] F.H. Seguin, C.K. Li, J.A. Frenje, et al., Phys. Plasmas 9 (2002) 2725.

[96] A.M. Koheler, Science 160 (1968) 303.

[97] D. West, et al., Nature 239 (1972) 157.

[98] N.S.P. King, E. Ables, K. Adams, et al., Nucl. Instrum. Methods A 424 (1999) 84.

[99] M. Borghesi, J. Fuchs, S.V. Bulanov, A.J. Mackinnon, P.K. Patel, M. Roth, Fusion Sci. Technol. 49 (2006) 412.

[100] R.A. Snavely, M.H. Key, S.P. Hatchett, et al., Phys. Rev. Lett. 85 (2000) 2945.

[101] L. Robson, P.T. Simpson, R.J. Clark, et al., Nature Phys. 3 (2006) 58.

[102] J.A. Cobble, R.P. Johnson, T.E. Cowan, N.R. Galloudec, M. Allen, J. Appl. Phys. 92 (2002) 1775.

[103] M. Borghesi, A.J. Mackinnon, D.H. Campbell, D.G. Hicks, S. Kar, P.K. Patel, D. Price, L. Romagnani, A. Schiavi, O. Willi, Phys. Rev. Lett. 92 (2004) 55003.

[104] T.E. Cowan, J. Fuchs, H. Ruhl, et al., Phys. Rev. Lett. 92 (2004) 204801.

[105] M. Roth, M. Allen, P. Audebert, et al., Plasma Phys. Control. Fusion 44 (2002) B99.

[106] J.F. Ziegler, J.P. Biersack, U. Littmark, The Stopping and Range of Ions in Solids, Pergamon Press, New York, 1985, Available from: http://www.srim.org/

[107] W.T. Scott, Rev. Mod. Phys. 35 (1963) 231.

[108] S. Kar, M. Borghesi, L. Romagnani, S. Takahasi, A. Zayats, S. Fritzler, V. Malka, A. Schiavi, J. Appl. Phys. 101 (2007) 044510.

[109] http://www.ispcorp.com/products/dosimetry/index.html.

REFRENCES

[110] M. Borghesi, A. Schiavi, D.H. Campell, M.G. Haines,

[111] V.L. Highland, Nucl. Instrum. Methods 129 (1975) 497.

[112] T.A. Lasinski, et al., Rev. Mod. Phys. 45 (1973) S1eS176.

[113] "Advanced Diagnostics for Magnetic and inertial fusion" editted by P.E. Stott, Wootton, G. Gorini and D. Batani, Kluwer, Academic/Plenum Publishers, New York ; (2002).

[114] P.-H. Maire and J. Breil, Int. J. *Num. Meth. Fluids* {\bf 56}, 1417 (2008).

[115] C. K. Li at al. *Phy. Rev. Let.* 100, 225001 (2008).

[116] P.-H. Maire, J. Breil, R. Abgral, and J. Ovadia, *SIAM SISC*, 1781 (2007).

[117] https://mcnpx.lanl.gov

[118] A.J.Meckinonn et al. *Phy. Rev. Let.* 97,045001(2006).

[119] M.Borghesi et al. *Plasma physics. Control. Fusion* 43(2001) A267-A276.

[120] http://www.srim.org/

[121] B. Rossi and K. Greisen Rev. Mod. Phys 13 (1941);

[122] http://pdg.lbl.gov/2008/AtomicNuclearProperties